2019-08-01

Pressurized Combustion Product Temperature Measurement Using Integrated Spectral Band Ratios

Scott Cutler Egbert
Brigham Young University

Pressurized Combustion Product Temperature Measurement Using Integrated Spectral Band Ratios

Scott Cutler Egbert

A thesis submitted to the faculty of
Brigham Young University
in partial fulfillment of the requirements for the degree of

Master of Science

Dale Reif Tree, Chair
Brad R. Adams
Brent W. Webb

Department of Mechanical Engineering

Brigham Young University

ABSTRACT

Pressurized Combustion Product Temperature Measurement Using
Integrated Spectral Band Ratios

Scott Cutler Egbert
Department of Mechanical Engineering, BYU
Master of Science

With increasing global power demands, there is a growing need for the clean and efficient use of fossil fuel resources. Gas turbine engines are a commonly used means for generating power; from the propulsion of aircraft to electricity on municipal grids. Measuring the temperature within a turbine combustor or at a turbine inlet could provide numerous advantages related to engine control, durability, efficiency, and emissions and yet this relatively straightforward task has eluded turbine engine manufacturers, primarily because of the high temperatures and pressures, harsh environment, and limited access. Optical emissions measurements are of particular interest for this task as they only require one optical access point and can be accomplished using thin optical fibers that can be fit within existing turbine geometries.

This work extends an optical emission method known as the integrated spectral band ratio (ISBR) method beyond previously obtained temperature measurements on atmospheric combustion products to temperature measurements in a pressurized turbine combustor. The ISBR correlates modeled integrated spectral band ratios of spectral water emission to gas temperature, comparable to two-color pyrometry. When the integrated spectral bands are measured, the temperature can be inferred from this correlation. This technique has previously been successfully applied at atmospheric conditions over pathlengths as short at 25 cm but in this case has been applied at pressures of 0.7 and 1.2 MPa and a pathlength of 15 cm.

Optical measurements were taken in a pressurized combustion test rig at Solar Turbines Inc. in San Diego California. Two temperature sweeps at high load and low load (pressures of 1.2 and 0.7 MPa, respectively) were measured. The average ISBR optical temperature measurements were approximately 200 K higher than the downstream thermocouple measurements. Thermocouple radiative losses were predicted to yield a bias of -175 K. The slope of a change in optical temperature to change in thermocouple temperature was 1.03 over the 87 K variation seen. Repeatability of the optical measurement at a given operating condition was on the order of ± 15 K and the absolute uncertainty of a single measurement was estimated to be ± 70 K over a temperature range of 1350 to 1500 K. The spectra, measured with a Fourier Transform Infrared Spectrometer (FTIR), was in very good agreement with spectral emission models produced using a derivative of the HITEMP database. All of the measured peak locations matched the model, and the measured data matched changes in spectral wings with changing pressure. A linear correlation was also found between raw optical signal and thermocouple measurements.

Keywords: radiation, IR, temperature, H_2O, ISBR, FTIR, optical measurement

ACKNOWLEDGEMENTS

I am grateful for the many individuals, named and unnamed, who have helped me reach this milestone. I continually feel as though I am standing on the shoulders of giants as I try to learn about the world around me and, in some small way, have a positive impact of my own.

I would like to thank Solar Turbines, especially Darrel Zeltner and Mohsen Resoltani, for their assistance with and funding of this work. I also owe an enormous debt of gratitude to Dr. Dale Tree for his mentoring and guidance throughout this project and for the positive impact he has had on my career. I am grateful for my many coworkers and classmates who have helped me throughout my time in school. I would like to thank my family and friends for their support and love, and for listening and nodding appropriately to my frustrations about cold water-vapor absorption and calibration curves. None of the research here would have been possible without a village of support.

And God said, Let there be light: and there was light.

And God saw the light, that it was good

Genesis 1:3-4

TABLE OF CONTENTS

LIST OF TABLES

LIST OF FIGURES

1 INTRODUCTION

Gas turbine engines are used worldwide to meet power generation needs ranging from aircraft propulsion to combined heating and power plants. Efficiency is of high interest due to fuel costs and environmental concerns inherent to fossil fuel combustion. Gas turbines are most efficient when operated at high temperatures, requiring precise controls to avoid overheating and damaging components, especially turbine blades [1]. With advances in gas turbine technology, turbine inlet temperatures can exceed 1500 K [1]. Coupled with the transonic flow speed and tight space constraints, these elevated temperatures make thermocouple temperature measurements at the turbine inlet impractical for most modern gas turbine engines [1, 2]. Standard practice currently involves using a thermocouple to measure turbine exit temperatures from which the turbine inlet temperature can be estimated [2]. Improved understanding of turbine inlet temperature would yield greater insight into thermodynamic conditions, improving modeling, performance, and efficiency.

1.1 Objective

A novel optical gas temperature measurement technique has been developed at Brigham Young University (BYU) in an atmospheric down-fired burner flow reactor (BFR) [3]. This method, known as the Integrated Spectral Band Ratio (ISBR) method, shows promise in gas turbine engines for measuring turbine inlet temperature. Work is being performed such that this

technique can be evaluated in a production grade gas turbine engine in cooperation with Solar Turbines Incorporated (Solar). This text describes a portion of that preparation work.

The objective of this work is to take ISBR measurements in a pressurized gas turbine combustor test rig at Solar and to compare those measurements with concurrently collected thermocouple measurements. Pressure rig testing allows the ISBR method to be evaluated at conditions comparable to those present at the turbine inlet with additional instrumentation and test flexibility than would be available in a production turbine. Optical access to the pressurized combustion gases is also facilitated through existing ports in the pressure rig. These tests represent the first time the ISBR method will be evaluated at pressure. Results will inform decisions related to integration of the technology into a turbine engine. Successful testing will open new pathways into the measuring of turbine inlet gas temperature and represent a step towards continued improvement of gas turbine engine efficiency.

1.2 Scope

As discussed, this work will focus on pressure rig testing of the ISBR method. A sequence of experiments is being performed in four test rigs at Solar Turbines to evaluate the feasibility of using the ISBR method in a gas turbine. The four tests are sequential with a go, no-go decision after each test based on the success of results. The four tests and objectives of each test are outlined in Table 1. The key research questions shown in the rightmost column are summaries of what each test aims to accomplish. These questions will be used to guide each go, no-go decision.

Table 1: Overview of the four tests to be performed at Solar Turbines and the principle objectives of each test. This work will focus on the pressurized rig test.

Test Name	Description	Objective	Key Research Question
Quartz Rig	Pressure: 1 atm Temperature: 1300-1500 K Path length: 210 mm Fiber: Low OH Silica	Demonstrate the integrated H_2O spectral band ratio method at Solar Turbines across a long path length.	Can the ISBR method measure temperature in new environments comparable to BFR performance?
Atmospheric Rig	Pressure: 1 atm Temperature: 1200-1400 K Path length: 25-230 mm Fiber: Low OH Silica	Evaluate the integrated H_2O spectral band method across the thin annular geometry of a turbine. Investigate methods for increasing the optical path length by adjusting the angle at which the probe views the flow annulus.	What are the minimum path length limitations of the ISBR method when a cold cavity is not placed opposite the optical probe? Can the optical path length be extended using fixed turbine geometry?
Pressurized Rig	Pressure: 1-16 atm Temperature: 1300-1500 K Path length: 150 mm maximum Fiber: Sapphire	Evaluate the integrated H_2O spectral band method at pressure across a moderate path length. Investigate integrated spectral CO_2 band methods by broadening the spectrum measured using a sapphire fiber. Design a probe for high pressure testing that can withstand high temperatures without water cooling or purge gas.	Will the ISBR method work at elevated pressures and moderate pathlengths? Can CO_2 emission be used to measure gas temperature? Can the impact pf cold water absorption be mitigated without using purge gas?
Titan 250 Test	Pressure: 21 atm Temperature: 1550 K Path length: 55 mm Fiber: Sapphire	Evaluate integrated H_2O spectral measurement on a commercial gas turbine test engine.	Can the ISBR method be employed in an operational turbine?

Quartz and atmospheric rig testing were performed previously with sufficient success to motivate additional testing in the pressure rig. As such, an optical probe was designed for pressurized measurements. Due to space, temperature, and pressure constraints, this probe must withstand the harsh temperatures without water cooling or purge gas, as has been used for previous ISBR measurements [4]. Correlations between integrated intensity ratios and gas temperature will be generated at pressure for existing spectral bands. Additional bands, available with the use of sapphire optical fibers, were also explored.

In addition to collecting ISBR measurements using a Fourier Transform Infrared (FTIR) spectrometer, an optical setup was designed to collect the integrated band intensities using detectors and optical filters. This system will eliminate the FTIR and integration software from the measurement process, increasing the speed of optical measurements by five orders of magnitude.

2 BACKGROUND

With turbine inlet temperatures in excess of 1500 K, transonic flow speeds, numerous vibrational modes due to blades rotating as fast as 25,000 rpm, and open pathlengths on the order of 4 cm, measuring the temperature just after the combustor of a gas turbine engine presents a unique engineering challenge [1, 2]. Various techniques are currently employed for measuring the temperature of reacting flows, some specific to gas turbine engines with many that have been tested in other settings. In this section, various methods for measuring temperature will be discussed, including in-flow thermocouple measurements, laser-based gas absorption measurements, gas emission measurements, and the ISBR method upon which this work is based.

2.1 In-Flow Thermocouple Temperature Measurements

Thermocouples are a widely used method for measuring the temperature of combustion gases. A thermocouple takes advantage of a phenomenon known as the Seebeck effect, where an electric potential is generated at the junction of two dissimilar metals that have been subjected to a temperature difference [5]. Advantages of thermocouples include their low cost, simplicity, and robustness [6].

Common issues with high temperature thermocouple measurements are caused by radiative losses, low convective heat transfer rates, and material strength concerns at high

temperatures. Thermocouple errors on the order of 200°C are not uncommon without proper mitigation of these errors [5, 6, 7].

Hot thermocouples exchange significant amounts of radiation with the surrounding walls, which are often at a much lower temperature than the gas. This interaction results in a net energy loss and subsequent decrease in thermocouple temperature. A common approach to minimize thermocouple radiative losses is shielding, or surrounding the thermocouple with a thin metal tube to prevent radiative exchange with cold surroundings. Because the radiation shield is also exposed to the hot gas, it will reach a much higher temperature than surrounding walls, allowing the thermocouple to exchange radiation with an object at a comparable temperature, reducing thermocouple radiative losses [5, 7]. The thermocouple probes used in this work consisted of k-type thermocouples ruggedized and shielded from wall radiation inside of stainless-steel tubes.

Similarly, if convective heat transfer rates between the hot gas and the thermocouple are low, radiative losses can dominate convective heating of the thermocouple, or dampen the response rate of the thermocouple to changes in gas properties. Due to the high flow rates and gas densities present in gas turbine environments, rates of convective heat transfer are often very high and do not require additional action, such as drawing air over the thermocouple to increase heat transfer, referred to as aspirating [5, 7].

Recent developments in gas turbine thermocouple measurements focus on new thermocouple materials of very small sizes. Given the high flow rates and temperatures present, large thermocouples or supporting structures could break off, be pulled into the turbine, and cause significant damage to the blades and other components [1]. Thin film thermocouples are being explored that can be deposited directly onto turbine surfaces. Though this limits measurements to boundary layer conditions, good agreement can be obtained between thin film

thermocouples and gas temperature in laboratory settings. Increasing sensor lifetime and decreasing measurement drift are areas of ongoing research [8, 9]. For this reason, thermocouples are typically placed at the end of the expansion stage, where flow conditions are less harsh [2]. While exit temperature measurements can be resolved to within one Kelvin, and are useful in estimating the turbine inlet temperature, this approach limits the spatial resolution of conditions at the inlet due to mixing in the expansion stage [1].

2.2 Laser Absorption Based Optical Temperature Measurements

Optical temperature measurements are a form of non-invasive thermal diagnostics, allowing equipment to be well removed from the flow. Measurements can be performed using both absorption and emission processes. Absorption techniques typically employ a laser with a frequency chosen to interact with a specific absorption line of the gas of interest. Laser-based measurements allow for rapid sampling of temperature and species concentration across a range of path lengths and concentrations.

Two common techniques for measuring gas temperature using lasers are coherent anti-Stokes Raman spectroscopy (CARS) and tunable diode lasers (TDL). CARS measurements employ a pump, a Stokes, and a probe laser that are oriented to intersect at the desired measurement location. The coherent anti-Stokes beam is formed by the gas in this location. Due to the coherence of the beam, signal strength is high, facilitating acquisition. While CARS can provide high signal strength and temporal resolution, requirement for multiple optical access ports at specific orientations, expensive high-powered lasers, and a large knowledge overhead typically prevent CARS from being used outside of laboratory settings [10].

Unlike CARS, TDL measurements probe gas absorption of the laser, as was performed by Zhou [11]. Because TDL systems are line of sight, they typically employ lower power, relatively

inexpensive lasers. These lasers can be tuned or scanned through various wavelengths of interest to probe various absorption features [12]. Frequency comb lasers are being developed that further expand the wavelength range available with laser-based measurements at a cost of system complexity [13].

As mentioned in conjunction with CARS, a major limitation to laser-based methods is the need for at least two optical ports to input and extract the signal, though research is being performed to allow for single point measurements [12]. Additional concerns related to equipment costs and data processing requirements have also made it difficult to apply these techniques outside of the laboratory.

2.3 Emission Based Optical Temperature Measurements

A number of techniques have been explored for measuring the temperature in and near combustors using emitting surfaces or gases. Emissions based techniques can be divided into two groups: methods that measure the emission from solid components, such as blades or walls, from which gas temperature is then inferred, and techniques that measure emission from the gas directly. Both will be discussed.

2.3.1 Solid Emission

General Electric and others have seen success measuring the emission from rotating turbine blades using techniques comparable to two-color pyrometry [14]. Two-color pyrometry is based on the shifting peak of the Planck distribution. For a surface of known emissivity, in its simplest form a gray or constant emissivity, temperature can be calculated by taking the ratio of two distinct wavelengths of emission. An example of such a relationship is shown in Figure 1 for the ratio of emission intensity of a blackbody source at 1.63 μm divided by the emission intensity

at 2.16 μm. Due to the use of ratios, gray, or non-spectral, emissivities have no effect on the resultant relationship.

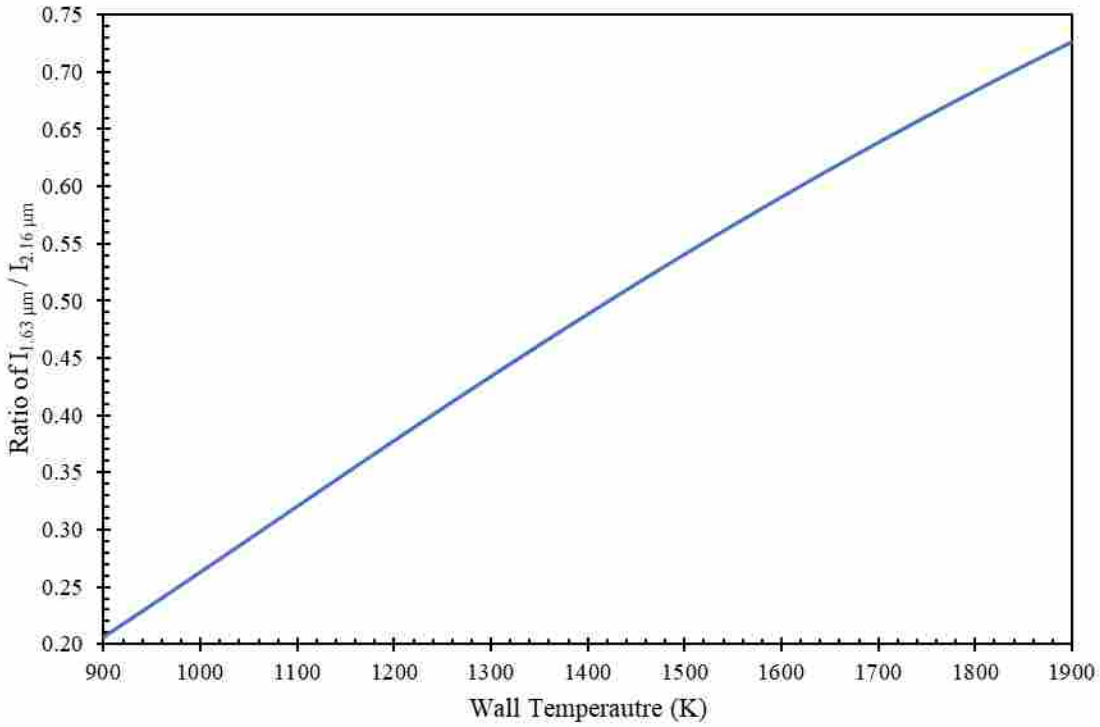

Figure 1: The ratio of emission intensity of a gray surface at 1.63 μm over 2.16 μm as a function of temperature, provided as an example of the foundation of two-color pyrometry.

While not a direct measurement of gas temperature, this technique is useful in identifying overheating turbine blades, a consequence of improper cooling or excessive gas temperatures. The probe is focused such that only one rotating blade occupies the probe view area at a time. Additionally, detectors are available with sufficient temporal resolution so as to distinguish each passing blade. Major setbacks to this technique have included strong combustor radiation reflecting from turbine blades and into the detector and particle deposition, such as soot or sand, on the optical lens [14]. Methods have been found to either compensate for or reduce these measurement errors, greatly improving accuracy and long-term durability [14]. Though

successful at measuring blade temperature, this method does not allow for an understanding of localized or time resolved gas temperature. Furthermore, the temperature measured is dependent on blade cooling properties, in addition to the gas temperature.

2.3.2 Gas Emission

Gas emission techniques typically require longer path lengths or higher concentrations, pressures, and/or temperatures to achieve sufficient signal strength. Evaluating gas emission from a 1.3 MW coal flame, Sonnik Clausen developed a gas temperature measurement method using the strong CO_2 emission band near 4.5 μm [15]. A spectrum comparable to that observed by Clausen is shown in Figure 2 for reference. Because the strength of CO_2 emission near 4.5 μm approaches blackbody emission levels under the conditions shown, a variation of single color pyrometry was used where the emission intensity could be related to the temperature using a calibrated emission measurement and Planck's Law, independent of CO_2 concentration, optical pathlength, or total pressure [15]. Though simple and effective at measuring gas temperature, this method requires a sufficiently long path length, or a high enough pressure or concentration of CO_2, for the emission to approach blackbody levels. Additionally, any lens fouling would bias the measurement, as a decrease in measured signal would be perceived as a decrease in gas temperature.

Comparable techniques have been developed to decrease path length requirements and mitigate the impact of lens fouling. Glasheen et al. used a reference solid body emission wavelength to scale each of three measured gas (H_2O and CO_2) emission wavelengths, thereby correcting for lens fouling [16]. A probe was developed to reduce particle deposition on optical equipment, comparable to that used for measuring turbine blade emission [14].

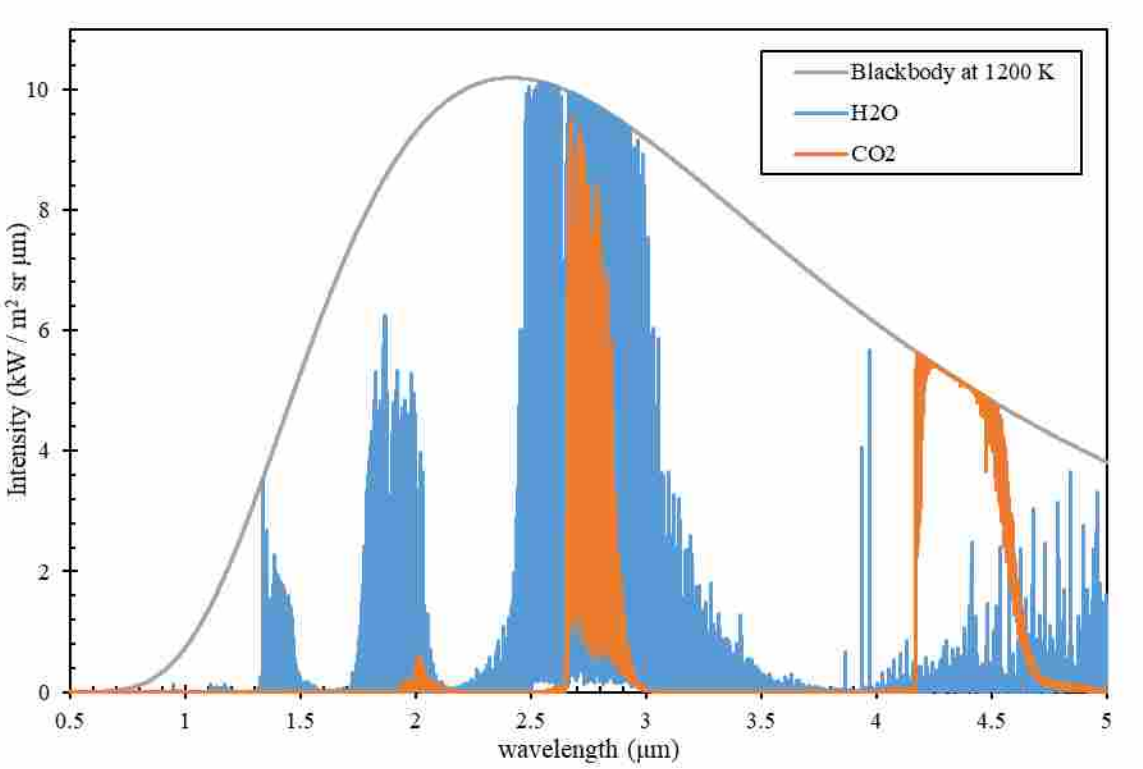

Figure 2: Modeled spectral emission intensity for a gas at 1200 K. 101 kPa, and a 10% concentration of both H_2O and CO_2 along an optical pathlength of 0.5 m.

This technique showed a correlation coefficient of 0.98 with concurrently taken thermocouple measurements. Knowledge of H_2O and CO_2 concentrations is required to convert measured intensity to gas temperature values. The potential for error due to incorrect concentration values is not discussed. Additionally, the wavelengths used or further development of this technique are not readily available in the literature.

Nakaya et al. developed a similar technique, measuring two wavelengths below 1.0 μm [17]. While this spectral range can be measured with inexpensive CMOS detectors, the signal strength in this near visible region is very low, as can be seen in Figure 2. Fluctuations of nearly 200 K in measured temperature were observed, even at the over 1700 K gas temperatures measured [17].

2.3.3 Integrated Spectral Band Ratios

A novel method for measuring the temperature of combustion gases was recently developed at BYU in a 150 kW_{th} atmospheric, down-fired reactor and is known as the Integrated Spectral Band Ratio (ISBR) method [3]. The ISBR technique utilizes the emission of water vapor between 1.54 and 2.22 μm, chosen due to the presence of significant H_2O emission with minimal CO_2 interference (see Figure 2 for reference). A more detailed plot of this region, as measured by Tobiasson using a low-OH silica optical fiber to transmit light from the post-flame region of natural gas combustion products to an FTIR Spectrometer, is given in Figure 3 [4].

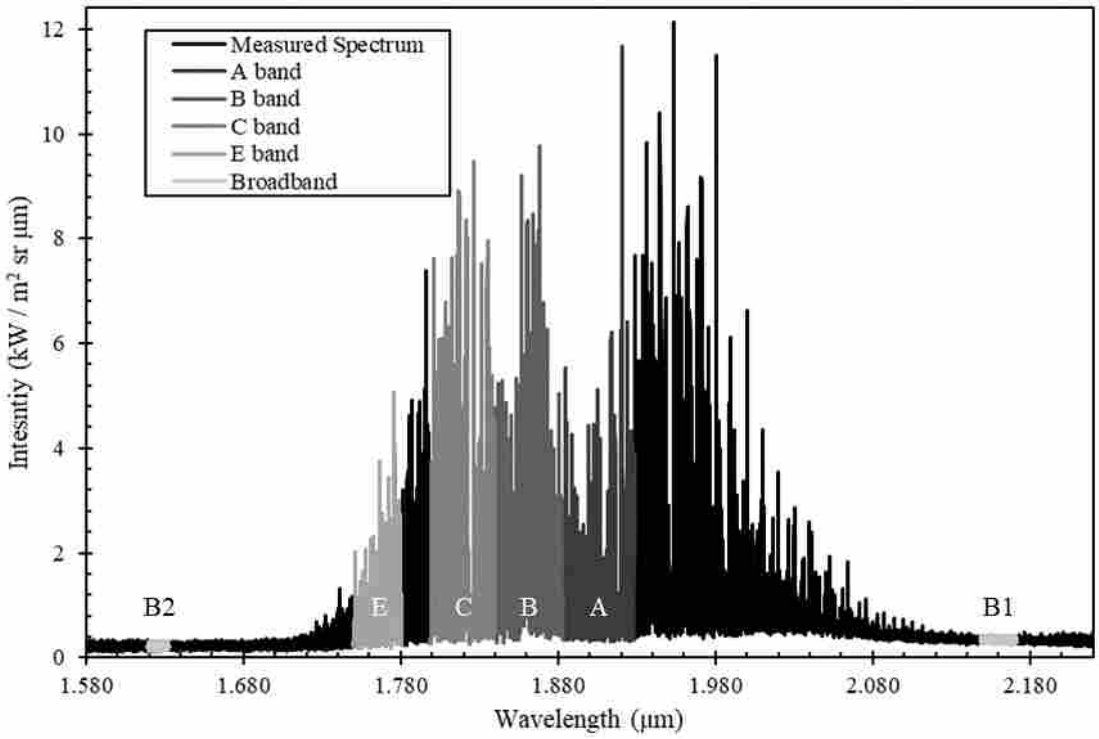

Figure 3: Measured spectral emission intensity in the BYU BFR along an optical pathlength of 0.58 m when viewing natural gas−air products. IR spectral bands used in determining broadband (B1 and B2) and gas (A, B, C, and E) temperatures are highlighted [4].

Similar to the method developed by Clausen, the gas was assumed to be of uniform composition and temperature along the optical path. Gas emission was isolated from other

sources, such as wall or particle emission, depending on the fuel type, through the use of a cold target and numeric analysis, as will be discussed in the following section [4]. Ratios of integrated intensities from two spectral bands, for example E and C in Figure 3, were identified that resulted in a monotonic, near-linear function of temperature [3, 18]. It was found that these ratios are largely independent of changes in water concentration, pressure, or pathlength, as shown in Figure 4 for the ratio E/C, easing the requirement that the gas be at known and uniform conditions. Variations in pressure by a factor of six, water concentration by a factor of three, or pathlength by a factor of three all result in a change in ratio value equivalent to a temperature change of approximately 22 K at 1400 K for the base conditions of 101 kPa, 6% H_2O, and a 15 cm pathlength, a change of 1.5% in gas temperature for 300 to 600% changes in gas properties.

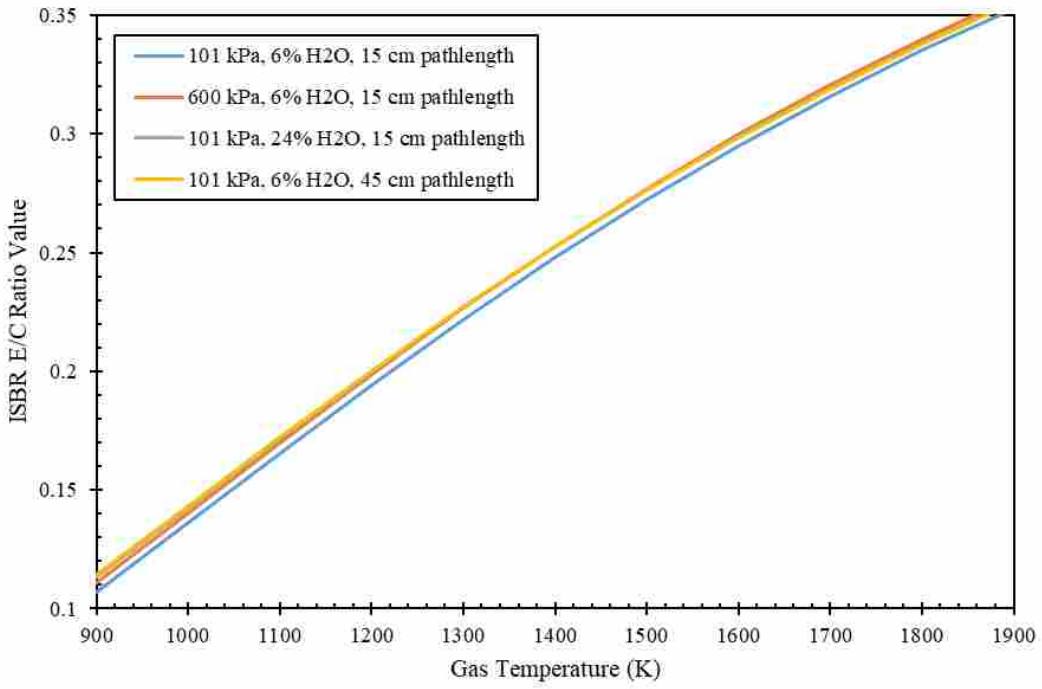

Figure 4: ISBR correlation used for calculating gas temperatures between 900 - 1900 K based on the ratio of integrated spectral intensity in bands E and C. Note that significant changes in pressure, pathlength, and gas concentration have minimal effect on the value of E/C.

It has been found that ISBR temperature measurements agree well with the mean gas temperature when the gas temperature varies along the measurement pathlength, as was the case in the down-fired reactor due to the interaction of the gas and the cooled reactor walls [18]. Cold water vapor along the optical path, either in the measurement volume or between the optical fiber exit and the optical detector, did have a significant and detrimental effect on the ability to optically measure temperature due to partial absorption of the hot gas radiation. This cooled gas, believed to result from partially cooled combustion products near the reactor walls, was removed by purging the optical probe with non-participating nitrogen gas [4]. At atmospheric conditions, signal strength limited the ISBR technique to pathlengths above 0.25 meters [4]. Due to optical fiber restrictions, emission regions outside of 1.54 - 2.22 μm have not been explored using ISBR.

The objective of this work is to explore using the ISBR technique in a pressurized environment at comparable conditions to the combustor exit of a turbine engine. This will involve evaluating ISBR ratios at elevated pressures of approximately 1.2 MPa and pathlengths of 15 cm. It is anticipated that the increase in gas emission due to the increased pressure will allow for measurements of shorter pathlengths than at atmospheric conditions. Additional deviations from previous measurements include the design and use of an uncooled, unpurged optical probe, the use of sapphire optical fibers with a wider transmission range, and lower water concentrations than have previously been measured.

3 THEORETICAL APPROACH

The methods used to measure gas temperature of the combustion products of a high-pressure gas turbine injector rig are explained in this chapter by first reviewing aspects of radiation heat transfer and applying them to a one-dimensional (1D) radiation model, then explaining how the integrated spectral band ratio process was applied to the specific probe and geometry for this experiment.

3.1 Radiative Heat Transfer

Foundational to understanding the ISBR method are definitions for radiative heat transfer properties such as intensity, heat rate, and solid angles.

Spectral intensity I_λ, is defined as a unit emitted radiative power dq, per unit projected area (area normal to the rays) $dA_1 \cos\theta$, per unit solid angle $d\omega$, per wavelength $d\lambda$, as shown in Equation (3-1) [19, 20].

$$I_\lambda \equiv \frac{dq}{dA_1 \cos\theta \, d\omega \, d\lambda} \tag{3-1}$$

Total intensity I, is defined as the integral of spectral intensity over all wavelengths, as shown in Equation (3-2).

As can be seen from Equation (3-1), intensity is defined per unit solid angle. Solid angles are the three-dimensional analog of the commonly used two-dimensional plane angles, as defined in Equation (3-3), where r is the distance between surface 1 and 2, and dA_p is the projected area of surface 1 normal to r, which is equal to $\cos\theta_1\, dA_1$.

$$I = \int_0^\infty I_\lambda \, d\lambda \tag{3-2}$$

$$d\omega \equiv \frac{dA_p}{r^2} = \frac{\cos\theta_1 \, dA_1}{r^2} \tag{3-3}$$

Figure 5 gives a visual representation of a generic form of Equations (3-1 and (3-3. Because intensity is defined as the radiative energy per unit solid angle, for a given $d\omega$ the value of intensity does not change with r in a non-participating medium [19, 20].

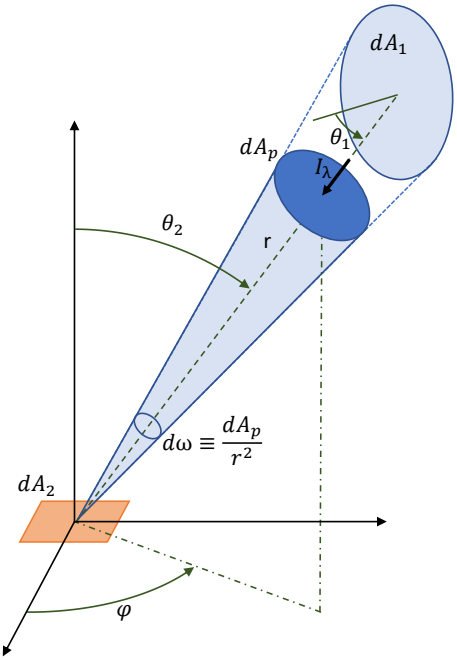

Figure 5: Definition of intensity highlighting the use of solid angles, dω.

An optical detector collects incident irradiation to an active surface area. As such, a detector will, in reality, measure a radiative power incident on the detective area, also known as a radiative heat rate Q. In the case of an FTIR, a spectral radiative heat rate Q_λ, is measured. This spectral heat rate is defined as shown in Equation (3-4), where $G_{\lambda,1\to2}$ is the spectral irradiative flux incident on surface 2, traveling from some emitting surface or participating media with projected area A_p. For ISBR measurements, the receiving surface A_2 is the area of an optical lens or the area of an optical fiber, either of which is small compared to the blackbody or gaseous source from which the radiation originates. This radiative heat rate is transferred to the detector as collimated radiation. As such, $G_{\lambda,1\to2}$ can be approximated as a constant across A_2.

$$Q_\lambda = \int_{A_2} G_{\lambda,1\to2} dA_2 \cong G_{\lambda,1\to2} A_2 \tag{3-4}$$

Spectral irradiative flux is defined in Equation (3-5) using intensity and geometric relationships. $G_{\lambda,1\to2}$ is seen to be the integrated incident intensity over the solid angle weighted by the incident angle. In the case of the measurements to be presented, the lens is oriented normal to the irradiation such that $\cos\theta_2 = 1$. The irradiation can also be approximated as constant over the solid angle view area $\Delta\omega_{1\to2}$ over which the lens collects light. As such, the incident irradiation reduces to the incident intensity multiplied by the solid angle of incident light directed into the end of the optical fiber by the lens, as shown in Equation (3-6. Substituting Equation (3-6 back into Equation (3-4) yields Equation (3-7).

$$G_{\lambda,1\to2} = \int_{2\pi} I_{\lambda,1\to2} \cos\theta_2 \, d\omega \tag{3-5}$$

$$G_{\lambda,1\to2} = I_{\lambda,1\to2}\Delta\omega_{1\to2} \tag{3-6}$$

$$Q_{\lambda} = I_{\lambda,1\to2}\Delta\omega_{1\to2}A_2 \tag{3-7}$$

When any measurement is obtained, the heat rate is converted to a voltage by the detector and associated electronics. The measured voltage is therefore the incident intensity multiplied by a spectral sensitivity factor accounting for the response of the detector C_{λ}, converting incident heat rate to a voltage, and a geometry factor $\Delta\omega_{1\to2}A_2$, representing the combination of collection optics geometry shown in Equation (3-8).

$$V_{\lambda} = C_{\lambda}I_{\lambda,1\to2}\Delta\omega_{1\to2}A_2 \tag{3-8}$$

Calibration for the combination of $C_{\lambda}\Delta\omega_{1\to2}A_2$ is done by facing the collection probe at a blackbody cavity at a known temperature such that the intensity can be calculated from Planck's equation, as shown numerically in Equation (3-9). So long as the detector and the geometry of the measurement optics remain unchanged, this calibration can be used to infer the intensity of the measured irradiation in the pressure rig.

$$C_{\lambda}\Delta\omega_{1\to2}A_2 = \frac{V_{\lambda}}{I_{\lambda}} \tag{3-9}$$

For the high-pressure rig, optical access was through a narrow port that did not allow probe cooling or a large optical lens. As a result, a design for the probe was selected using a spherical sapphire lens that produced a very short focal length. This was desirable to reduce the amount

cold H_2O gas absorption in the probe and to enable the probe to withstand high temperatures. The use of a spherical lens was problematic in that the acceptance angle of light able to enter the optical fiber was no longer limited to a small cone angle as was used previously by Ellis [3]. A depiction of the optical geometry is shown in Figure 6. When testing with a plano-convex lens, it was found that the view angle deviated 0.61° from cylindrical [4]. This value was obtained by moving the optical probe towards the blackbody until the signal stopped increasing, occurring at approximately 0.8 meters of separation, signifying that the view area was completely occupied by the blackbody cavity for all calibration measurements within 0.8 meters. Similar tests using the spherical lens did not result in a maximum value until the probe was partially inside of the blackbody cavity, indicative of a significantly larger view angle.

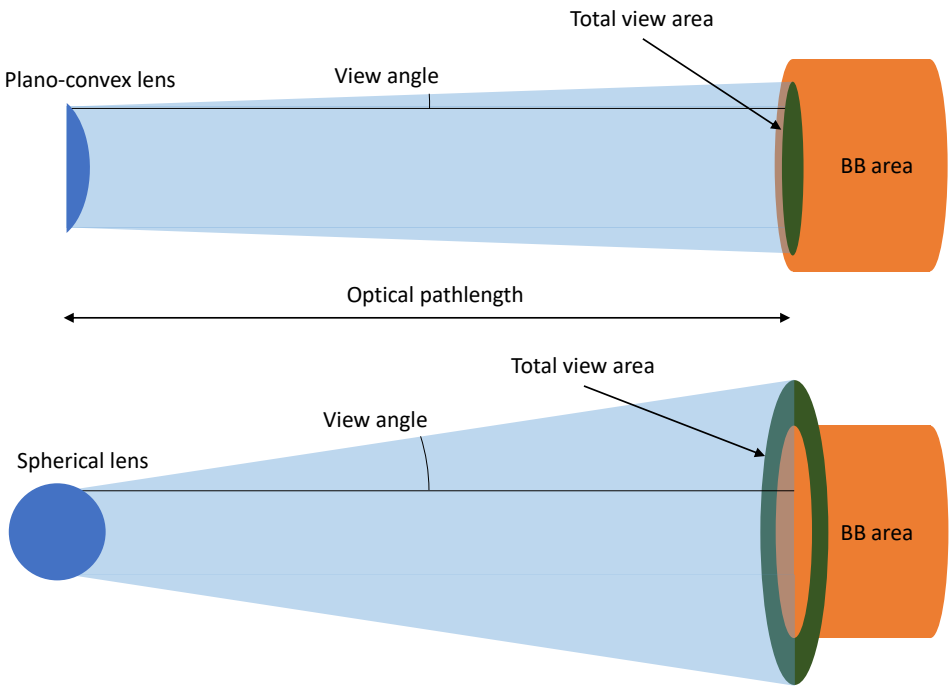

Figure 6: Schematic highlighting the impact of poorly collimated light on the calibration view area. The view angle for an optical probe utilizing a plano-convex lens, as was used for previous ISBR measurements [4], and that of a spherical lens, as used in this work, are shown.

During testing, the measured magnitude of the pressurized measurements was found to be significantly higher than that of blackbody calibration measurements, even though the former had an emissivity lower than unity and the latter were at higher temperatures. This was interpreted as further evidence that the blackbody cavity was not able to fill the total solid angle view area of the probe. As such, calibration measurements did not have equivalent solid angles of incident intensity as the pressure rig measurement, where the combustion gases were able to fill the total view area. This meant that the geometric sensitivity constant, $\Delta\omega_{1\to2}A_2$ in Equation (3-7, that was found during calibration could not be directly used to obtain a measured intensity for data collected in the pressure rig. As a result, a new calibration procedure was required for implementing the ISBR method.

3.2 ISBR for Non-Collimated Measurements

The measured radiation field is governed by the 1D form of the radiation transfer equation (RTE). Light traveling along a given path is collected by a lens, focused onto a fiber optic cable, and transmitted to a detector.

The complete form of the 1D RTE is shown in Equation (3-10) where $\frac{dI_\lambda}{ds}$ is the change in intensity, I_λ, along a differential pathlength, s. On the right side of the equation, the terms represent the emission, absorption, out scattering, and in scattering of the participating medium, respectively [19]. These terms could be due to gas or particulate matter.

$$\frac{dI_\lambda}{ds} = \kappa_\lambda I_{\lambda,bb}(T) - \kappa_\lambda I_\lambda - \sigma_\lambda I_\lambda + \frac{\sigma_\lambda}{4\pi}\int_{4\pi} I_\lambda(\hat{s_i})\,\Phi(\hat{s}_i,\hat{s})d\Omega_i \tag{3-10}$$

As this work involves measuring and modeling natural gas combustion products well after the reaction zone, the participating medium will be solely composed of radiating gas molecules with negligible particulate or soot. As such, scattering is negligible, yielding Equation (3-11) [19].

$$\frac{dI_\lambda}{ds} = \kappa_{\lambda,g} I_{\lambda,bb}(T_g) - \kappa_{\lambda,g} I_\lambda \tag{3-11}$$

Here $\kappa_{\lambda,g}$ is the spectral absorption coefficient of the gas, $I_{\lambda,bb}(T_g)$ the spectral blackbody emission at the gas temperature T_g, and I_λ the spectral irradiation entering the differential length ds.

Integrating Equation (3-11) along a discrete pathlength, Δs, of constant radiative properties yields Equation (3-12).

$$I_{\lambda,s+\Delta s} = I_{\lambda,s} \exp(-\kappa_{\lambda,g}\Delta s) + I_{\lambda,bb}(T_g)[1 - \exp(-\kappa_{\lambda,g}\Delta s)] \tag{3-12}$$

$I_{\lambda,s+\Delta s}$ represents the intensity leaving the system in the direction of interest, $I_{\lambda,s}$ the intensity entering and being attenuated by a factor of $\exp(-\kappa_{\lambda,g}\Delta s)$ as it passes through the medium, and $I_{\lambda,bb}(T_g)$ the spectral blackbody gas emission multiplied by the effective emissivity, as defined in Equation (3-13).

$$\varepsilon_{\lambda,g} = 1 - exp(-\kappa_{\lambda,g}\Delta s) \tag{3-13}$$

For this work, gas emission values were taken from the work of Pearson et al., a derivative of the HITEMP 2010 database [21]. Accordingly, $\kappa_{\lambda,g}$ is generated as shown in Equation (3-14, where P_{tot} is the total pressure, y_{H2O} the gas concentration, R_u the ideal gas constant, T_g the gas temperature, and N_A Avogadro's number. $C_{abs,\lambda,g}$ are gas specific coefficients derived from the HITEMP 2010 database by Pearson et al. [21].

$$\kappa_{\lambda,g} = C_{abs,\lambda,g} \frac{y_{H2O} P_{tot}}{R_u T_g} N_A \tag{3-14}$$

In the case of multiple participating gas species, values of $\kappa_{\lambda,i}$ for each species were summed to generate a $\kappa_{\lambda,total}$. In this work only H_2O and CO_2 were evaluated due to their relatively high concentrations in lean natural gas combustion and their emission in the wavelength range of interest.

Incorporating Equation (3-13) into Equation (3-12) yields Equation (3-15), shown below.

$$I_{\lambda,s+\Delta s} = I_{\lambda,s}(1 - \varepsilon_{\lambda,g}) + I_{\lambda,bb}(T_g)\varepsilon_{\lambda,g} \tag{3-15}$$

Using Equation (3-15), the incident intensity on a surface can be calculated by defining a boundary intensity at the opposite surface and integrating along a pathlength, *L*, to the incident surface. While various temperature and gas concentration profiles could be defined as a function of pathlength, the concentration and temperature profiles for measurement calculations were assumed uniform, based on the limited impact that variations in gas properties have on ISBR measurements (Figure 4). The impact of this assumption of optical temperatures will be further

explored in Sections 5.5.5 and 5.5.6. Numerical experiments were then performed to determine the errors associated with non-uniform profiles.

The far wall was assigned a non-spectral emissivity of ε_{wall}, based on measurements of similar refractory liners in the 1 to 2 μm range [22]. Any spectral transmittance of the optical lens is included in the $C_\lambda \Delta\omega_{1\to2} A_2$ data measurement term obtained during calibration (Equation (3-16). Both the wall and lens boundary conditions were assumed to be non-reflective, with numerical experiments being used to confirm the negligible impact of reflectivity on calculated optical temperatures. The resulting simplified form of the integrated radiative equation used to infer temperature is shown in Equation (3-16). The first term on the right-hand side is the intensity contributed by the surface opposite the measurement $I_{\lambda,bb}(T_{wall})\varepsilon_{\lambda,wall}$ and the second term the intensity contributed from the gas volume along the line of sight $I_{\lambda,bb}(T_g)\varepsilon_{\lambda,g}$. The results for one such model were shown in Figure 2.

$$I_{\lambda,meas} = I_{\lambda,bb}(T_{wall})\varepsilon_{wall}(1-\varepsilon_{\lambda,g}) + I_{\lambda,bb}(T_g)\varepsilon_{\lambda,g} \tag{3-16}$$

3.2.1 Calculation of Gas Temperature

From the discussion in Section 3.1, intensity is collected from a solid angle $\Delta\omega$ to a surface of area A where it is converted to a voltage using a transfer function C_λ. Thus, the measured voltage for a wavelength is represented by Equation (**3-17**.

$$V_{\lambda,meas} = \left[I_{\lambda,bb}(T_{wall})\varepsilon_{wall}(1-\varepsilon_{\lambda,g}) + I_{\lambda,bb}(T_g)\varepsilon_{\lambda,g}\right] C_\lambda A \Delta\omega_{meas} \tag{3-17}$$

The optical probe was placed in front of a portable blackbody calibration source of known temperature. Comparable devices have been shown to possess effective emissitivies on the order of 0.998 [15]. In this configuration, the gas emissivity was assumed to be zero and the wall emissivity was approximated as 1.0, resulting in values for $C_\lambda A \Delta\omega_{cal}$ as derived from Equation **(3-18)**. This combination of variables is a transfer function that allows a conversion of measured voltage to intensity so long as C_λ, A, and $\Delta\omega$ remain constant. Since C_λ is dependent on the detector and A is the area of the sapphire lens, both were unchanged between calibration and measurement. As discussed, $\Delta\omega$ was found to change between the calibration and the measurement. By defining a constant b as the solid angle ratio (SAR), or the ratio of the measured solid angle $\Delta\omega_{meas}$ to the calibration solid angle $\Delta\omega_{cal}$ ($b = SAR \equiv \frac{\Delta\omega_{cal}}{\Delta\omega_{meas}}$), the previously obtained calibration transfer function can still be used to convert $V_{\lambda,meas}$ to an intensity, as shown in Equation (**3-18**, so long as b can be obtained.

$$I_{\lambda,meas} = (C_\lambda A \Delta\omega_{cal}) b V_{\lambda,meas} \tag{3-18}$$

During data collection, the measured voltage can be decomposed and written as shown in Equation (**3-19**. Initially, none of the individual terms on the right-hand side are known.

$$V_{\lambda,meas} = \left[I_{\lambda,bb}(T_{wall})\varepsilon_{wall}\left(1-\varepsilon_{\lambda,g}\right) + I_{\lambda,bb}\left(T_g\right)\varepsilon_{\lambda,g}\right] C_\lambda A \Delta\omega_{cal} b \tag{3-19}$$

Wall emission can be isolated using two-color pyrometry in regions with minimal gas emission, $\varepsilon_{\lambda,g} \cong 0$, such as the regions marked as B1 and B2 in Figure 3. In these spectral regions, Equation (**3-19** reduces to Equation (**3-20**.

$$V_{\lambda,meas} = \left[I_{\lambda,bb}(T_{wall})\varepsilon_{wall}\right] C_\lambda A \Delta\omega_{cal} b \tag{3-20}$$

Because b is non-spectral, it will divide out of the ratio of intensities, as shown in (**3-21**, where $C_1 A\Delta\omega_{cal}$ and $C_2 A\Delta\omega_{cal}$ represent the calibrated detector response sensitivity factors at each wavelength evaluated. Wall temperature can then be calculated using classical two-color pyrometry, independent of variations in solid angle between calibration and the measurement, using a correlation like that shown in Figure 1.

$$\frac{I_{2,bb}(T_{wall})}{I_{1,bb}(T_{wall})} = \frac{V_{2,bb,meas}}{V_{1,bb,meas}} \frac{C_1 A\Delta\omega_{cal}}{C_2 A\Delta\omega_{cal}} \tag{3-21}$$

Returning to Equation (**3-17**, only four unknowns remain: T_g, $\varepsilon_{\lambda,g}$, ε_{wall}, and b. These variables can be found by iterating the following algorithm. Optical gas temperature and measured pressure, pathlength, and species concentrations are used in calculating $\varepsilon_{\lambda,g}$. Due to the interdependence of calculated properties, inputs of a guessed temperature, for example $T_g = 1400K$, and a SAR value, $b = 1.0$, were needed in calculating other properties. Convergence was not affected by the initial guess.

1. Use the known $C_\lambda A\Delta\omega_{cal}$ to convert each measured voltage to $I_{\lambda,meas}/b$ per Equation (**3-18**. After the first iteration, $I_{\lambda,meas}$ can be updated using the current value of b.
2. Calculate gas emissivity $\varepsilon_{\lambda,g}$ from Equations (3-14 and (**3-13** using the current gas temperature and the measured pressure and water concentration from the Solar test cell data. The water concentration was determined to be twice the measured CO_2 concentration, as 94% of the natural gas fuel was methane.

3. Calculate wall conditions T_{wall} and ε_{wall} using Equation (**3-21** for T_{wall} and by rearranging Equation (**3-20** to solve for ε_{wall} once T_{wall} is known. Because the wall is assumed gray, ε_{wall} can be calculated in either wavelength region that does not contain gas emission. Note that T_{wall} will not change with each iteration, but ε_{wall}, which is not based on a ratio, is a function of b. Values for ε_{wall} will converge in parallel with values for b.
4. Calculate gas temperature T_g by solving Equation (**3-19** for the gas emission term $I_{\lambda,bb}(T_g)\varepsilon_{\lambda,g}$ at each measured band, integrating the intensity of that band and taking the ratio of two bands to produce the ISBR, which was then correlated to a gas temperature. Note that b will be factored out of the resulting equation, comparable to Equation (**3-21**.
5. With all other variables known, use Equation (**3-19** to solve for b, the SAR.
6. Iterate on steps 2 through 5 using the updated values of T_g and b, updating $I_{\lambda,meas}$ with each iteration.

The SAR algorithm flowed comparably to the previous ISBR algorithm [3, 4]. The algorithm was iterated until values of T_g and b did not change by more than 0.1% between iterations. A visual depiction of the data processing method is given in Figure 7 for reference, with a complete version of the MATLAB algorithm used given in Appendix A.

3.2.2 Spectral Band Selection

Spectral measurement bands were selected by Ellis by identifying regions with a single participating molecule, in this case water, and testing combinations of ratios through a process of trial and error [3]. These bands were identified as regions where the modeled ratio of integrated intensities from two spectral bands varied almost linearly with changing gas temperature. In

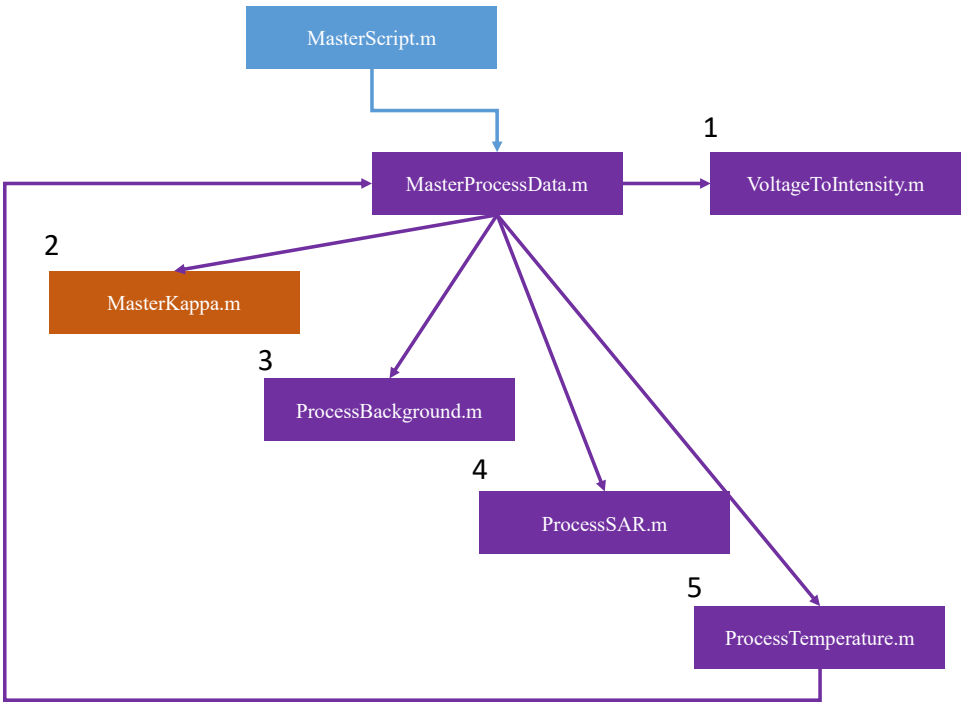

Figure 7: Flow chart for the ISBR algorithm with the SAR extension. Step 1 was performed once, with steps 2-5 iterated until convergence was achieved. See Appendix A for a complete version of the MATLAB algorithm used.

addition to a linear relationship with temperature, the use of ratios gave the added benefit of a nearly concentration, pressure, and pathlength independent method for evaluating gas temperature, as was shown in Figure 4. The ranges of the spectral bands used by Ellis are given below as bands A-E in Table 2. Each spectral band is nominally 100 cm^{-1} in width, possessing at least 35 individual gas emission peaks [3]. The bands for calculating broadband conditions, B1 and B2, are also included in Table 2. As can be seen in Figure 2, gas emission is negligibly small in these two regions of the spectrum, allowing for the calculation of broadband, non-vapor phase emission, originating from the wall or particles in the flow. These bands were modified slightly from those used by Ellis and Tobiasson to better avoid any water emission [3, 4].

Previous ISBR temperature measurements were taken using a Thorlabs low OH silica multimode fiber [3, 4]. This fiber was limited to a spectral range below approximately 2.3 μm, as

Table 2: Bands used for ISBR measurements. Ratios evaluated for gas temperature were E/A, E/B, E/C, with B2/B1 used for wall temperature.

Band	Wavenumber (cm^{-1})	Wavelength (μm)
A	5185-5310	1.883-1.929
B	5310-5435	1.840-1.883
C	5435-5560	1.799-1.840
E	5615-5715	1.750-1.781
B1	4605-4655	2.148-2.172
B2	6125-6175	1.619-1.633

was shown in Figure 3. Unique to this work is the use of sapphire optical fibers for their ability to withstand high temperature conditions in an uncooled, pressurized optical probe. An added benefit in using a sapphire optical fiber is the ability to transmit further into the infrared, with strong transmission out to approximately 3.0 μm. Figure 8 depicts a 1D spectral model for a gas at 1400 K, 1200 kPa, consisting of 6% H_2O and 3% CO_2 (methane products) along an optical pathlength of 0.15 m with an opposite wall at 800 K and an emissivity of 0.4. Blackbody emission at 1400 K (equivalent to the gas temperature) is also shown for reference. The pressurized spectra look similar to the atmospheric pressure spectra shown in Figure 2.

With the additional spectral range afforded by sapphire optical fibers, new spectral bands were explored for calculating ISBR temperatures through a similar process to that employed by Ellis in the transmission range of silica fibers [3]. Emission between 2.40-2.65 μm contains strong water emission with minimal CO_2 emission, a promising region for calculating gas temperature. Additionally, a large portion of the previous silica bands (A-E) was combined to produce a new larger band with a higher integrated intensity (J). These additional bands, referred to collectively as sapphire bands, are given in Table 3.

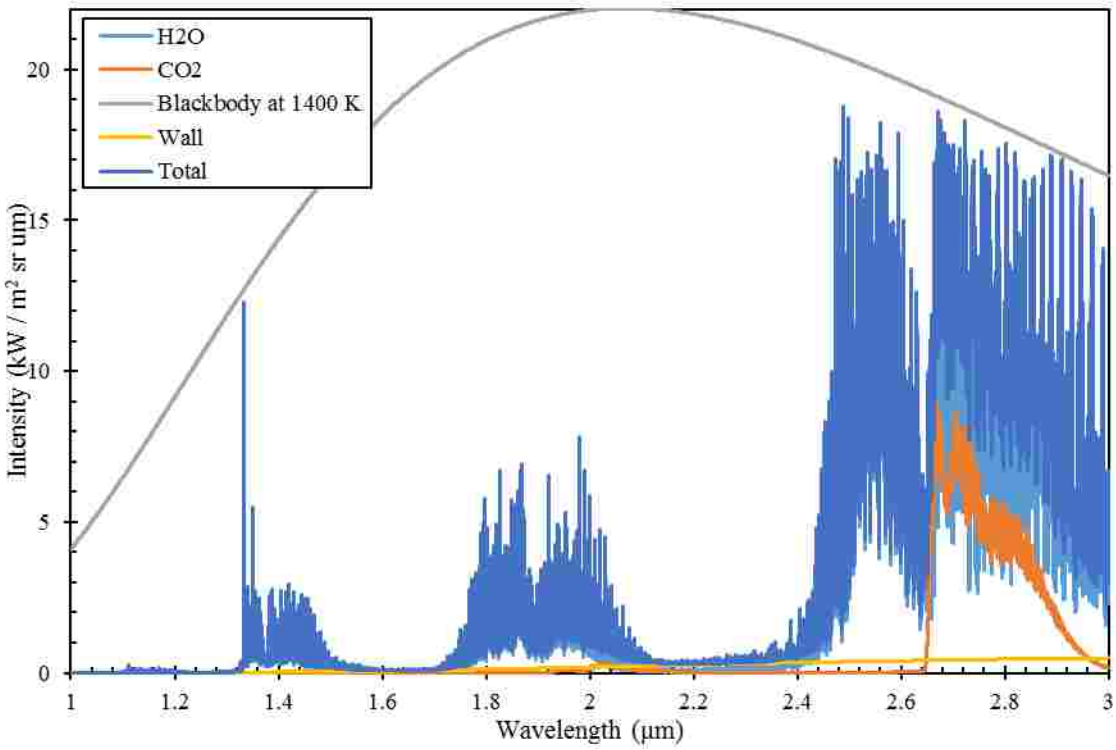

Figure 8: Modeled spectral emission intensity for a gas at 1400 K, 1200 kPa, 6% H2O and 3% CO_2 (methane products) along an optical pathlength of 0.15 m with a wall at 800 K and an emissivity of 0.4 at the far side of the optical path.

Table 3: Sapphire range ISBR bands

Band	Wavenumber (cm^{-1})	Wavelength (µm)
F	3800-3900	2.564-2.632
G	3900-4000	2.500-2.564
H	4000-4100	2.439-2.500
J	5200-5800	1.724-1.923

All promising correlations from ISBR combinations are shown in Figure 9, and include the silica bands of E/A, E/B, and E/C and the newly identified sapphire bands of H/F, G/F, J/F, J/G, and J/H. The correlations shown are for a 1D model at 1200 kPa, 6% water concentration, and pathlength of 15 cm. Elevated pressure does not appear to significantly affect the shape of

ISBR lines, as can be seen by comparing E/C shown in Figure 9 to Figure 4, or to correlations given by Ellis or Tobiasson [3, 4].

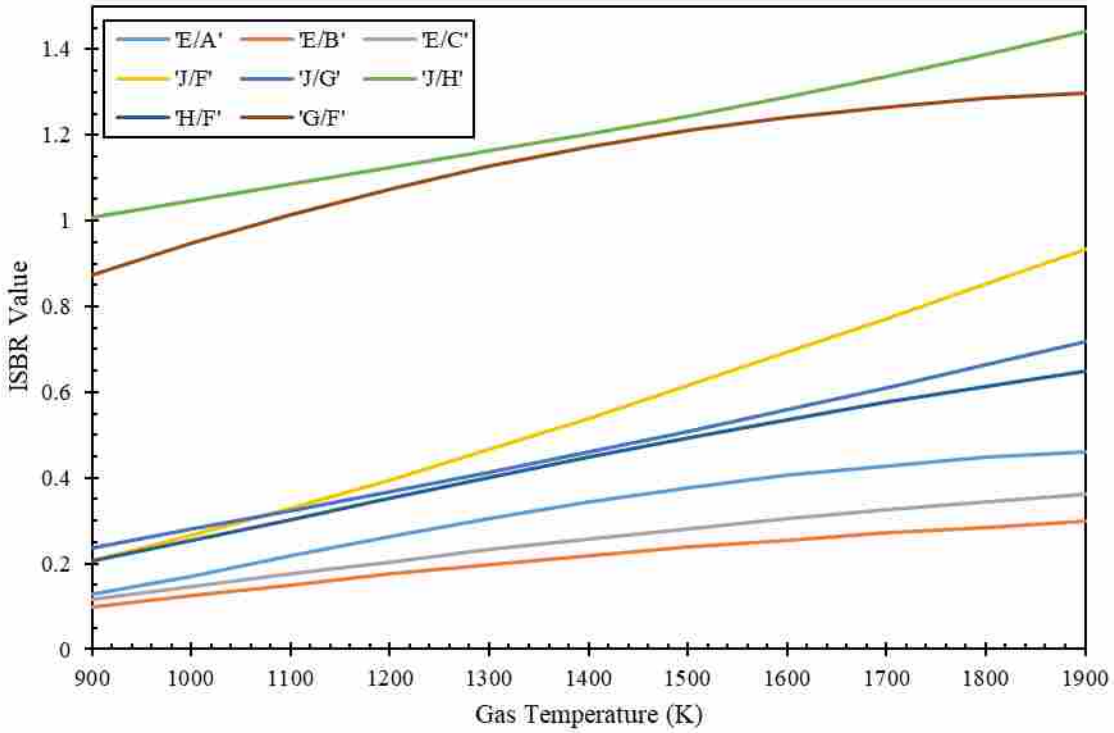

Figure 9: All correlation equations used in this work. Correlations shown were generated at a pressure of 1200 kPa, 6% water concentration, and pathlength of 15 cm.

Further analysis of all pressurized ISBR correlations was performed and will be discussed in Section 5. Comparable behavior was found between silica bands E/A, E/B, and E/C at pressure as were seen at atmospheric conditions, namely a stability with variations in non-temperature gas conditions. Sapphire bands did not exhibit this same behavior, and as such will not be emphasized in the results section of this work.

3.3 Fourier Transform Infrared Spectrometer

A Fourier Transform Infrared (FTIR) Spectrometer was used for this work. At the heart of an FTIR is an optical device known as a Michelson interferometer, which uses temporal

interference patterns of light to distinguish the wavelengths present in a given optical beam. A schematic of a Michelson Interferometer is shown in Figure 10.

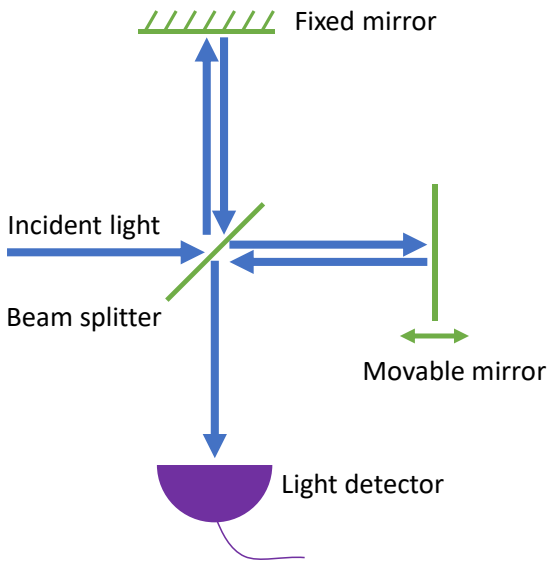

Figure 10: Schematic of a Michelson interferometer, a key component in an FTIR spectrometer. Light enters from the left of the diagram, is split before being recombined after traversing a pathlength difference, before signal intensity is measured at the detector shown at bottom.

In operating a Michelson interferometer, light to be measured is directed towards a beam splitting mirror, which is in turn oriented at a 45° angle from the incident beam of light. Nominally half of the beam is reflected and the other half is transmitted. Light reflected upwards is subsequently reflected by a fixed mirror (shown at top) back towards the beam splitter, where part is reflected out of the interferometer and another portion is transmitted towards the detector (shown at bottom). Also returning to the beam splitter is the light that was originally transmitted, after having been reflected by a movable mirror (shown at right). A portion of the beam returning from the movable mirror is transmitted, such that it leaves the interferometer, while the reflected portion continues towards the detector (shown at bottom).

For a monochromatic light source, were the pathlength traveled by the beam reflecting from the stationary mirror to match the pathlength of the beam reflecting from the moving mirror, the two beams would constructively interfere, and light would be seen by the detector. Identical behavior would occur if the pathlength difference between the two beams were an integer multiple of the wavelength of the light. If the pathlength difference were a half integer multiple of wavelength, $\Delta d = \lambda\left(n + \frac{1}{2}\right)$ where $n = 0,1,2\ldots$, the recombined beams would destructively interfere and no light would be seen at the detector. For a continuously moving mirror, this translates into a sinusoidal interference pattern at the detector known as an interferogram, as shown in Figure 11 for the case of a 2.0 μm beam of light.

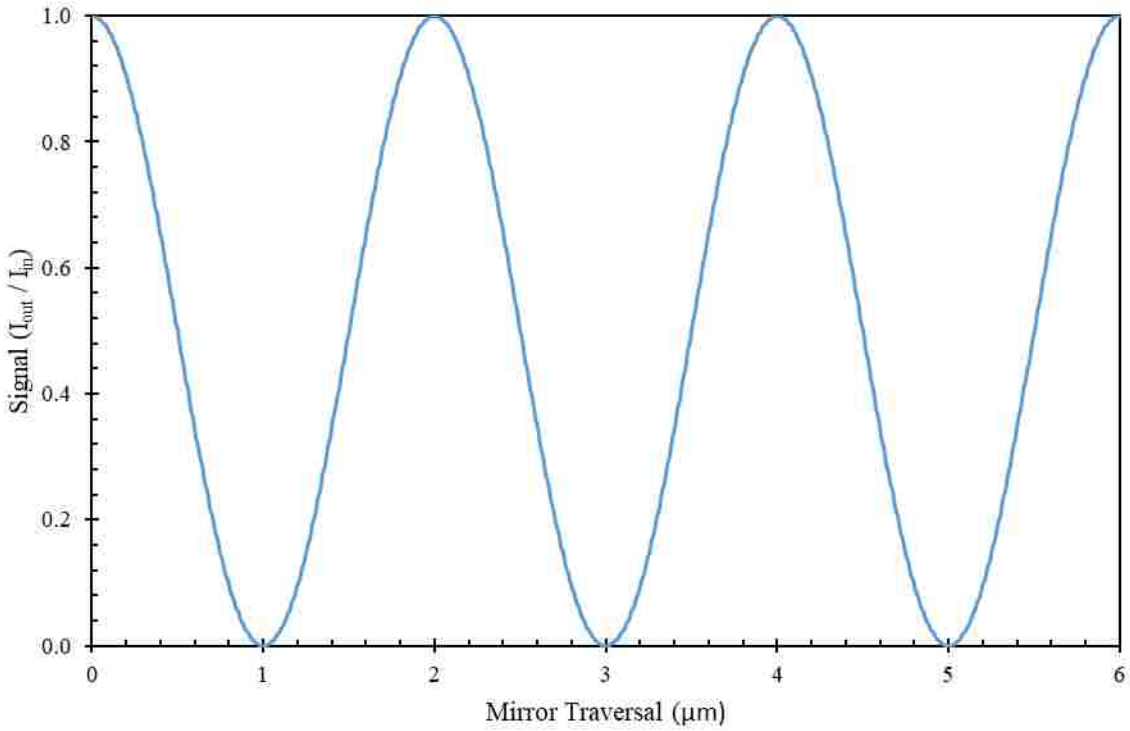

Figure 11: Interferogram obtained from a single wavelength at 2.0 μm incident into a Michelson interferometer.

For an incident beam containing multiple wavelengths of light, the measured interferogram deviates from a simple sinusoid, consisting of a central spike with fluctuating

decay in the wings, as shown in Figure 12 for the case of a Lorentzian peak centered at 2.0 μm with a half width of 2.0 μm.

The spectrum of light is obtained by taking the Fourier transform of the interferogram. The transform of a sine wave is a delta function centered at the spatial frequency, or wavenumber, of the beam. For the case of 2.0 μm light, this would result in a delta function at 5,000 cm^{-1}, units that can be converted to wavelength by taking the reciprocal. The Fourier transform for a more involved interferogram would likewise yield the spectra of light present in the beam in units of wavenumber.

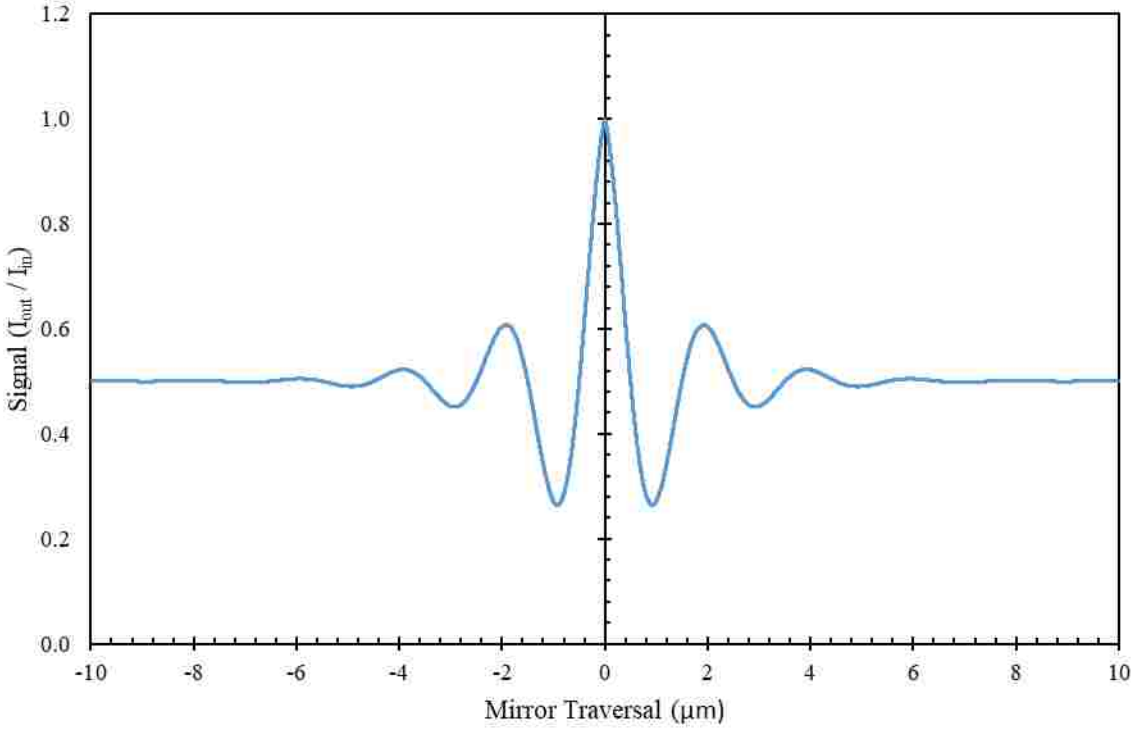

Figure 12: Interferogram obtained from a Lorenztian profile centered at 2.0 μm with a half width of 2.0 μm incident into a Michelson interferometer.

3.3.1 Apodizations and Zero Padding

In an idealized case, the path traveled by an FTIR mirror would be infinite in both directions, allowing the interferogram to likewise extend infinitely. Due to physical limitations, numerical methods are used to manage the finite nature of a measured interferogram. Two methods will be explored in this work: apodizations and zero padding.

As a mathematical explanation of the finite mirror traversal of an interferogram, the measured interferogram can be multiplied by an apodization, or apodizing, function. In the simplest case, a finite interferogram could be thought of as an infinite interferogram being multiplied by a boxcar function. The boxcar is a top hat function with a value of unity (which does not affect the spectra) wherever a data point is present, and a value of zero beyond the range of mirror movement, where no data exists. This is the apodization naturally occurring in finite interferogram processing. An example of a boxcar function is shown in Figure 13 for a mirror traversal of ±1 unit length. From the convolution theorem, the Fourier transform of two multiplied functions is the convolution of their individual Fourier transforms. Due to the sharp discontinuity present in the wings of the data, phantom frequencies are introduced, generating what appears to be noise in the measured spectrum of light [23].

A more sophisticated approach to apodization is the Happ-Genzel function, also shown in Figure 13. This function is used to reduce discontinuities and smooth the measured spectrum. Because the central spike in intensity is typically much narrower than the wings, as shown in Figure 11 where the spike is only 8 μm in width, the Happ-Genzel function largely impacts the wings of the spectra, smoothing the resultant spectrum with minimal degradation to spectral quality [23].

Another data processing technique in FTIR analysis is zero padding, or zero filling. When taking the Fourier transform of a finite interferogram with N data points, the output spectrum is also limited to N values. This can result in sharp transitions between neighboring peaks and the appearance of a low-resolution measurement. Adding zeros to the wings of the interferogram increases the number of data points in the resulting spectrum, smoothing the transition between peaks [23].

Neither technique discussed in this section is able to generate new information about the spectra that isn't already present in the interferogram. While judicious processing of interferograms is able to preserve information and reduce spectral noise, the impact of sophisticated apodizations and zero padding was found to be limited to wavelength scales much

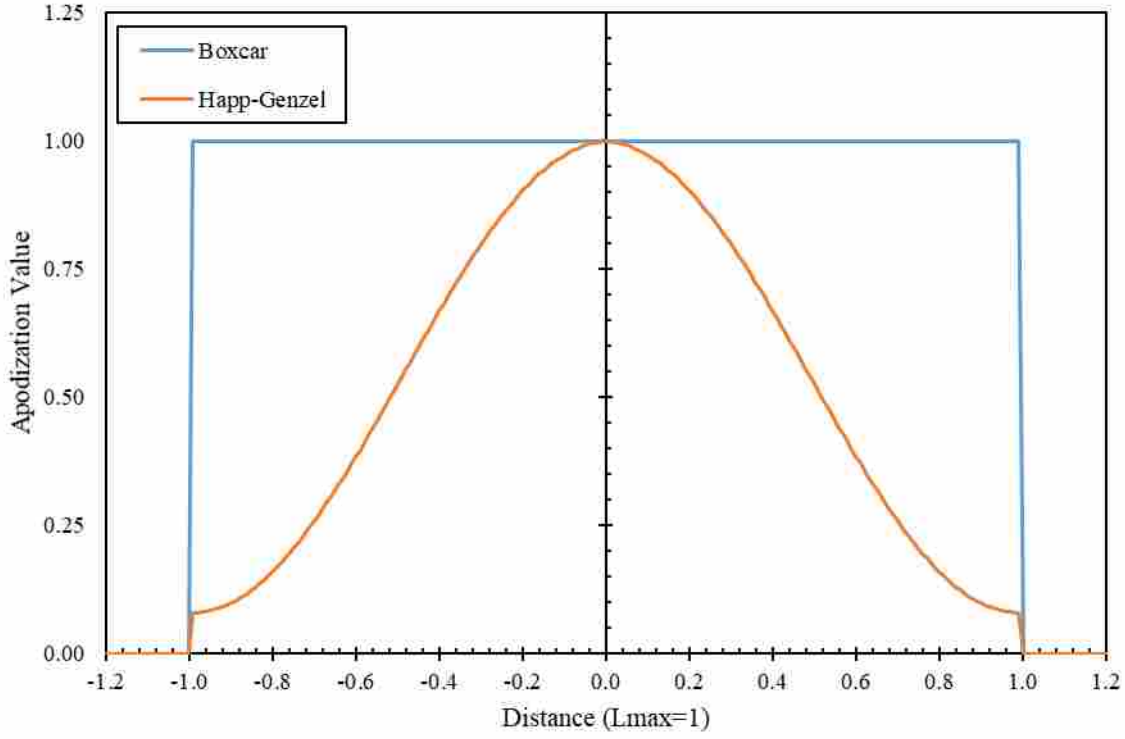

Figure 13: Example of boxcar and Happ-Genzel apodization functions used in FTIR interferogram processing.

smaller than the width of the spectral bands used (see Section 5.5.1). As such, a simple boxcar function without zero padding was used to process the data in this work.

3.4 Non-spectral Detectors

Current ISBR data processing utilizes an FTIR spectrometer such that the entire spectrum can be visualized and the measured data can be compared to modeled spectra. As the ISBR method matures, it is hoped that detectors and optical filters could be used in place of FTIR spectrometers. While FTIRs depend on moving mirrors to resolve spectra, a process that can take minutes to complete and requires a large physical footprint to house, detectors are able to collect data points at greater than kilohertz frequencies in very small packages.

Optical filters approximating bands C, E, B1, and B2 have been identified. Spectral transmission data for each filter is shown in Figure 14. Modified ISBR correlations have been computed based on the expected transmission of each spectral band and show promise for calculating gas temperatures.

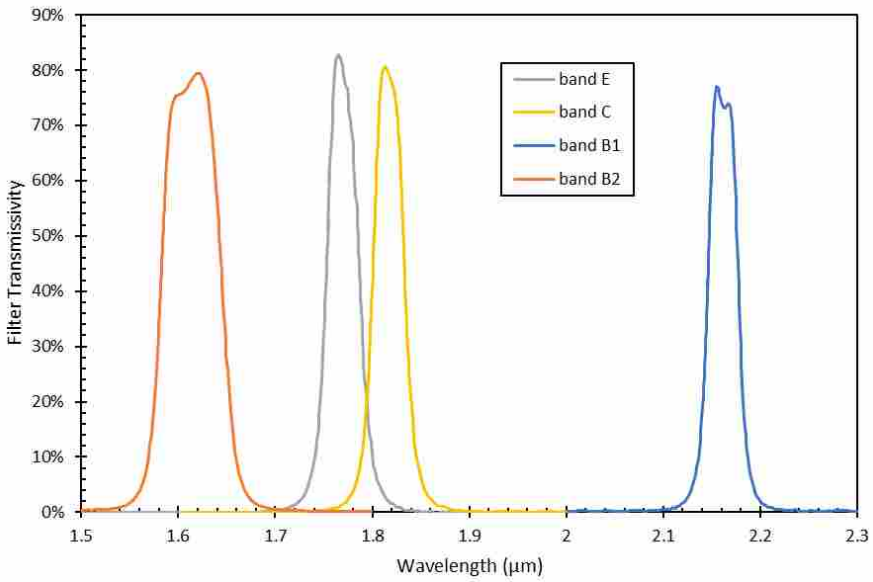

Figure 14: Optical filter spectral transmission for filters approximating ISBR bands E, C, B1, and B2.

An InGaAs detector containing four detective areas, each capped with one of the ISBR filters, has been ordered for future testing. The quad InGaAs detector is shown in Figure 15. An engineering drawing of the detector is shown in Appendix C for reference.

Figure 15: Quad (four element) InGaAs detector containing filters representing ISBR bands C, E, B1, and B2. A penny is included for a reference of scale.

4 EXPERIMENTAL METHOD

4.1 Data Collection

Testing for this work took place from May 15-18, 2018 at Solar Turbines facilities in San Diego, California in a pressurized combustor test rig running natural gas as the fuel. The physical combustion test rig and optical data collection system will be outlined.

4.1.1 Pressure Rig

Data were collected in a Solar Turbines test apparatus known as the pressure rig. It consists of a single combustor assembly placed in a flow-through pressurized cylinder nominally 30 cm in diameter, as shown in Figure 16. Flow diameter was constricted by a factor of two between the burner and all measurement devices. An optical probe was placed with the centerline 51.5 cm downstream of the burner exit. At the measurement location, the flow path was 15.2 cm in diameter. Emissions measurements were taken at two locations, 54.0 and 56.5 cm downstream of the burner. Two emissions probes consisted of a tube extending across the flow with multiple holes to sample a path averaged composition of gas into an analyzer. Three shielded k-type thermocouples were inserted 59.1 cm downstream of the burner, 7.6 cm downstream of the optical probe centerline, at various radial locations in the flow. Thermocouple shielding consisted of an exterior 6 mm (1/4”) stainless-steel tube with an interior electrically insulating sheath. Measurements taken using these thermocouples are referred to as the exhaust

temperature, in comparison to the optical temperature, or the temperature measured using the optical probe and ISBR method.

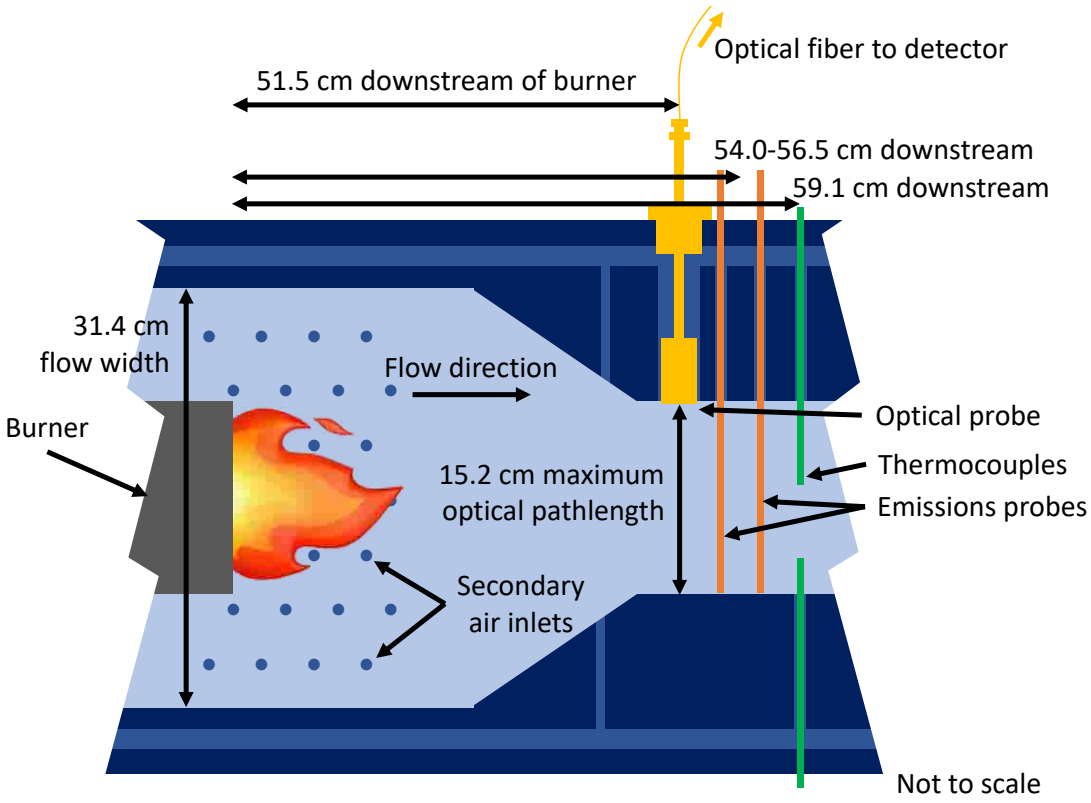

Figure 16: Schematic of pressure rig including the location of the optical, emissions, and thermocouple ports used for data collection.

Secondary air was added to the flow through various vents axially aligned with the combustor, marked as the secondary air inlets in Figure 16. It is believed that additional cooling air entered the flow path around a gasket at the flow restriction and around all measurement devices inserted into the flow. While the amount of air entering through these extraneous regions is likely small, it was not uniquely quantified for each location. Air entering the flow between the optical and thermocouple temperature measurement locations would have a significant impact on the relationship between the two temperatures and will be discussed as a source of error in the measurement.

The measurement consisted of two temperature sweeps at two loads or pressures. The temperature was varied by changing the fuel flow rate while holding air flow constant. The load was reduced by changing both fuel and air flow rate. The temperature swing was characterized by the calculated temperature of the primary zone (T_{PZ}) which was the adiabatic equilibrium temperature of the products using the fuel and air flow rate in the primary zone of the burner. A secondary zone temperature was also calculated representing the adiabatic equilibrium temperature of the products including primary and secondary air. Nominal flows and temperatures for the two load conditions are shown in Table 4. For reference, the stoichiometric air-fuel ratio (A/F) for methane, the primary component (94%) of the natural gas is 17.4 [24].

Table 4: Nominal operating conditions for the temperature swings at each load.

	High Load	**Low Load**
Preheated air temp (K)	641	579
Primary zone temperature (K)	1707 - 1891	1756 - 1888
Secondary zone temperature (K)	1159-1258	1168-1241
Pressure (MPa_{abs})	1.185	0.745
Air flow rate, total (kg/s)	2.01	1.29
Air-Fuel ratio (A/F)	62 - 74.7	59.7 – 67.5

4.1.2 Optical Probe

The optical probe designed for high pressure measurements parallels the probe designed by Tobiasson [4], only miniaturized and modified for operation in a pressurized environment without purge gas or cooling water. Sapphire was chosen as the material for both the lens and fiber due to its thermal and optical properties. Previous optical probes, such as the one used by Tobiasson, were water cooled to protect the probe and fiber cladding from melting, and to eliminate optical noise due to emission from the probe materials. The previous probes were also

nitrogen purged to removed cold water vapor from the flow path. Absorption by cold water vapor was found to be a significant source of error in ISBR measurements [4].

Given the 2.5 cm diameter dimensional constraint of the access port in the pressure rig, and the requirement that the probe seal the pressure inside the reactor, cooling and purging the probe was seen as impractical. It was determined that placing the probe in the flow path would reduce the need of nitrogen purge, as there would be no room for water vapor to cool between the flow and the probe. The low-OH silica fibers used previously have a temperature limit of 358 K and would not be suitable for such an application. Bare sapphire was chosen due to its optical transmission range of 1.0 to 3.0 μm as well as its softening point over 2300 K, well above the maximum exhaust temperature expected (Table 4). A spherical sapphire lens was used in place of a plano-convex lens to reduce the distance between the lens and the fiber and to fit within the smaller cavity of the probe. The focal length of a sapphire ball lens is on the order of 1 mm behind the lens compared to 20 mm for a plano-convex lens. A shorter focal length minimizes the potential for absorption and simplifies alignment of the lens and bare fiber. Flexibility and fiber brittleness are major drawbacks of using bare sapphire fibers. For the 425 μm diameter sapphire fiber used in this work, the minimum bend radius was restricted to 8 cm. Exposure of the bare fiber to accidental bumps further necessitated the use of thin stainless-steel tubing to protect the fiber.

A schematic of the optical probe is shown in Figure 17 with complete engineering drawings of the probe given in Appendix B.

A sapphire ball lens (item 7 in Figure 17) was housed at the front of a cylindrical outer shell (3). A set screw behind the lens (4) was used to secure the lens in position against the shell. A small hole was manufactured axially through the center of the set screw such that a sapphire

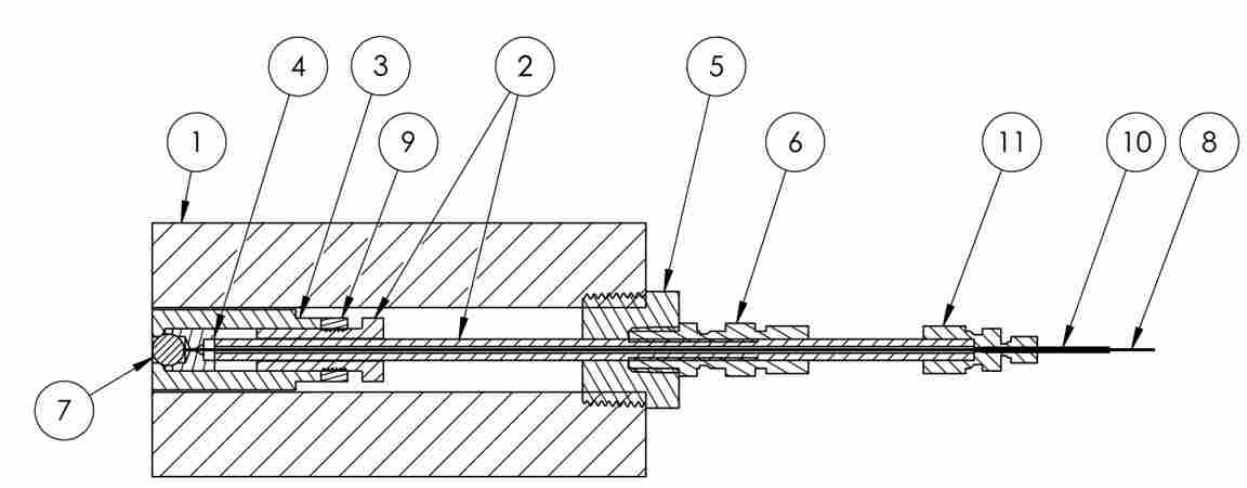

Figure 17: High-pressure optical probe assembly drawing. See Appendix B for complete engineering drawings of the high-pressure probe.

fiber could be placed through the set screw and at the focal point of the lens. A nominally 25 cm long piece of rigid 6.35 cm (1/4") diameter stainless-steel tubing both protected the fiber and secured the probe at a fixed depth in the pressure rig. A bolt was welded to the 6.35 cm diameter tubing such that the tubing and bolt assembly (2) could be attached to the outer shell (3). This arrangement allowed the fiber to be adjusted to the focus of the lens by turning the tubing and bolt assembly. A lock nut (9) was employed to prevent the system from moving during testing.

Thin walled, flexible 1.59 mm (1/16") diameter, 2-meter-long stainless-steel tubing was inserted a short distance into the 6.35 cm diameter tubing to protect the fiber between the optical probe and the detector. This flexible tubing was secured to the 6.35 cm diameter tubing with a pressure fitting. Graphite ferrules were used in the pressure fitting to allow the flexible tubing to move axially inside the thick tubing, allowing an additional method to align the fiber with the focal point of the ball lens.

The sapphire fiber was 425 μm diameter and nominally two meters long such that it could comfortably reach from the pressure rig to the collimator of the FTIR. Pressure was contained

using a 1” NPT plug (5), sealed against the 6.35 cm diameter tubing (2) with a pressure fitting, which was sealed against the 1.59 mm flexible tubing with a pressure fitting, which was finally epoxied into the fiber connector.

Pictures of the optical probe following testing are shown in Figure 18 and Figure 19. Color staining of the outer shell is the result of collecting calibration data with the optical probe inside the blackbody at temperatures in excess of 1300 K. A schematic of the testing layout is shown in Figure 20.

Figure 18: Top view of the optical probe without the 1.59 mm diameter flexible tubing or sapphire fiber (8 and 10 from Figure 17).

Figure 19: Isometric view of the optical probe without the 1.59 mm diameter flexible tubing or sapphire fiber (8 and 10 from Figure 17).

4.1.3 Optical Measurement System

Optical data for this work was collected using a Thermofischer Scientific Nicolet 6700 FTIR. The FTIR was purged with nitrogen gas to reduce absorption along the approximately 1 meter long internal pathlength. A KBr beam splitter with an advertised transmission range of 1.35-28 μm was used along with a HgCdTe detector with a detection range of 0.85-17 μm. The mirror had an advertised resolution of 0.125 cm^{-1}, 8 cm mirror pathlength equivalent travel. All measurements were the average of 16 individual scans, a process that took nominally one minute for each measurement.

Due to truncation error in the wavelength value of the FTIR HeNe laser reference laser, all measured wavelengths were shifted in wavenumber space by 0.167 cm^{-1} [4]. This shift is included to facilitate comparison between measured and modeled spectra and does not affect integrated intensity in any of the spectral bands as each is nominally 100 cm^{-1} wide.

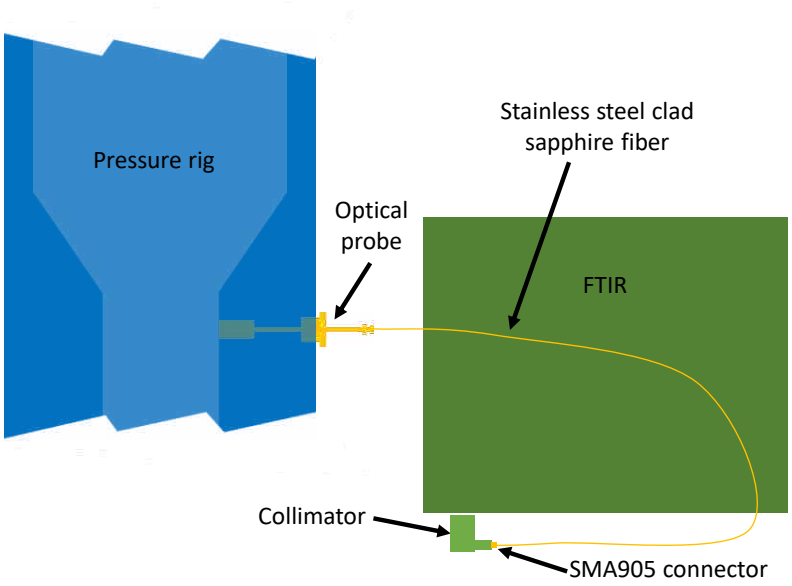

Figure 20: Schematic of the optical connection between the pressure rig and FTIR. Note that the stainless-steel clad sapphire fiber passes over the FTIR, with the light entering the FTIR at the collimator.

4.2 Calibration to Intensity

As part of operating the FTIR for the ISBR method, a calibration is required to convert the signal produced by the HgCdTe detector in volts to an incident intensity on the detector. This was accomplished by recording detector output while viewing a known signal intensity from a blackbody emitter at various temperatures. The calibration spectra contained unwanted cold-water vapor absorption due to humidity along the calibration optical path. This absorption was removed through a filtering process. A curve fit was then used to generate an equation for intensity as a function of measured voltage at each wavelength. This section details these processes, which are similar to those used by Tobiasson [4] with minor modifications to the filtering and curve fitting portions.

4.2.1 Collecting Calibration Data

Calibrations for this work were performed by orienting the optical probe at a blackbody emitter, as shown in Figure 21 capable of temperatures as high as 1400°C. Calibrations were performed while the FTIR was in position next to the pressurized rig. The collimator and optics within the FTIR remained unchanged for the measurement but the probe was moved from the calibration location and inserted into the pressure rig.

For each calibration, the optical probe was positioned between 0 and 10 cm from the blackbody cavity. Moving the probe in an axial direction closer to or further from the cavity changed the signal intensity, indicating that the solid angle view area of the probe was not filled by the blackbody cavity but also contained some unknown fraction of comparably cold refractory liner. The calibration obtained is therefore some fraction of the intensity that would be seen if the solid angle of the probe were filled, as is the case for pressure rig measurements where the probe is surrounded by emitting gas and walls.

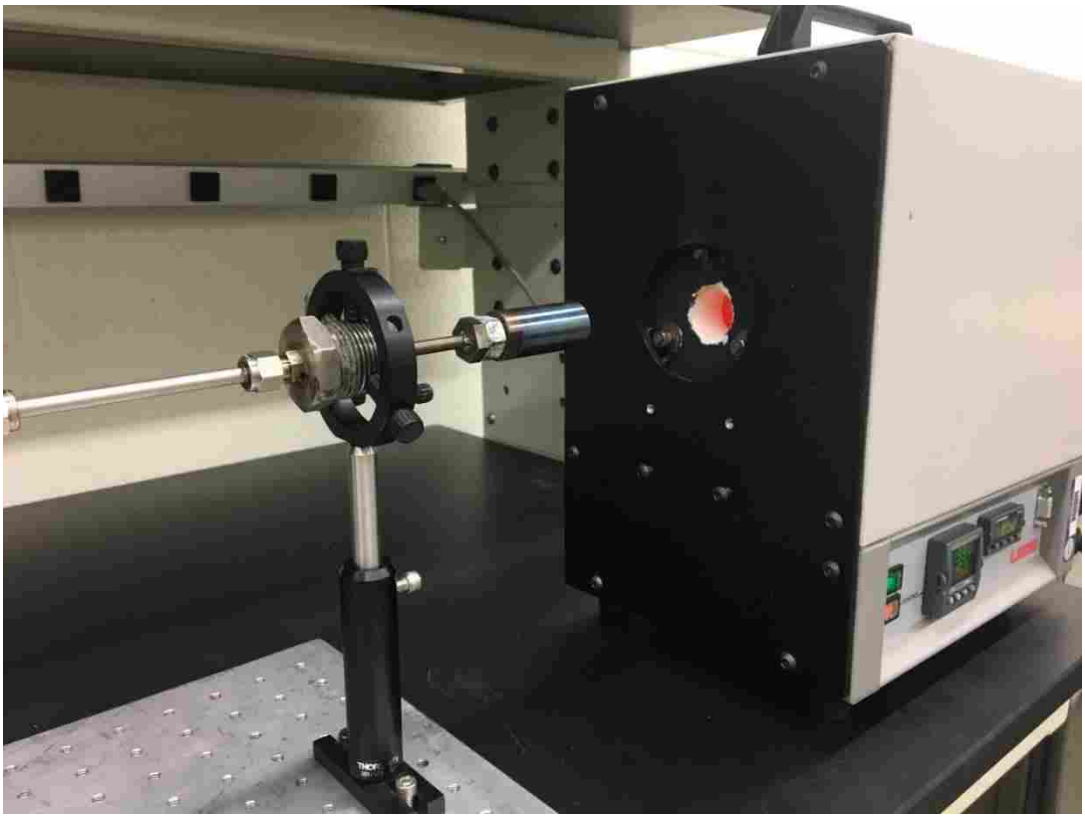

Figure 21: Calibration setup showing the high-pressure optical probe while viewing the blackbody. Because the optical probe view area is not collimated, the black refractory surrounding the blackbody cavity also occupied the view of the optical probe.

Over the experimental campaign, three calibrations were collected, each on the day prior to the subsequent day of data collection. An overview of each calibration is given in Table 5. Calibration 1 was done quickly prior to testing and did not cover the lower temperature range. Calibration 2 covers the widest range of temperatures and was taken with the spherical lens. Calibration 3 was taken without the spherical lens to explore the possibility of collecting data with a bare fiber. This calibration produced similar results to Calibration 2 but did not cover as large a temperature range. Calibration 2 gave the broadest range of intensities and was taken with a lens, comparable to the data evaluated in this work. As such, Calibration 2 will be used for data processing of the May 18 pressure rig data.

Table 5: Overview of each calibration taken during pressure rig measurements. Given the wide range of temperatures and the use of a spherical lens, Calibration 2 was used for data processing in this work.

Calibration	**1**	**2**	**3**
Date	5/15/19	5/16/19	5/17/19
T_{low} (°C)	1000	600	600
T_{high} (°C)	1400	1300	1100
ΔT (°C)	100	100	50
Number of points	5	8	11
Lens	Spherical	Spherical	None (bare fiber)
Distance from BB to probe (cm)	~10	~5	0

Planck distribution can be seen on the left side of the calibration where the sapphire is most transmissive. Attenuation above 2.7 μm is believed to be due to sapphire fiber attenuation, as the spectra clearly deviates from a Planck distribution. In addition to this signal attenuation, sharp peaks of spectral absorption can be seen, especially from 1.8 to 1.9 μm and 2.5 to 2.8 μm. This absorption matches the emissions peaks of water vapor shown in Figure 2 and is believed to be caused by water vapor (humidity) in the air. Absorption in the FTIR is minimized by a nitrogen purge. The air between the probe and the blackbody is not purged. This absorption presents a problem as it would not match conditions in the pressurized pressure rig. Because measuring intensity in these regions, especially the ISBR bands 1.6 to 2.2 μm, is crucial to temperature calculations, methods were explored for removing this absorption and will be discussed in the following section.

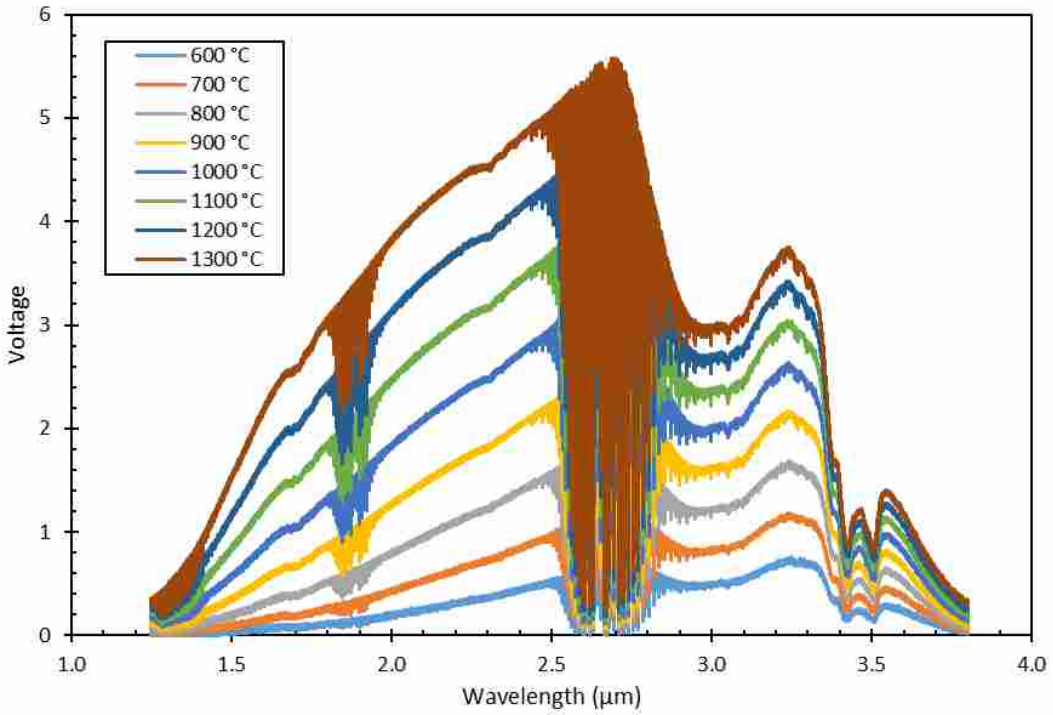

Figure 22: Raw spectral data files from Calibration 2 blackbody measurements.

4.2.2 Filtering Calibration Files

Calibration data were filtered and smoothed in order to remove absorption and obtain an accurate measurement of the detector response to incident intensity. The filtering was performed by identifying regions with strong participating media, namely H_2O, with CO_2 included for completeness. These regions were identified by modeling absorption for 7200 ppm H_2O and 400 ppm CO_2 and removing all data from regions with a cross section greater than $2.4 \cdot 10^4$ m^{-1}. Removed data points were replaced by interpolating across the missing sections, as is shown in Figure 23 for the Calibration 2, 1300°C spectrum. A 5th order low pass filter with a cutoff frequency of 0.004 ($\Delta\eta = 0.06$ cm^{-1}) was then applied to the entire spectrum to smooth the transition between filtered and unfiltered wavelengths and reduce measurement noise.

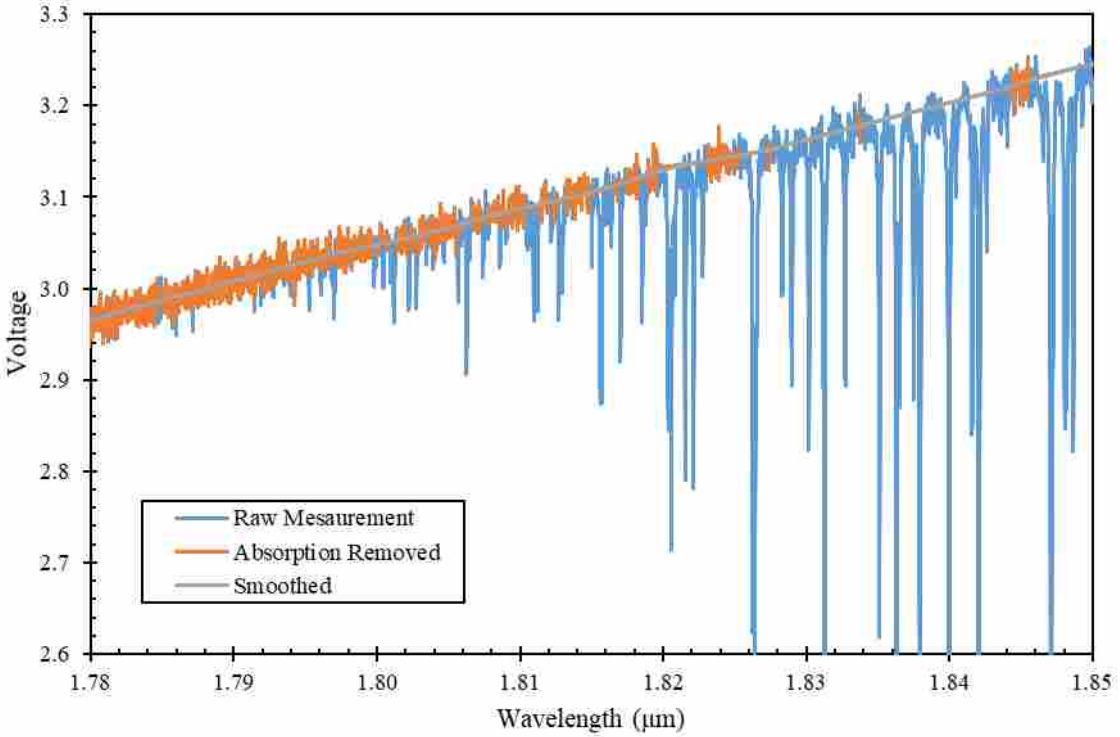

Figure 23: A depiction of the filtering process for the Calibration 2, 1300°C measured spectrum. Absorption peaks to be removed were identified using the HITEMP database. Missing regions were filled by interpolating neighboring points before a low pass filter was used to smooth the spectrum.

4.2.3 Calibration Equation

The desired outcome of the calibration process is to generate an equation with inputs of wavenumber and signal and an output of intensity. The eight temperature data points of Calibration 2 yield eight intensity-voltage pairs at each wavelength. Six equations were explored to create the best match between measured and curve-fit behavior. All equations explored are show in Table 6. Previous work by Tobiasson used a polynomial curve fit with an offset. "Power and exponential" and "exponential to power" equations, both without offsets, were obtained through a curve fit equation generator called ZunZun [25].

A sample of the eight intensity-voltage pairs at 1.800 μm is shown in Figure 24. The relationship between voltage and intensity is monotonic and very smooth. When viewing the

Table 6: Equations explored for use in calibrating voltage to intensity relationships

Equation Name	Behavior at origin	Equation
Polynomial	Offset	$A + Bv + Cv^2$
	No offset	$Bv + Cv^2$
Power and Exponential	Offset	$Av^B e^{Cv} + D$
	No offset	$Av^B e^{Cv}$
Exponential to Power	Offset	$Ae^{Bv^C} + D$
	No offset	Ae^{Bv^C}

entire intensity range shown in Figure 24(A), it is difficult to identify differences between the calibration equations. Focusing on the low or high end of the curve, significant differences emerge. Figure 24(B) shows the low end of the curve. Low intensities are particularly important due to their influence on the background wall temperature and because the large troughs of spectral gas emissions contain a significant fraction of the total gas emission energy. Data that do not pass through the origin were found to be problematic as will be seen in Section 5.5.3. The equation identified as "Power and Exponential No Offset" in Table 6 was selected for data processing. Results from other calibration curves are presented and discussed in Section 5.5.3.

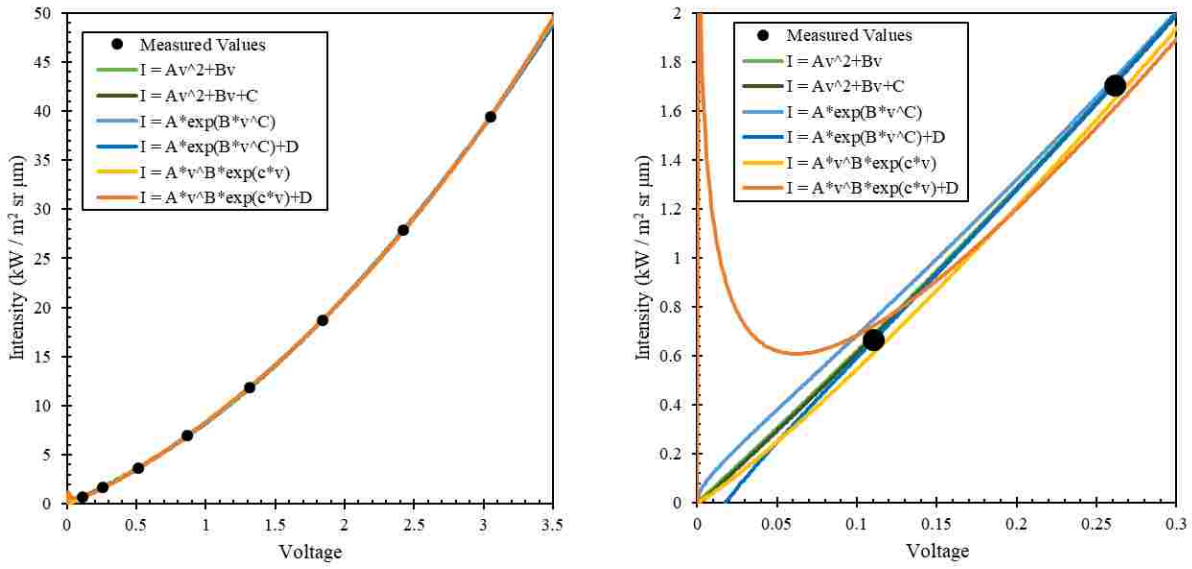

Figure 24: Calibration equation curve fits to measured data at 1.800 µm (A) over the entire measured range and (B) at low intensities.

5 RESULTS AND DISCUSSION

Pressure rig data were collected over the course of one week with data processing taking place in the succeeding months. As has been discussed, calibration data were taken prior to each day of testing (May 15, 16, and 17) with experimental data collected on the subsequent days (May 16, 17, and 18). This work will focus on the May 18th data, as circumstances allowed 30 optical and thermocouple data point pairs to be collected that day.

5.1 Test Conditions

May 18 testing consisted of two temperature sweeps, where air-fuel ratio was varied to change the gas temperature, at a unique simulated turbine load (pressure). Although some testing was conducted using a bare fiber, a sapphire ball lens was in place for all of data taken on May 18. Measured test cell data that define the operating conditions, including pressure, fuel and air mass flow rates, exhaust CO_2 concentration, theoretical primary zone flame temperature, and downstream temperature, were recorded by Solar, concurrent with optical temperature measurements. The Solar test cell data recorded for high and low load tests are listed in Table 7 and Table 8 at each of the 31 intervals when optical measurements were obtained. Data points 1-18 were taken during the first (high load) sweep with data points 20-31 during the second (low load) sweep. Data for point 19 were collected and saved but the flame became too lean and blew out before an FTIR scan could be completed. The test cell data for points 7 and 14 are seen to be

identical to their previous test cell data. For these two points, two optical measurements were obtained for a single recorded test cell operating point. A unique number was given to represent the optical data available.

From Table 7 and Table 8, it can be seen that the average pressure at high and low loads was 1180 ± 9 kPa and 744 ± 11 kPa respectively. Primary air was added through the burner or injector and secondary air or cooling air added through cooling passages and probe access ports along the axial length of the pressure rig. The total air flow was almost constant at 1.955 ± 0.005 kg/s at high load and 1.281 ± 0.007 kg/s at low load. The secondary air flow rate was approximately 25% higher than the primary air flow rate for the high load and 22% higher for the low load points.

The fuel flow rate was adjusted to produce a calculated primary zone temperature (T_{PZ}). T_{PZ} values are calculated based on combustion of the incoming fuel and air to the adiabatic equilibrium temperature of the products, and are based on the primary air inlet temperature, the primary air flow rate, and the fuel flow rate. The incoming air was heated to 641 K for the high load sweep and 579 K for the low load sweep, therefore it was necessary to have a slightly richer A/F ratio for the low load sweep in order to produce the same primary zone temperatures at low load. This can be seen in the A/F ratio data, which changes from 62 to 74 at high load and from 59.7 to 67.1 at low load. The result can also be seen in the CO_2 concentration, which is slightly higher for the low load sweep at the same T_{PZ} temperature as the high load sweep.

An equilibrium adiabatic flame temperature for the complete fuel air mixture, after primary gases have mixed with the secondary air stream, is shown in the column labeled Sec. Zone Temp. This calculated adiabatic equilibrium temperature is very close to the average of the three thermocouple temperatures shown in the final column. For the high load cases, the

Table 7: Pressure rig data taken for high load data points. No Solar data were taken concurrent with optical measurement 19 due to flame extinction halfway through the nominally minute long optical data collection process.

Data Point	Pressure (kPa)	Fuel Flow Rate (kg/s)	Air Flow Rate (kg/s)	Sec. A/F	CO_2 Conc. (% vol)	Prim. Zone Temp. (K)	Sec. Zone Temp. (K)	Ex. T.C. 1 (K)	Ex. T.C. 2 (K)	Ex. T.C. 3 (K)	Ex. Temp. Avg. (K)
1	1187	0.0316	2.01	62.0	3.06%	1884	1255	1286	1162	1325	1258
2	1187	0.0316	2.00	62.0	3.09%	1886	1257	1287	1164	1327	1260
3	1191	0.0316	2.00	61.7	3.10%	1891	1258	1290	1166	1330	1262
4	1185	0.0296	2.01	66.2	2.97%	1820	1221	1267	1117	1296	1227
5	1182	0.0296	2.01	66.2	2.97%	1821	1221	1268	1117	1297	1227
6	1183	0.0297	2.01	66.0	2.98%	1822	1221	1269	1121	1299	1229
7	1183	0.0297	2.01	66.0	2.98%	1822	1221	1269	1121	1299	1229
8	1178	0.0286	2.00	68.4	2.86%	1790	1204	1258	1095	1283	1212
9	1186	0.0286	2.01	68.3	2.84%	1790	1204	1256	1092	1283	1210
10	1186	0.0286	2.00	68.3	2.85%	1791	1204	1256	1091	1281	1210
11	1171	0.0278	2.00	70.2	2.71%	1767	1191	1246	1080	1271	1199
12	1174	0.0278	2.00	70.4	2.72%	1762	1190	1245	1079	1270	1198
13	1184	0.0278	2.01	70.4	2.71%	1763	1190	1244	1076	1269	1196
14	1184	0.0278	2.01	70.4	2.71%	1763	1190	1244	1076	1269	1196
15	1174	0.0271	2.01	72.2	2.52%	1738	1176	1232	1065	1257	1185
16	1178	0.0271	2.01	72.3	2.49%	1735	1174	1230	1062	1255	1182
17	1161	0.0262	2.01	74.7	2.32%	1707	1159	1217	1054	1240	1170
18	1160	0.0262	2.01	74.7	2.33%	1707	1159	1217	1055	1240	1171
19	N/A	N/A	N/A	N/A	N/A	N/A	N/A	N/A	N/A	N/A	N/A

Table 8: Pressure rig data taken for low load data points.

Data Point	Pressure (kPa)	Fuel Flow Rate (kg/s)	Air Flow Rate (kg/s)	Sec. A/F	CO_2 Conc. (% vol)	Prim. Zone Temp. (K)	Sec. Zone Temp. (K)	Exh.T.C. 1 (K)	Exh. T.C. 2 (K)	Exh T.C. 3 (K)	Exh. Temp. Avg. (K)
20	736	0.0216	1.29	59.7	3.64%	1879	1237	1240	1110	1297	1216
21	757	0.0216	1.29	59.3	3.65%	1888	1241	1242	1113	1301	1219
22	768	0.0216	1.30	59.6	3.63%	1882	1237	1240	1110	1299	1216
23	741	0.0202	1.29	63.7	3.38%	1814	1201	1216	1072	1267	1185
24	745	0.0202	1.29	63.5	3.40%	1818	1202	1219	1072	1266	1186
25	751	0.0202	1.29	63.6	3.37%	1815	1201	1217	1071	1265	1184
26	739	0.0198	1.30	65.0	3.26%	1791	1187	1206	1062	1254	1174
27	740	0.0197	1.29	65.2	3.27%	1788	1187	1206	1062	1252	1173
28	748	0.0197	1.29	64.8	3.23%	1795	1188	1206	1059	1252	1173
29	732	0.0190	1.29	67.2	2.97%	1760	1168	1190	1047	1238	1158
30	735	0.0190	1.29	67.5	2.98%	1756	1168	1192	1050	1236	1159
31	736	0.0190	1.29	67.1	2.97%	1763	1171	1193	1049	1237	1160

adiabatic calculated temperature is slightly lower than the average thermocouple measurement (2 - 12 K) while at low load the calculated adiabatic temperature is slightly higher (10 - 20 K). One would expect a measured thermocouple temperature to be significantly lower than a calculated, adiabatic temperature, especially before correcting for radiative losses of the thermocouple. This parity of adiabatic and measured temperatures suggests that not all of the secondary air has been mixed into the products at the measured thermocouple locations. This observation is also consistent with the CO_2 measurement taken between the optical probe and the thermocouple, which is approximately 10% higher than the calculated equilibrium concentration including all primary and secondary air.

Figure 25 shows a plot of primary and secondary zone calculated temperatures, thermocouple temperatures, and primary zone air fuel ratio from the tabular data in Table 7 and Table 8. The low load sweep produced the same higher primary zone temperatures but the high load sweep was able to go to a lower T_{PZ} temperature before the flame blew out. The secondary zone and thermocouple temperatures are seen to shift in the same direction as the calculated T_{PZ} temperatures but with smaller changes than are seen in the T_{PZ} temperatures.

Although they are measured at the same axial location in the pressure rig, thermocouple temperatures are significantly different. This indicates that mixing is still incomplete and the radial temperature profile, even downstream of the optical measurement, is far from uniform. The impacts of this non-uniformity on optical temperature measurements will be further explored. Of the three thermocouples, temperatures measured by thermocouple 3, T_3, were consistently highest, followed by T_1, and T_2 as the lowest. Table 9 shows the average offset between thermocouple readings at high and low load. The largest difference between an individual thermocouple and the average is on the order of 9%. Given the unknown radial

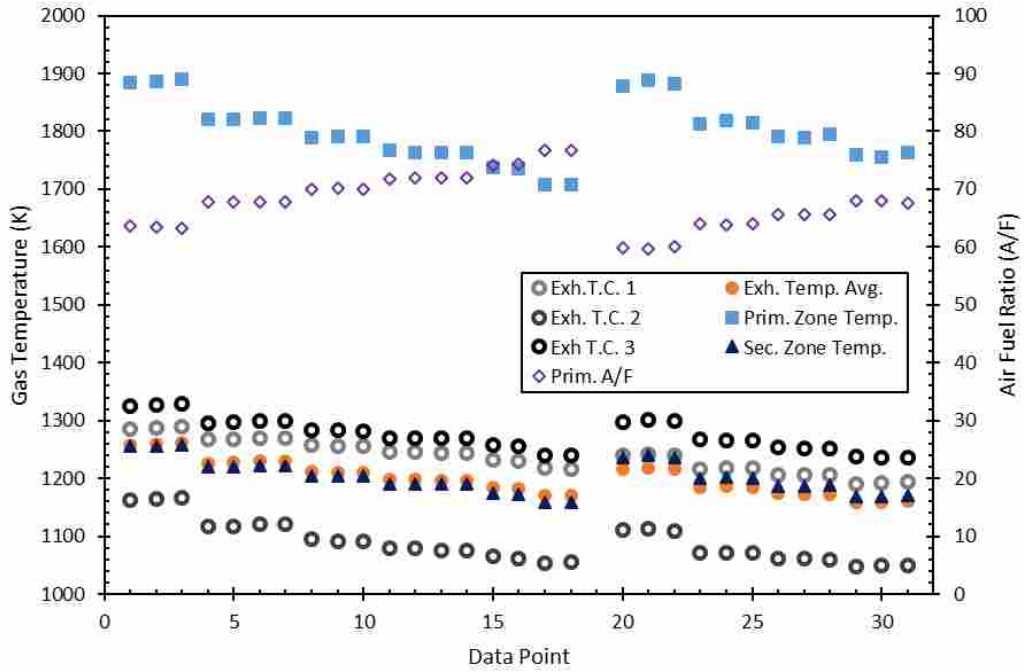

Figure 25: Calculated primary and secondary zone temperatures, measured thermocouple temperatures, and air fuel ratios as taken from tabulated testing data.

locations of the thermocouples and large spatial variations, the accuracy of the average temperature in representing a mass average is difficult to assess but is estimated to be in a worst case, ± 40 K, or on the order of 3% of the average thermocouple reading.

Table 9: Thermocouple offset from average temperature values. All values given in Kelvin (K).

	T_1-T_{avg}	T_2-T_{avg}	T_3-T_{avg}	T_{PZ}-T_{avg}
high load	42±7	-113±9	70±2	569±24
low load	30±4	-111±3	80±2	620±21

In addition to positional uncertainty, thermocouple readings varied with time. While this behavior is not fully captured for an individual data point, the variation in thermocouple measurements for data points under identical test conditions was used to estimate the change in thermocouple temperature as a function of time. A maximum change of just over 4 K was

observed, occurring for data points 1 - 3. A temporal uncertainty is therefore perhaps negligible, but was estimated at ± 3 K.

Thermocouples are well known to have radiative losses and can produce temperatures significantly lower than the temperature of the gas they are measuring [5, 6, 7]. In this case, radiation would largely be exchanged between the stainless-steel radiation shield of the thermocouple probe and the pressure rig wall. The pressure rig wall will later be shown to have an optically calculated temperature and emissivity on the order of 750 - 850 K and 0.4, respectively. As the calculated emissivity was lower than what would be expected for a refractory liner, this and other properties were varied to gain an understanding of radiative loss uncertainty. Gas temperature was approximated as 1400 K with a velocity of 35 m/s calculated based on measured mass flow rates. Convective heat transfer was modeled as a cylinder in crossflow with a value of 630 W / m^2 K [20]. A conservative estimate for radiative losses based on an energy balance yielded an estimated measurement bias of -175 K with a random uncertainty of ± 30 K. A schematic of the energy balance employed is shown in Figure 26.

Random uncertainties for positional, temporal, and radiative losses are compiled in Table 10. The total random uncertainty, calculated as the root mean square of the individual uncertainties, was found to be ± 50 K, with the measurement bias of -175 K due to radiative losses.

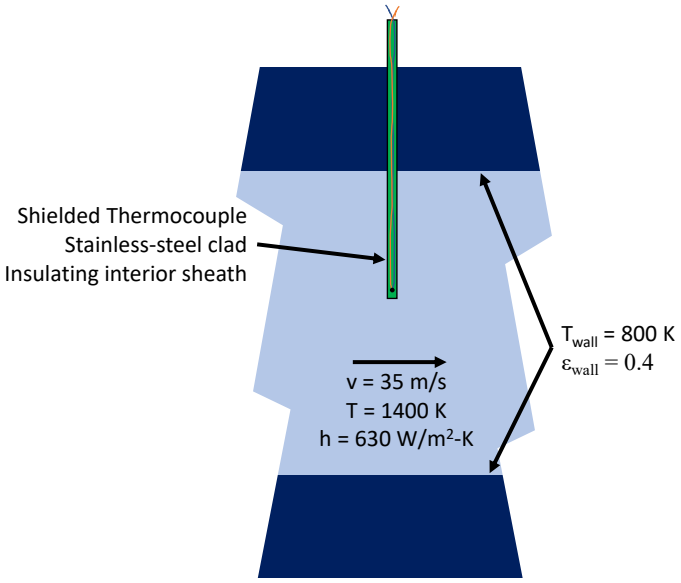

Figure 26: Schematic diagram of the energy balance used in assessing thermocouple radiative losses.

Table 10: Sources and total random thermocouple uncertainty.

	Uncertainty (K)
Positional	± 40
Temporal	± 3
Radiative Loss	± 30
Total	± 50

5.2 Optical Temperatures, ISBR Method

Gas temperatures were calculated for each data point using the ISBR method, as described in Section 3.2 with results from ISBR calculations shown in Table 11 for high and low load measurements. Included in the table are the calculated optical temperatures for each of the ISBR temperature ratios used, an average optical temperature, an optically calculated wall temperature and emissivity, and the calculated SAR. Each of the ISBR ratios yielded a unique estimate of the gas temperature. The offset of each ratio from the average optical temperature

was found to be consistent at an average of 4 ± 4 K, -23 ± 4 K, and 18 ± 2 K for ratios $T_{E/A}$, $T_{E/B}$, and $T_{E/C}$, respectively. The maximum difference in optical temperatures, $T_{E/C}$ - $T_{E/A}$, is 41 ± 4 K. Due to the fairly constant offset, the average optical gas temperature will be used as a representative value of optical gas temperature when individual gas temperatures are not used.

Table 11: Optical gas properties for both high (1-19) and low (20-31) load testing as calculated using the ISBR method with area ratios.

Data Point	Gas Temp. E/A (K)	Gas Temp. E/B (K)	Gas Temp. E/C (K)	Gas Temp. Average (K)	Wall Temp. (K)	Wall Emissivity	Solid Angle Ratio
1	1466	1424	1475	1455	864	0.351	3.20
2	1494	1450	1497	1480	867	0.379	2.97
3	1495	1452	1497	1481	877	0.340	2.99
4	1443	1420	1459	1441	839	0.388	2.99
5	1440	1404	1448	1431	857	0.320	3.04
6	1452	1427	1466	1449	834	0.417	2.89
7	1434	1405	1449	1429	839	0.366	3.07
8	1424	1406	1445	1425	826	0.396	2.97
9	1412	1387	1431	1410	820	0.403	3.08
10	1425	1396	1437	1419	832	0.367	2.98
11	1409	1387	1420	1405	813	0.403	3.02
12	1414	1391	1428	1411	811	0.401	3.05
13	1396	1373	1412	1394	828	0.323	3.14
14	1406	1382	1424	1404	810	0.403	3.06
15	1409	1395	1425	1410	791	0.456	2.97
16	1399	1378	1416	1398	789	0.437	3.14
17	1378	1361	1402	1381	783	0.406	3.60
18	1374	1355	1391	1373	780	0.389	3.35
19	-	-	-	-	-	-	-
20	1458	1427	1471	1452	816	0.382	2.87
21	1460	1427	1472	1453	819	0.398	2.87
22	1461	1418	1465	1448	816	0.397	2.86
23	1414	1388	1432	1411	796	0.380	2.88
24	1428	1396	1436	1420	785	0.436	2.78
25	1436	1411	1449	1432	796	0.403	2.69
26	1405	1377	1421	1401	778	0.414	2.83
27	1410	1389	1427	1408	767	0.479	2.78
28	1408	1381	1423	1404	787	0.360	2.85
29	1382	1360	1399	1380	752	0.441	3.06
30	1393	1367	1413	1391	748	0.474	2.94
31	1394	1367	1407	1389	756	0.451	2.91

Optically calculated wall temperatures ranged from 826 ± 29 K at high load to 785 ± 25 K at low load, with emissivities of 0.386 ± 0.036 and 0.418 ± 0.038, respectively for high and low load. The measured emissivities are within expected values for a refractory surface at 800 K, and, as will be shown in Section 5.5.2, optical wall properties show good agreement with the measured spectra. Solid angle ratio (SAR) values were similar, though significantly different, between high and low loads, at 3.08 ± 0.17 and 2.86 ± 0.09 respectively. The SARs are also reasonable when comparing the solid angle of the sapphire lens to blackbody surface and the total solid angle that could be viewed by the fiber. It is expected that both values would remain relatively constant over all data points collected. While processing the data it was found that very small differences in the shape of the calibration curve fits at low intensity had a large impact on SAR and wall emissivity. The calibration fit selected, "Power and Exponential No Offset" in Table 6, was found to produce minimal variation in wall emissivity and SAR, as will be discussed in Section 5.5.3.

All three optical temperatures were plotted against the average exhaust temperature for high load measurements (1-18), as shown in Figure 27. A linear relationship can be seen between optical and average exhaust thermocouple temperatures. Linear fits were calculated for each ISBR ratio and the slope of each line was found to be nearly equivalent at 1.03 ± 0.14 $K_{optical} / K_{exhaust}$, where $K_{optical}$ is the optical temperature and $K_{exhaust}$ is the exhaust temperature, of that the optical temperature changes by 1.03 K per every 1 K change in exhaust temperature. This result suggests that optical temperatures register a very similar, though slightly larger temperature change with changing gas temperature than thermocouples. This could be explained based on previous discussion of thermocouple radiation losses, which would have a greater impact at higher temperatures.

Scatter in optical temperature at a given T_{PZ} is caused by small variations in the integrated band intensity. Scatter for ISBR temperatures varies from 5 to 26 K, or on the order of 1% of the measured value. Scatter for thermocouple, T_{PZ}, and secondary zone temperatures

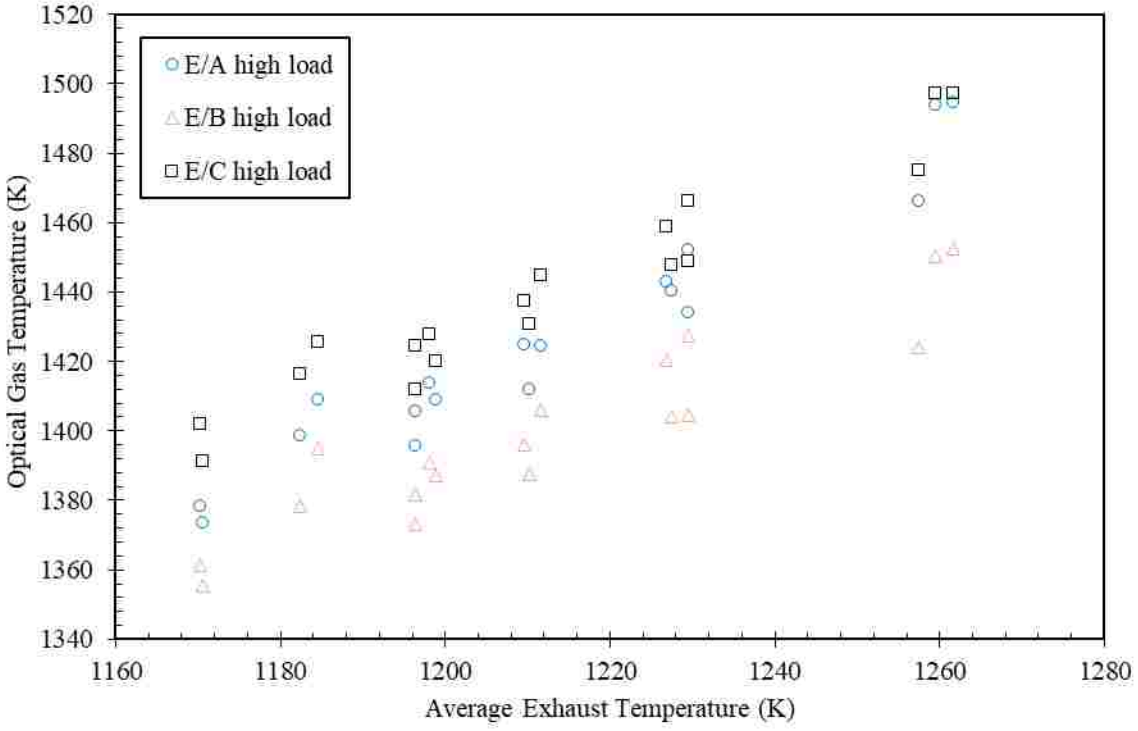

Figure 27: Calculated ISBR optical gas temperatures as a function of average exhaust temperature for high load data points (1-18).

varies from 1 to 4 K, 0 to 9 K, and 0 to 4 K, respectively. This scatter is believed to be random. Due to time involved in taking each FTIR data point, fewer replicates could be taken. It is believed that the rapid data sampling available while using detectors and optical filters will allow for improved measurement averaging, reducing random uncertainty.

An average temperature offset of 210 ± 19 K was found between optical and uncorrected thermocouple temperature measurements. This offset is likely caused by radiative losses of the thermocouples (-175 K), in addition to dilution of the flow with additional cooling air between the optical and thermocouple ports, other uncertainty in the thermocouple temperature as

discussed, heat loss of the gas between the optical and thermocouple measurements, and uncertainty in ISBR temperature to be discussed in more detail.

In addition to a temperature offset from thermocouple values, a temperature difference between $T_{E/A}$, $T_{E/B}$, and $T_{E/C}$ can be clearly seen in Figure 27. This offset between optical temperatures, along with general ISBR temperature uncertainty, could be caused by:

1) Uncertainty in wall temperature and emissivity shifting the spectra.
2) Calibration error at low intensities causing uncertainty in wall conditions and other low intensity portions of the spectrum.
3) Incorrect SAR and other issues arising from poorly collimated optical measurements.
4) Non-uniform gas temperature profiles.
5) ISBR input property uncertainty, including incorrect H_2O concentrations and variable pathlengths due to poorly collimated light.
6) Errors in modeled spectra.
7) Errors in the measured spectra due to FTIR resolution

Each of these potential sources of error, along with signal-to-noise levels present, will be discussed in Section 5.5, Sources of Error.

Low load optical measurements were plotted against thermocouple values, as shown in Figure 28, with similar results to those observed in Figure 27. The average slope of linear fits through each optical temperature is 1.10 ± 0.10 $K_{optical}$ / $K_{exhaust}$, comparable to that seen at high load conditions. The temperature offset between optical and uncorrected thermocouple measurements also increased slightly to 232 ± 19 K at low load. Comparable magnitudes of each ISBR temperature ($T_{E/C} > T_{E/A} > T_{E/C}$) and scatter in temperatures can also be seen. In general,

trends observed under high load conditions are present at low load, leading to a similar uncertainty in optical temperature independent of measurement pressure.

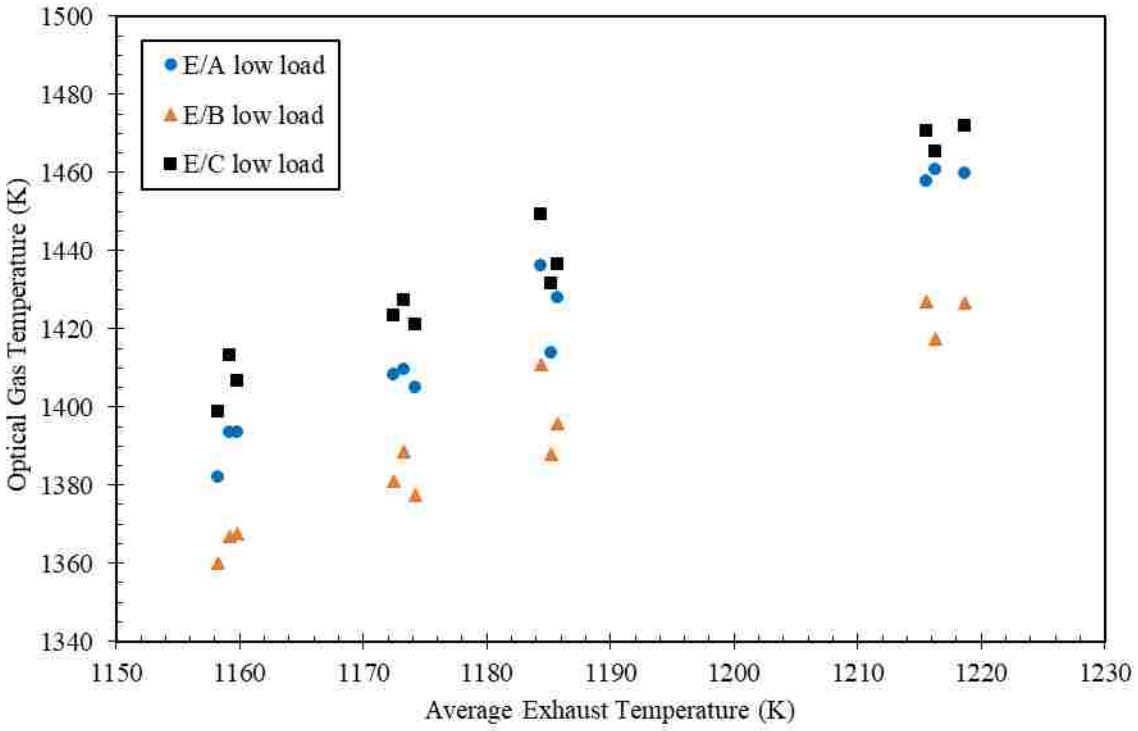

Figure 28: Calculated ISBR optical gas temperatures as a function of average exhaust temperature for low load data points (20-31).

Average ISBR temperature measurements for high and low load, along with T_{PZ} and secondary zone temperatures were plotted as a function of average thermocouple temperature, as shown in Figure 29. The average optical temperature was found to be lower than the adiabatically calculated primary zone temperature, as would be expected. The optically calculated temperature was higher than the adiabatic secondary zone temperature. While this behavior is non-physical, it should be noted that thermocouple measurements downstream of the optical measurement were nominally equal to adiabatic secondary zone temperatures before considering the 175 K radiative loss bias calculated previously, calling into question the mixing

rate of primary and secondary air, as has been discussed. Low load temperatures were found to be higher than high load temperatures at the same average exhaust thermocouple temperature for all three temperatures shown. Note that the average optical temperatures are shifted by the same amount as the average exhaust thermocouple between the high and low load measurements.

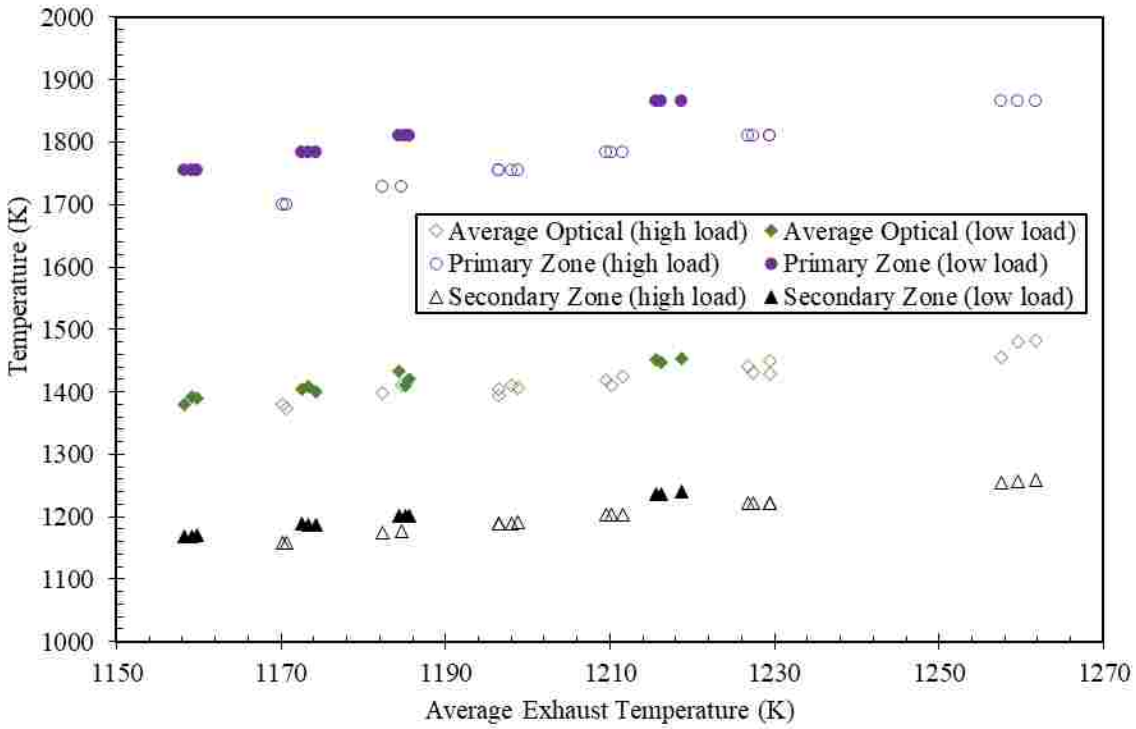

Figure 29: Average ISBR optical gas temperature, primary zone temperature, and secondary zone calculated temperature as a function of average exhaust temperature for all data points.

In spite of the random error seen, the standard error for the line of best fit, a measure of the accuracy of the predicting value of the linear fit, for exhaust temperature as a predictor of optical temperature was 14 $K_{exhaust}$ for all data points at high and low load. This value represents a lower bound of ± 14 K uncertainty on the predicting ability of a linear fit between optical and thermocouple temperatures.

As outlined in the preceding paragraphs, sources of optical temperature uncertainty were tabulated and will be discussed in Section 5.5. The result of this evaluation is shown in Table 12. The largest source of uncertainty was found to be due to input conditions to the ISBR algorithm, particularly uncertainty in water concentration and the potential for concentration gradients. From modeling work performed, temperature gradients and general signal-to-noise were also found to be large sources of error. It is not believed that the poorly collimated view area had a significant effect on the calibration beyond the variation in signal strength.

Table 12: Sources and total optical temperature uncertainty.

Source	Uncertainty (K)
Signal-to-noise	± 25
Wall temperature	± 20
Calibration at low intensity	± 20
Non-collimated view	± 15
Temperature gradients	± 25
ISBR input property uncertainty	± 50
Discrepancies with HITEMP	No value assigned
Total	± 70

Taking the root mean square of the values in Table 12 yields a total uncertainty of ± 70 K for optical temperature measurements in this work. The offset between optical and radiation thermocouple measurements was 44 ± 14 K for all measurement conditions. Based on the optical uncertainty of ± 70 K and the random thermocouple uncertainty of ± 50 K, promising agreement can be seen between optical and radiation corrected thermocouple measurements. Both optical and corrected thermocouple measurements were significantly larger than the theoretical maximum secondary zone temperature at 217 ± 8 K and 173 ± 12 K higher than T_{sec}, respectively, indicating potential for delayed mixing of the secondary air or additional uncertainty in the mass flow rate values from which secondary temperature is calculated.

Measured CO_2 concentrations at 10% higher than expected secondary zone concentrations further calls into question secondary zone temperature predictions. Additional investigation is required to definitively validate the magnitude of the temperature calculated using the ISBR method at pressure.

5.3 Spectral Model Compared to Measurement

Additional insight can be gained by evaluating the agreement of spectral measurements and the HITEMP model used to correlate them to gas temperature. Figure 30 shows data points 4 through 7 along with a spectral model at the average measurement conditions for the four data points. A portion of the band C spectrum was selected and is representative of behavior throughout the measurement region. As can be seen, there is a measured peak for every modeled peak. The modeled peaks are about the same width as the measured peaks. Measured peaks are also reproducible, and either consistently match, are smaller than, or are larger than the measured peaks at any given wavelength. It should be noted that the measured and modeled spectra are forced to have the same integrated intensity, over bands A through E by adjusting the SAR. Thus, if these wavelengths shown appear to have an average measured intensity higher than the modeled intensity, the regions of the spectrum not shown will balance out the difference. Wiggles, or high frequency variations in the measured data, not found in the modeled data can also be seen. This is thought to be caused by apodization of the measured interferogram and noise as described in the Section 5.5.1.

Measured to modeled spectral agreement was also found with changes in pressure. Figure 31 shows measurements 10 and 24, a high and a low compared to modeled data at high and low load. Both loads are at almost the same temperature 1419 and 1420 K, respectively. Comparable

behavior can be seen for measured intensity spectra 8-10 and 23-25. Only one of each was included for visual clarity. Modeled conditions at high and low load reflect the

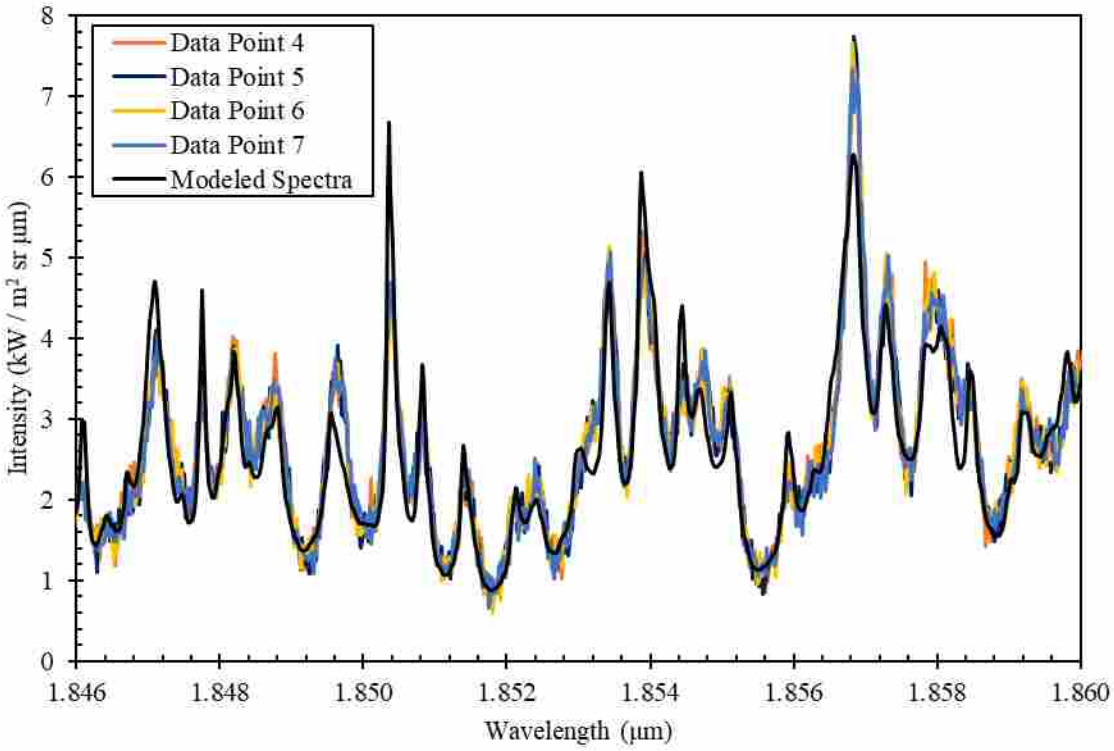

Figure 30: Measured spectra for data points 4-7 (high load, T_{PZ} = 1821 K) with modeled spectra generated for a 15 cm pathlength of 2.98% CO2 and 5.96% H2O at 1183 kPa and 1438 K with a far wall at 842 K and a wall emissivity of 0.373. An SAR ratio of 3.0 was used to scale all measured spectra. Values used reflect average conditions for data points 4-7.

tabulated pathlength, pressure, and CO_2 concentration given in Table 7 and Table 8, along with the calculated optical temperature, wall conditions, and SAR value given in Table 11 for the corresponding data point.

From Figure 31, comparable changes in peak width with changing pressure can be seen for both measured and modeled spectra. The higher load data (10) has wider peaks, larger wings and higher troughs than the lower load data (24) as is seen in the model. Interestingly, peak height trends are not affected by the change in pressure.

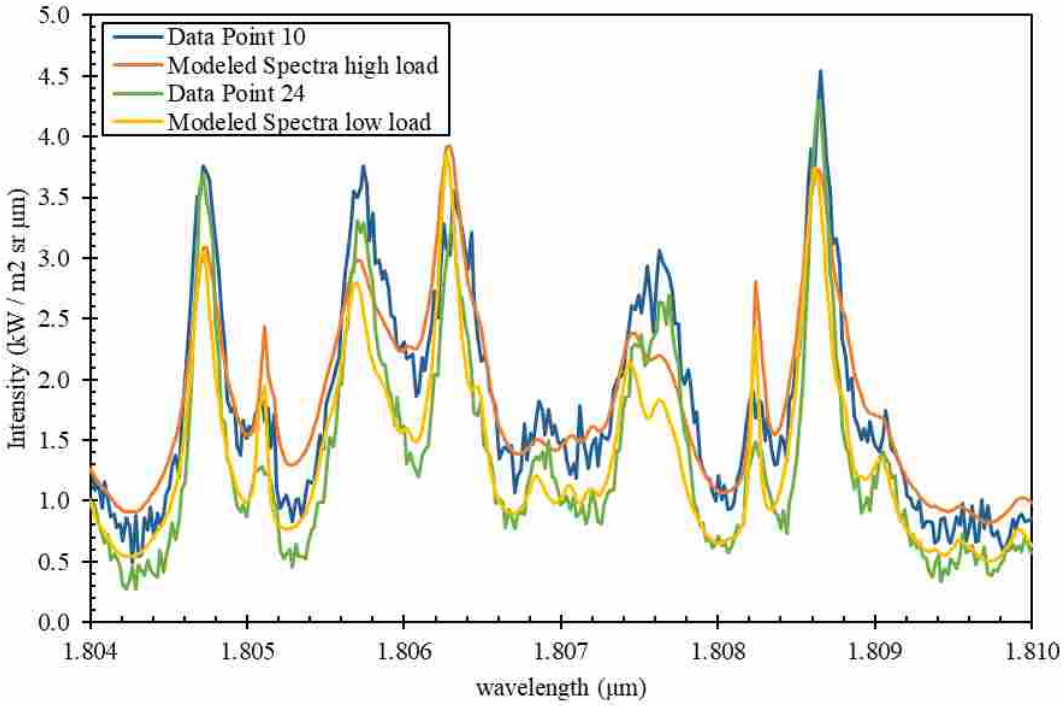

Figure 31: Measured spectra for data points 10 and 24 (high and low load, average optical temperatures of 1420 K) with modeled spectra generated for the conditions shown for each respective data point in Table 7 and Table 8 and Table 11.

Measured peaks that were higher than modeled peaks at high pressure are also higher at low pressure, and vice versa for peaks that are lower than modeled peaks. The same trends in measured to modeled peak height can also be seen when comparing Figure 31 against Figure 30.

Visual temperature uncertainty was explored by manually varying the temperature in the model before plotting the measured and modeled spectra. Figure 32 shows measured spectra plotted with modeled spectra at the calculated optical temperature, as well as modeled spectra generated using a gas temperature 100 K higher than the average optical temperature of 1438 K, specifically 1538 K. Plots of spectra in bands E and A were chosen both because of the large spectral separation between them and due to the proximity of $T_{E/A}$ to the average optical temperature. Modeled conditions match those given in Table 7 for both measured spectra. Optical conditions at 1438 K match those given in Table 11. For the 1538 K model, wall

conditions and SAR were recalculated to best fit the modeled spectra, yielding a wall temperature and emissivity of 842 K and 0.510, and an SAR of 2.19.

From Figure 32, the agreement of the average ISBR temperature can be clearly seen. While not all measured and modeled peaks are the same height, on average, modeled peaks at 1438 K are comparable heights in both bands A and E. For modeled spectra at 1538 K, the measured spectra for band E is noticeably higher than the modeled spectra, with the measured spectra in band A being noticeably lower. Even when forcing the measured and modeled integrated intensity to match for bands A-E, as is the case with the updated SAR value, the model could not be forced to match the measured data across the spectrum when the wrong temperature is assumed. This line of analysis is equivalent to the ISBR temperature ratios that were employed to obtain a temperature of 1438 K. Given the visual inconsistency in spectra at a gas temperature 100 K offset from the ISBR calculated temperature, the uncertainty in ISBR temperature was determined to be below 100 K.

5.4 Correlating Voltage Ratio with Thermocouple Temperature

In addition to using ISBR ratios of calibrated intensities to calculate gas temperature, ratios of integrated raw signal, referred to as voltage, were also evaluated. Comparable to analysis of optical temperatures, the computed ratios for high load measurements (1-18) were correlated with the average exhaust thermocouple temperature, as is shown in Figure 33. A near-linear correlation is seen between changes in integrated voltage ratio and thermocouple temperature. It is believed that this behavior is due to the small temperature range evaluated, such that voltage is nearly a linear function of intensity and intensity of gas temperature (see Figure 24 and Figure 9). Of the three ratios, E/B again exhibits the maximum standard error for

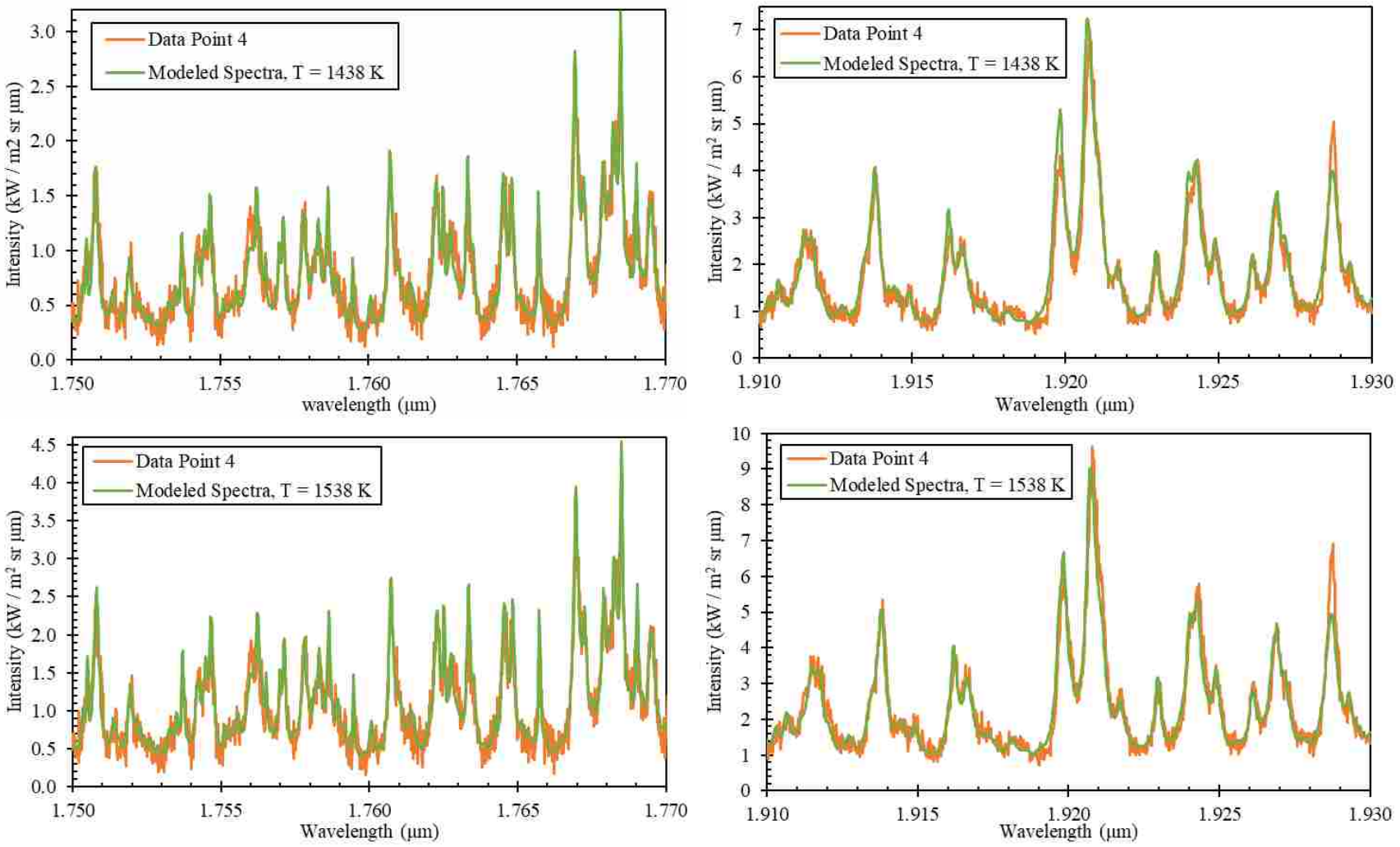

(band E) (band A)

Figure 32: Measured spectra for data point 4 (average optical temperature of 1438 K) with the top row of modeled spectra reflecting the conditions shown in Table 6 and Table 10. The bottom row of modeled spectra are at a temperature of 1538 K. Correspondingly, wall temperature, emissivity, and SAR were updated to 842 K, 0.510, and 2.19, respectively.

the line of best fit at ± 5 $K_{exhaust}$, or the ability to use voltage ratios to predict exhaust temperature at a theoretical maximum uncertainty of ± 5 K.

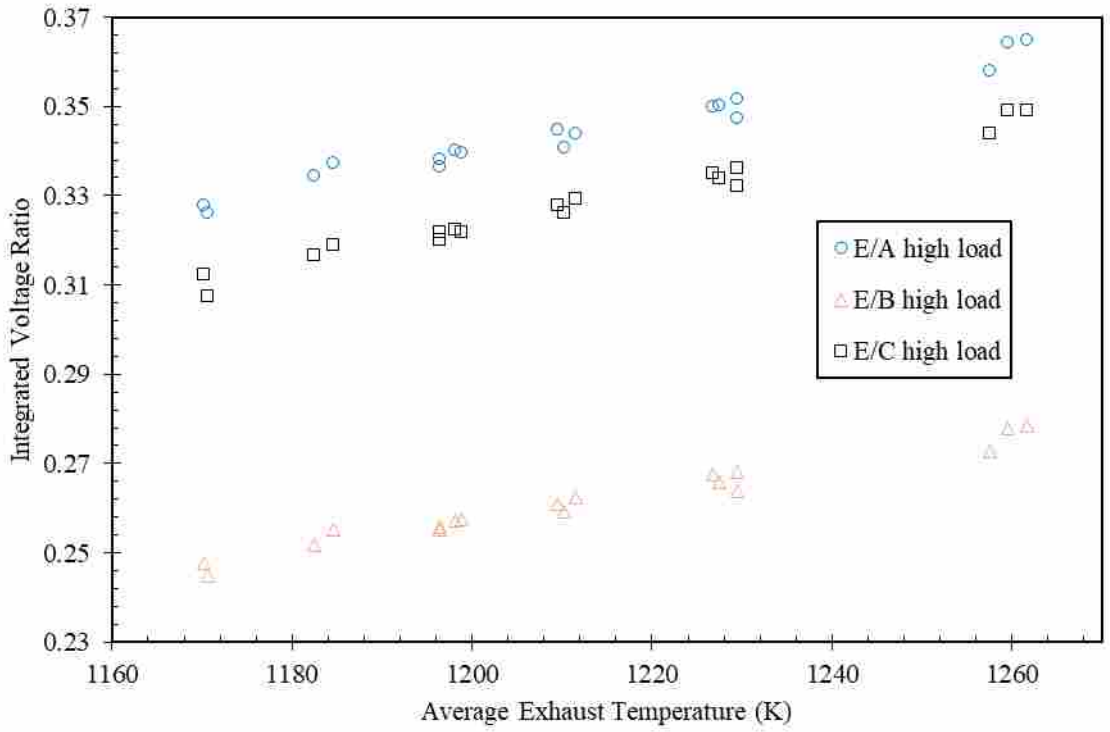

Figure 33: Integrated voltage ratios for ISBR bands as a function of average exhaust temperature for high load data points (1-18).

While voltage ratios do show a tighter correlation to exhaust temperature than ISBR temperatures, important information is lost in the raw measurement. Voltage ratios can only indicate that gas conditions have changed, giving no prediction of the gas temperature. While changes in gas temperature could be important, such as in system monitoring applications, use of voltage ratios requires a reference measurement to establish a relationship with temperature. In the case of the data shown, this reference temperature was a series of thermocouples. Though the variation is expected to be slight for reasons discussed in the development of ISBR correlations, voltage ratios would also shift with changes in pressure, pathlength, and concentration. Unlike ISBR ratios, where a new correlation can be computed reflecting this change in gas properties,

changes in measurement conditions while using voltage ratios would require new reference temperature measurements.

5.5 Sources of Error

Potential sources of error were quantified, both to validate the measurement taken and to further explore the limitation of the ISBR method. A brief discussion of each will be given.

5.5.1 Signal-to-Noise

A signal-to-noise ratio was calculated by evaluating signal fluctuations in a region without significant gas participation, namely B2, where the measured spectra would theoretically approximate a smooth Planck distribution. The B2 region measured and modeled spectra for data point 1 are shown in Figure 34. Fluctuations were found to be on the order of ±0.1 kW / m^2 sr μm. While this noise was found to be large in band B2, in band E, the measurement band with the weakest signal, the change in signal between peaks and troughs for data point 1 was as high as 3.5 kW / m^2 sr μm for large peaks, giving a signal-to-noise ratio of 35. While signals did get weaker for lower temperature and pressure data points, signal-to-noise ratios in band E remained above 23 for all ISBR data measured.

Signal-to-noise ratios previously discussed assume that all fluctuations in the spectral data are random noise inherent to the measurement. This is not entirely accurate, due to the Fourier transformation used in data processing, as was discussed in Section 3.3. Methods were explored for reducing the fluctuations in the data, specifically through zero padding interferogram and evaluating additional apodization functions. Figure 35 focusses on a very small wavelength width of 1 nm and zooms in on the magnitude of the high frequency fluctuations in the data. Three different apodization/padding schemes are shown: 1) boxcar

apodization without zero padding (the Fourier transform processing method used in this work) 2) boxcar apodization with

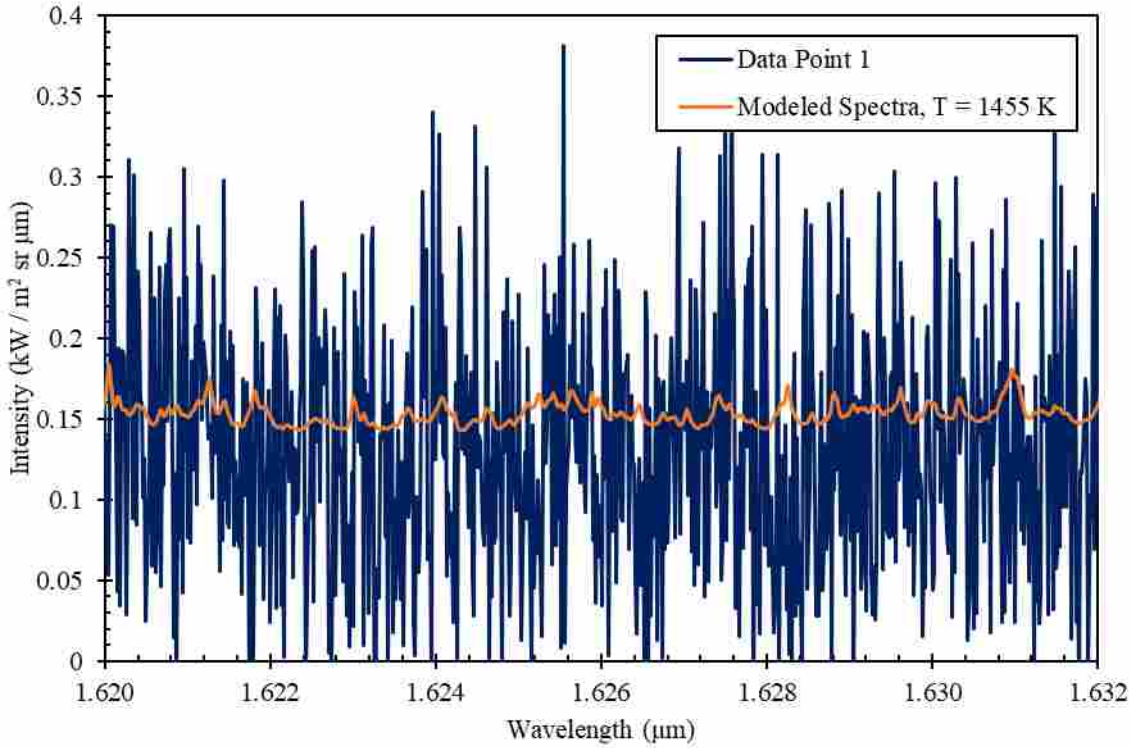

Figure 34: Measured spectra reduced by the area ratio and modeled spectra at the average optical temperature for data point 1 in ISBR band B2.

zero padding and 3) the Happ-Genzel apodization with zero padding. Outside of fluctuations on the sub 0.04 nm scale, changing the apodization, zero padding the interferogram, or a combination of both has minimal effect on the spectra. With the use of integrated spectral bands that are a minimum of 14 nm in width, variations due to apodizations or zero padding are seen to have negligible effect on the processed spectra.

Due to the difficulty in separating signal noise from Fourier transform related spectral fluctuations, equating the signal-to-noise ratio to an uncertainty in optical temperature was not attempted. Instead, the scatter of 5 to 26 K between optical measurements taken under the same conditions, as was seen in Figure 27, was used as a representation of the noise present in the

data. An uncertainty of ± 25 K, nominally 2% of 1400 K, was used as a conservative estimate for the impact of noise on optical temperature measurements.

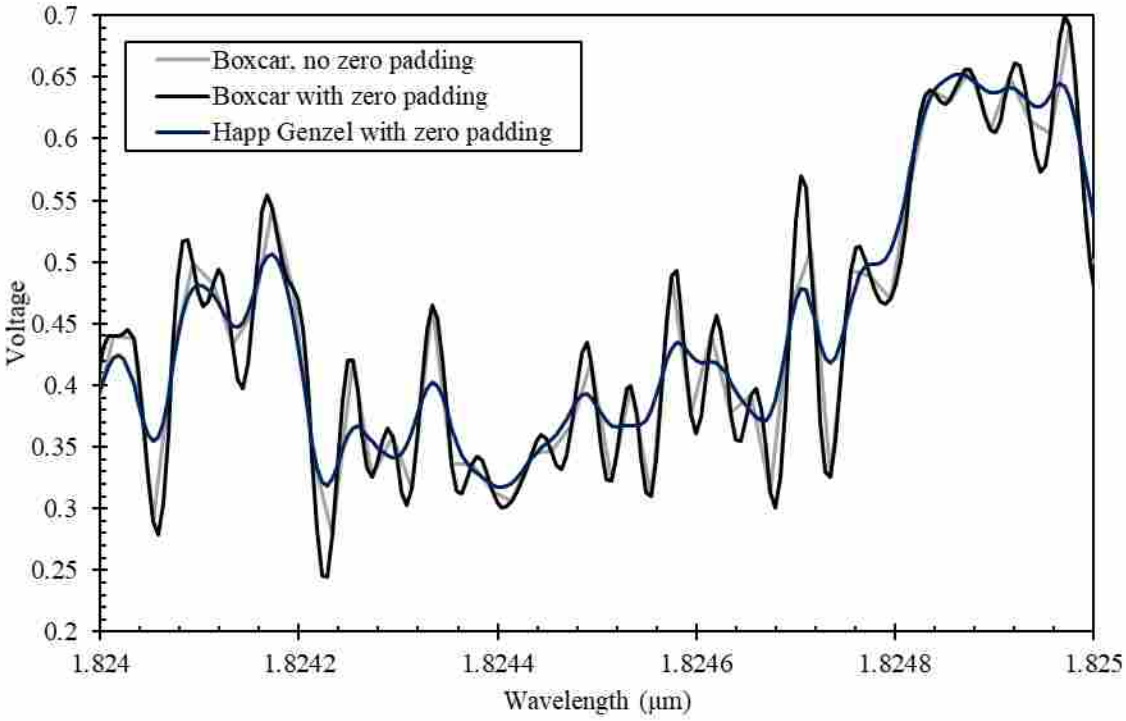

Figure 35: Various apodization functions and zero padding of unprocessed voltage measurements for data point 1 in band C.

5.5.2 Wall Temperature

Error in wall temperature and emissivity calculations would have an uneven effect on calculated gas emission and an impact of ISBR temperatures. An erroneously high wall temperature would result in background emission term with an incorrect slope, impacting high wavelengths, such as band A, differently than low wavelengths such as band E. Subtracting such an erroneous background emission term would change the ratio of E/A, changing the calculated gas temperature.

Measured spectra for data point 1 is shown in Figure 36. Wall emission, 864 K with an emissivity of 0.351, was added. Wall temperature was varied ± 50 K to evaluate the goodness of

fit of the calculated wall temperature. In spite of noise present in B1, intensity calculated at wall temperatures 50 K above and below the inferred wall temperature are clearly not good fits to the measured data. As such, the uncertainty in broadband temperature was determined to be less than ± 50 K.

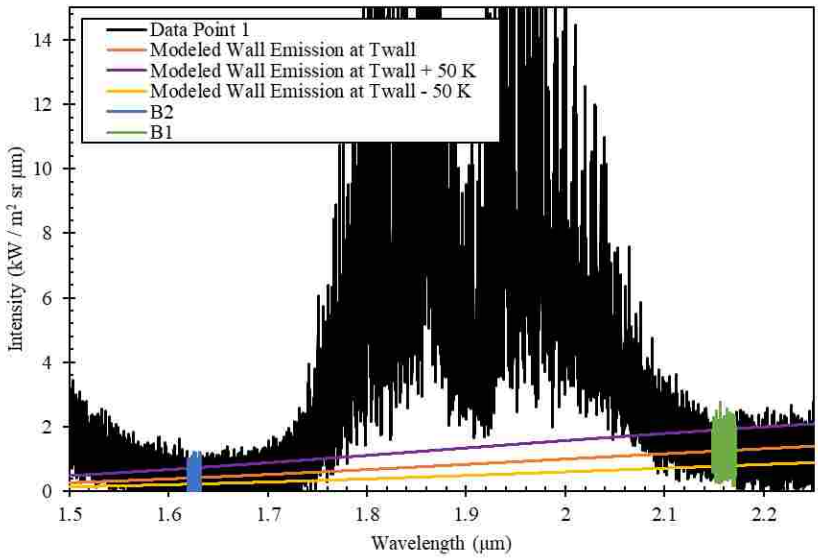

Figure 36: Measured spectral intensity from data point 1 along with optically calculated wall emission (850 K, emissivity of 0.351), and wall emission at ±50 K. B1 and B2, the ISBR regions used for calculating wall properties, are highlighted for reference.

In addition to visually agreeing with the spectra for a given test, optically measured wall temperature and emissivity can be evaluated for all tests as a function of gas temperature, as shown in Figure 37. Wall temperatures show a positive correlation with exhaust gas temperature, as would be expected from walls that are heated by the gas. Wall emissivity is fairly constant with changing gas temperature. Given the correlation with thermocouple temperature and the visual agreement shown previously, an uncertainty of ± 30 K on the wall temperature is seen as a conservative estimate.

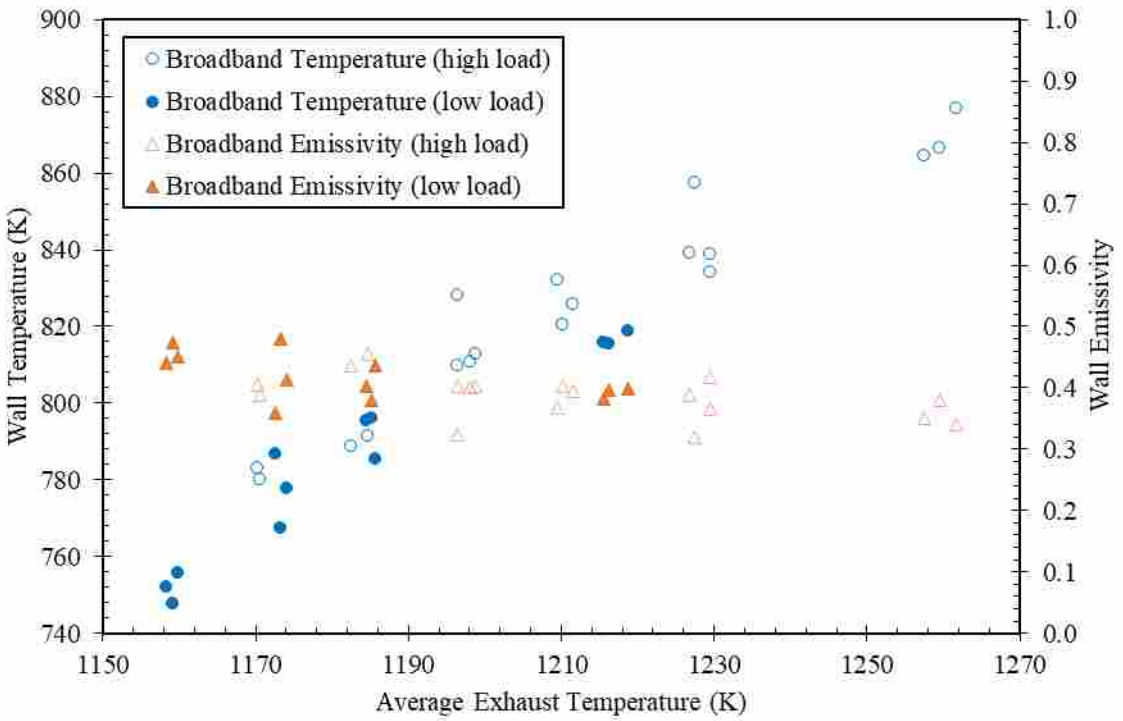

Figure 37: ISBR calculated wall temperature and emissivity as a function of average exhaust temperature.

Values for wall temperature in particular are of interest due to the impact on gas measurement ratios. ISBR temperatures were calculated for wall temperatures ± 30 K from originally calculated values. The corresponding error in gas temperature was consistently below ± 20 K. As would be expected due to their spectral separation, errors in background temperature affect $T_{E/A}$ the most. This is not the trend seen in the measured data, where $T_{E/A}$ is consistently between $T_{E/B}$ and $T_{E/C}$, but could be a contributing factor to optical temperature uncertainty.

5.5.3 Calibration at Low Intensity

As was discussed in Section 4.2, multiple calibration curve fitting equations were explored as part of this work with significant variation found between equations. Of specific

interest is the spectral behavior at low intensity, as wide troughs form a large part of each integrated intensity.

Specifically, six potential calibration curve fit equations were evaluated. Significantly larger variation was seen at low intensities, specifically in B1 and B2, than moderate or high intensities, such as in gas emission peaks in bands A through E. Figure 38 shows the variation in intensity in band B2 for each of the calibrations. Unlike the noise introduced by using different apodizations, changing the calibration equation affects the magnitude of the spectra, changing calculated wall conditions.

May 18 data was processed using each of the six calibration equations to better understand their merits. It was found that the power and exponential curve fit with an offset was not able to process low intensity data, as could be expected given behavior observed in Figure 24, and as such was removed from consideration. Calculated wall temperatures for the remaining five curve fit equations are shown in Figure 39. The polynomial equation with an offset yielded unreasonably low wall temperatures, with a mean and mode emissivity of 29,000 and 9, respectively. Emissivities calculated using the power to exponential with an offset curve (I = A*exp(B*v^C)+D in Figure 37) also varied above unity, and as such all equations with a calculated offset were removed from consideration.

Of the six equations considered, the three without an offset term performed the best at low intensity. Of these three, calculated gas temperatures varied by only ±15K between them. A more conservative value of ±20K was used to reflect uncertainty due to calibration equation selection. As was discussed in Section 4.2.3, the “Power and Exponential No Offset” from Table 6 was selected for data processing in this work.

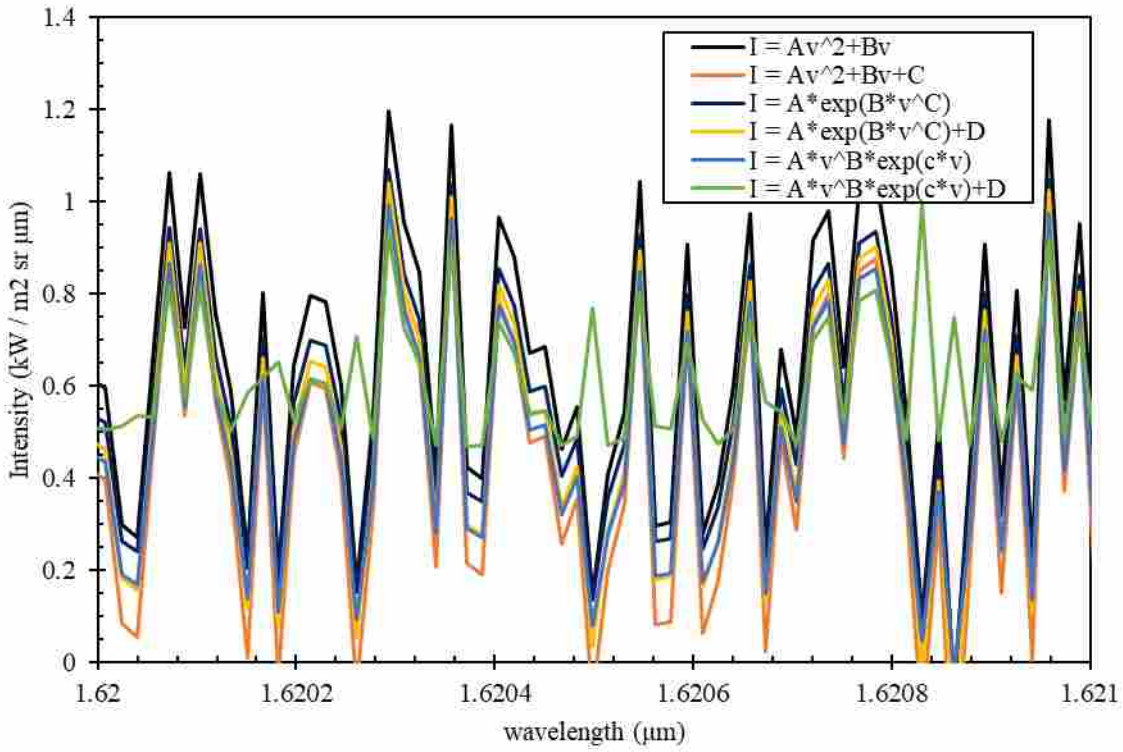

Figure 38: Measured spectra for data point 1 in band B2 corresponding to each of the six calibration equations explored as part of this work.

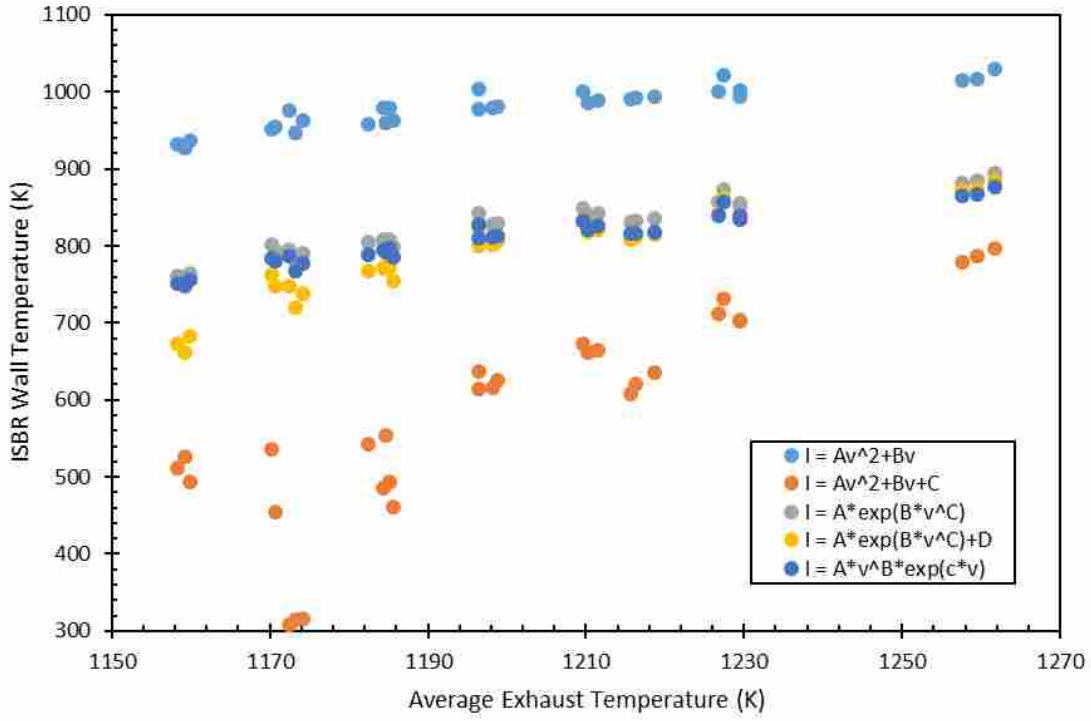

Figure 39: ISBR calculated wall temperature as a function of average exhaust temperature for five of the calibration curve fit equations considered.

5.5.4 Non-Collimated View

An additional source of error during measurements could be attributed to the non-collimated light entering the fiber. While the measurement is not a strong function of pathlength, it is possible that a wide solid angle view could allow spectra originating at different temperatures to enter the fiber. This would be especially problematic during calibration, when the probe could be viewing the hot blackbody cavity as well as the warm refractory liner of the blackbody.

A numerical model was generated highlighting the effect simultaneously viewing two surfaces at different temperatures, comparable to the hot blackbody and warm surrounding ceramic or refractory. In this instance, a fraction of the view was occupied by emission at 1000 K, representing the blackbody cavity, with the remainder at a lower temperature, representing another surface of competing emission. Signal intensity in bands E and C, approximated as 1.760 and 1.820 μm, respectively, was used to evaluate the impact.

Results of this analysis are shown in Figure 40. The highest error occurs when the colder area exterior to the blackbody cavity is different enough or cold enough to change the ratio of E/C but hot enough to contribute to the total magnitudes of bands E and C. Given that the exterior refractory did not glow during calibration, it was likely well below 800 K and therefore did not impact the ratios generated by the calibration by more than 1%. Similarly, the interior surface of the blackbody cavity, although potentially at a non-uniform temperature, likely did not vary by more than 50 K. As such, an uncertainty of ± 15 K could be attributed to temperature variations due to poor collimation and temperature variations present during calibration measurements. The impact of poorly collimated light on the defined optical pathlength for a participating medium will be discussed in Section 5.5.6.

5.5.5 Temperature Gradients

Temperature gradients in the gas stream have been shown to impact ISBR temperature measurements in non-intuitive ways [18]. Modeling analysis was performed to evaluate the potential impact of a temperature gradient on measured optical temperatures based on pressure rig conditions. The optical path of the simulated pressure rig was discretized along a grid of 11 pathlength segments, each with uniform properties. Pressure, water concentration, and total pathlength match conditions for data point 1. To isolate the impact of gas temperature gradients, wall emission was not included. Modeled gas temperature was varied between 1300 and 1500 K, representative of the 195 K maximum difference between thermocouple readings. A visual depiction of the temperature bins used is shown in Figure 41.

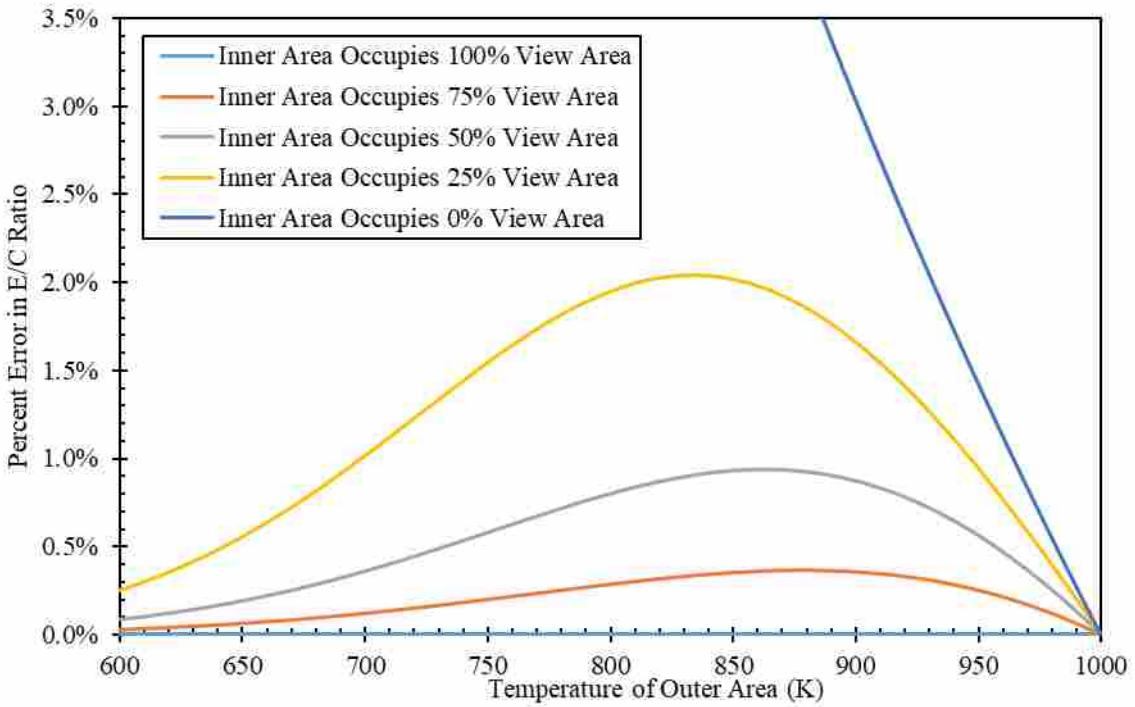

Figure 40: Modeled effect of variable view area on measured ratio E/C. Band E was approximated as 1.760 µm and band C 1.820 µm, both with blackbody emission for simplicity. Both the relative area and temperature of the outer area were varied to highlight the impact on E/C ratio.

Spectral models were developed according to Equation (**3-16** and gas temperature was calculated using the ISBR method with SAR. Because the mean temperature of the participating medium varied between each bin, the error between optical and geometrically averaged temperature will be used.

From this analysis, it was found that flows with narrow regions of high temperature yielded optical temperatures in excess of the geometric mean temperature, as shown in Figure 42. This result agrees with previous findings under similar conditions [18]. In addition to the magnitude of the temperature difference, modeled temperature gradients impacted $T_{E/B}$ and $T_{E/C}$ almost identically. Measured data do not show similar trends in optical temperatures, where measured $T_{E/A}$ values are between $T_{E/B}$ and $T_{E/C}$. As such, the impact of temperature gradients cannot be dismissed, but it is not believed to be a dominant source of error in this measurement.

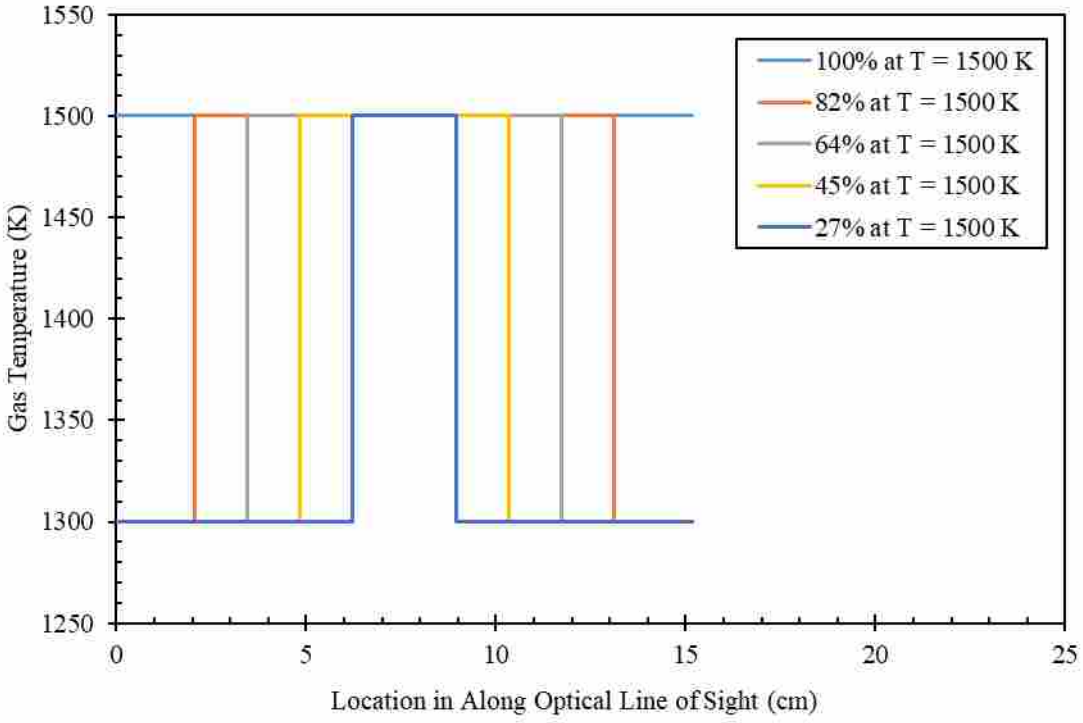

Figure 41: Temperature bins used for temperature gradient analysis. Sharp transitions between high and low temperature were used for simplicity of modeling.

An uncertainty of ± 25 K, or just under 2% of 1400 K, is given as a conservative estimate for the uncertainty due to temperature gradients.

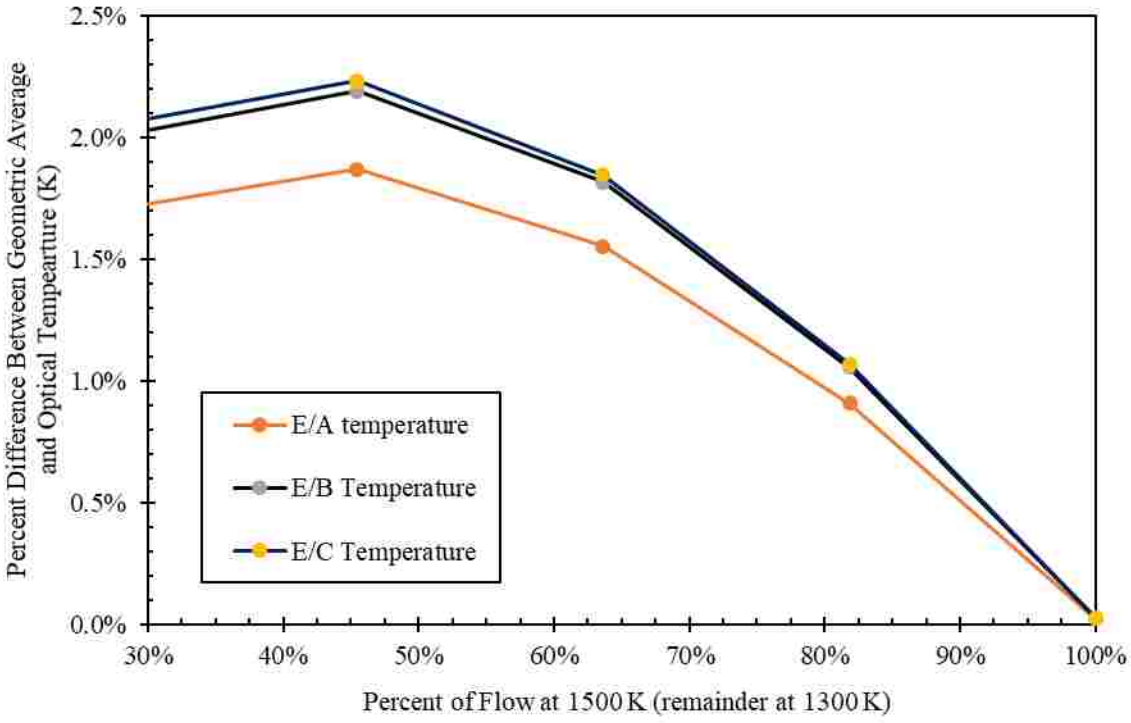

Figure 42: Results of calculating ISBR temperatures of modeled participating mediums with temperature gradients.

5.5.6 ISBR Input Gas Properties

An additional uncertainty explored was that due to input gas properties for ISBR calculations, namely pressure, water concentration, and optical pathlength. The viability of the newly developed sapphire ratios in conjunction with varying gas properties will first be explored, followed by the magnitude of the uncertainty in gas properties.

Comparable to the exploration of silica bands as a function of pressure, water concentration, and pathlength shown in Figure 4, sapphire bands were evaluated for stability with changing gas properties. The variation in ratio G/F with changing measurement conditions is shown in Figure 43. Given the focus on pressurized measurements, 1200 kPa was used as a

baseline pressure for this analysis, along with 6% water concentration and a 15 cm pathlength, conditions comparable to those expected during pressurized data collection. It was found that the new sapphire ratios were much more dependent on measurements conditions, particularly the pressure, than the previously used silica bands.

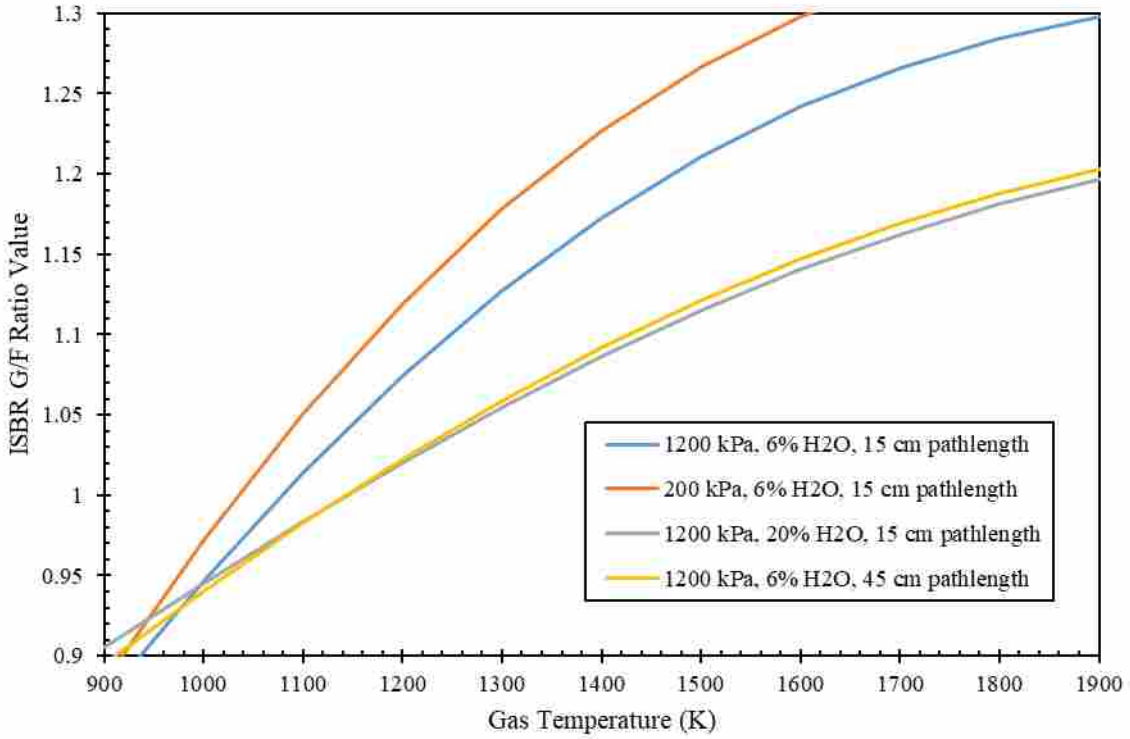

Figure 43: Sapphire band G/F as a function of other conditions

It is believed that the increased dependence of sapphire measurement bands on non-temperature conditions is due to the high peak emissivity in the sapphire region. This is comparable to a phenomenon in astrophysics referred to as the curve of growth (COG), a normalized system for quantifying the growth of a spectral line as a function of optical depth, τ or $\kappa\Delta s$ as was used in Equation (3-12) [26]. Given that κ is a function of temperature, pressure, and gas concentration, and Δs represents the optical pathlength, trends in total intensity with

changing optical depth are of great interest. Figure 44 gives a depiction of a COG line for hydrogen spectral absorption [26]. The general shape of the COG line is also applicable to water spectral emission lines. This line is formed by plotting equivalent width, comparable to a normalized total intensity, against optical depth. For optically thin absorption (small τ), the equivalent width grows linearly with optical depth, as is the case for optically thin ISBR emission measurements in the silica region. Such a trend would have minimal impact when taking the ratio of two linearly modified total intensities. When the peak of the spectral line saturates, or reaches a maximum, total intensity increases logarithmically with increasing optical depth. This can be seen to be the case for some peaks in the sapphire bands, where the emissivity near 2.5 μm approaches unity. From Figure 43, it appears that the transition between linear and logarithmic spectral line growth cannot be minimized through the use of ratios.

To further evaluate the suitability of all ratios, models were generated to compute the error in calculated ISBR optical temperature for a ±10% change in gas properties. Reference conditions of 1400 K, 1200 kPa, 6% water concentration, and 15 cm pathlength were used. Each model parameter, other than gas temperature, was varied ±10% individually and collectively. ISBR temperatures were calculated using the intensity ratios at the varied conditions as though the measurement volume were at the reference conditions stated. The error in optical temperature for each ratio is shown in Table 13.

As can be seen in Table 13, the sapphire measurement bands are not as stable with changing measurement conditions as the silica bands. While the uncertainty in pressure, concentration, and pathlength is believed to be less than ±10% during pressurized measurements, the potential for measuring non-uniform flows suggests that the sapphire band ratios should be

avoided. As such, sapphire ratios were not used for calculating temperature as part of this work in favor of the silica ratios of E/A, E/B, and E/C.

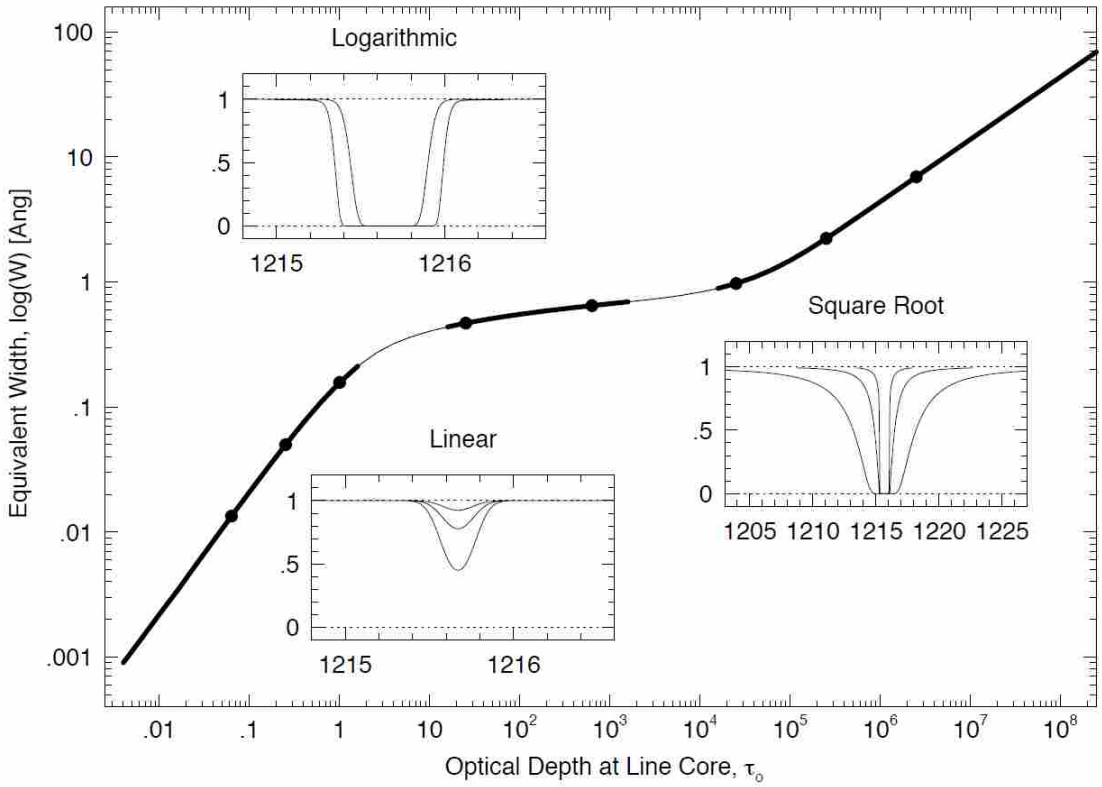

Figure 44: The curve of growth (COG) showing equivalent width, a value comparable to total peak intensity, as a function of the optical depth at the line core, τ_0, for the Ly α hydrogen absorption line. The three regimes, "linear", "logarithmic", and "square root" are shown by the thick curves, respectively, as τ_0 increases. Absorption profiles are shown for each regime and their locations on the COG are marked with filled points. Note the expanded wavelength scale for the profiles on the square root part of the COG. This is due to large damping wings. Figure courtesy of Chris Churchill [26].

As for the uncertainty of E/A, E/B, and E/C, the total uncertainty listed in Table 13 does not account for concentration gradients in addition to the uncertainty of the average value. Assuming comparable behavior in concentration gradients as was found for temperature, a resultant gas temperature uncertainty of ± 50 K, corresponding to 3.5% of 1400 K, was given to

represent gas temperature uncertainty due to uncertainty in pressure, water concentration, and pathlength.

Table 13: Error inherent to uncertainty in ISBR measurement conditions. A reference condition of 1400 K, 1200 kPa, 6% water concentration, and 15 cm pathlength was used.

	Error in $T_{optical}$ with ±10% change in pressure (K)	**Error in $T_{optical}$ with ±10% change in water concentration (K)**	**Error in $T_{optical}$ with ±10% change in pathlength (K)**	**Error in $T_{optical}$ with ±10% change in P, y_{H2O}, and PL (K)**
E/A	4	3	4	11
E/B	10	7	9	29
E/C	8	6	7	23
J/F	24	23	33	89
J/G	43	38	54	147
J/H	40	45	76	175
H/F	19	16	18	59
G/F	217	146	209	501

5.5.7 Discrepancies with HITEMP Model

Comparing measured and modeled spectra reveals significant agreement at all ISBR wavelengths, specifically agreement in peak location, width, and average height. Consistent and seemingly random disagreement is seen in the height of each peak. This behavior is highlight in Figure 45, where four measured data points consistently err higher or lower than the modeled peaks. Given the two large peaks at 1.8505 and 1.8570 μm where the modeled peak height is higher and then lower, respectively, than the measured peaks, overall peak size does not appear to be a factor in their agreement. Similar behavior can be seen in other peaks in Figure 45, Figure 30, and Figure 32, representing bands A, B, C, and E for data points 4-7, and Figure 31 representing band C for data points 10 and 24. Comparable behavior exists for all measurements.

Due to the dynamic nature of the flow volume (velocity ~ 35 m/s) and the non-uniform composition in both temperature and species, there is no clear conclusion that can be drawn

regarding the correctness of either the measured or modeled spectra. It would appear, however, that a discrepancy does exist. Based on results discussed, the difference between measured and modeled spectra does not appear to significantly affect the ability to match

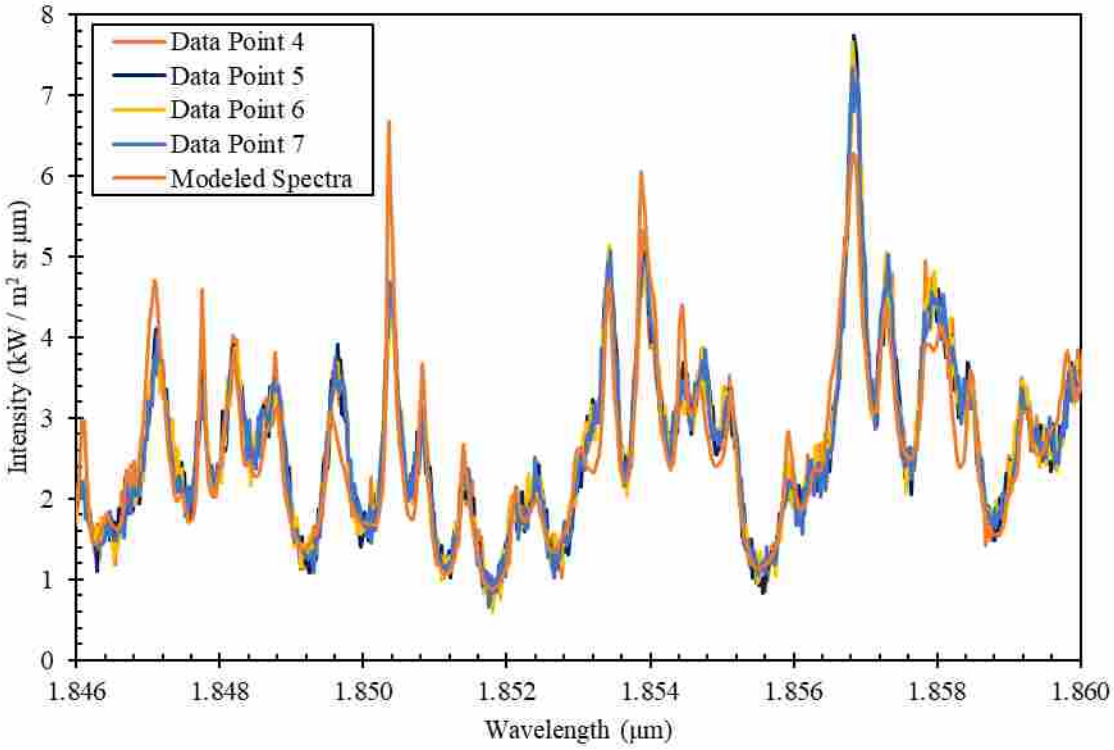

Figure 45: Measured spectra for data points 4-7 (high load, T_{PZ} = 1821 K) with modeled spectra generated for a 15 cm pathlength of 2.98% CO2 and 5.96% H2O at 1183 kPa and 1438 K with a far wall at 842 K and a wall emissivity of 0.373. An SAR ratio of 3.0 was used to scale all measured spectra. Values used reflect average conditions for data points 4-7.

the two using ISBR ratios. This could be due to the use of integrated areas and their ability to average out differences in individual peak height. As such, it is difficult to attribute a numerical error in calculated temperature to this spectral difference and therefore, no quantitative error has been assigned. No attempt will be made to quantify this uncertainty.

6 FUTURE WORK WITH NON-SPECTRAL DETECTORS

As was discussed in Section 3.4, non-spectral InGaAs detectors are being evaluated for replacing the FTIR in ISBR data collection. At the writing of this document, the detectors have been manufactured but not tested. Work is being performed to measure the output of the detectors. Given that this output is on the order of 1.0 μA, a circuit has been designed to amplify and convert the signal to a voltage that can be read by a microprocessor. The circuit diagram is shown in Figure 46, consisting of a voltage inverting op amp that converts current to negative voltage, a voltage buffering op amp to isolate the InGaAs detector from the rest of the circuit, and a voltage inverting op amp that returns the voltage to a positive value. This circuit has been verified using a single InGaAs detector.

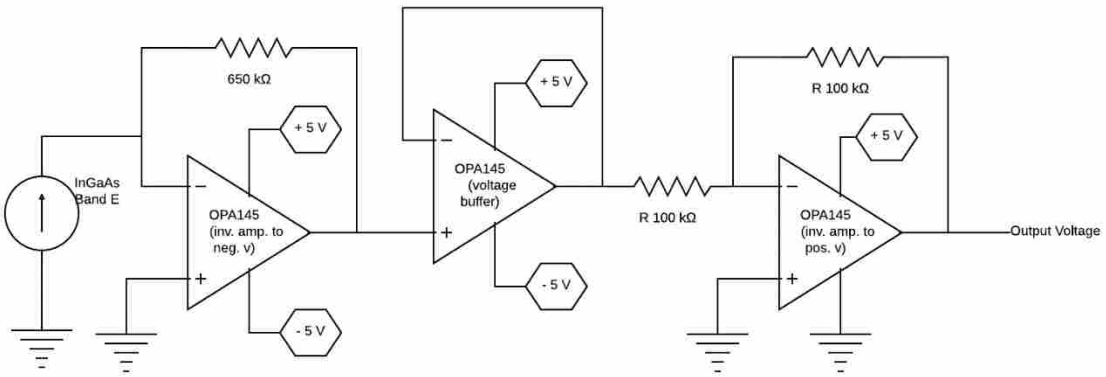

Figure 46: A proposed circuit for converting the output current from an InGaAs detector, approximated in the diagram as an ideal current source, to an amplified voltage to be read by a microprocessor.

A diagram of the data acquisition system for the InGaAs detectors is shown in Figure 47. The Cosel NAC-06-472 120 V_{AC} filter and PBW30F-5 switching power supply with a 5 V_{DC}, 30 W max output will be used as power supply components, with the Teensy 3.6, with 13-bit analog voltage resolution and 180 MHz processing speed, as the microcontroller. Both are represented in Figure 47.

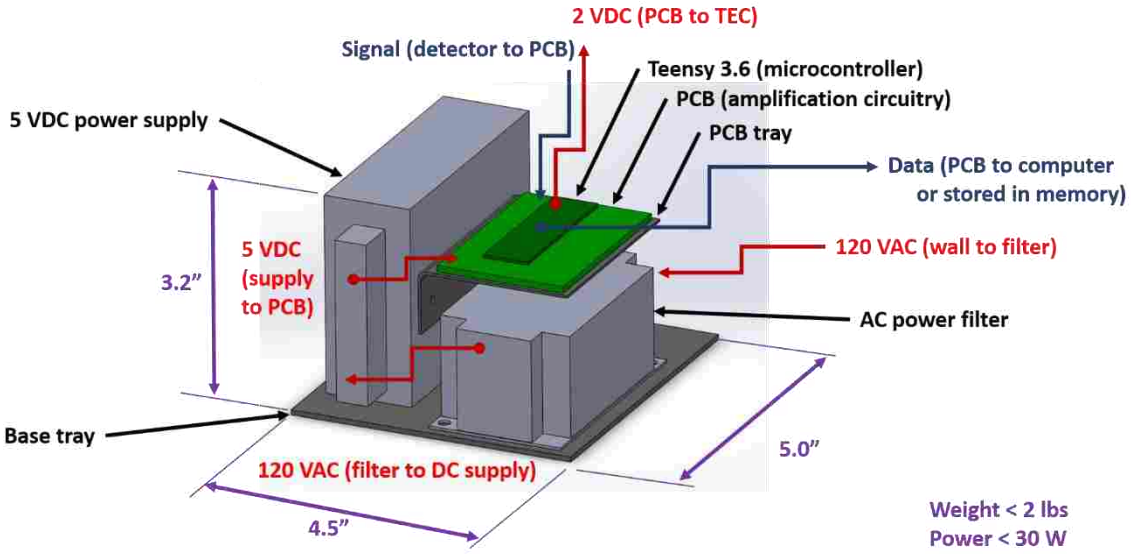

Figure 47: Diagram of a proposed InGaAs detector acquisition system including a power filter and AC/DC converter, a circuit board to convert detector output current to a voltage, and a microprocessor to measure the voltage signal.

7 SUMMARY AND CONCLUSIONS

The ISBR method was applied to a pressurized environment as part of a larger effort to measure the gas temperature of a turbine engine. Correlations between integrated intensity ratios and gas temperature were generated at pressure for previously used silica and newly measured sapphire spectral bands. Silica measured bands were found to behave comparably at pressure as during previous testing at atmospheric conditions. The newly measured sapphire bands were found to be dependent on non-temperature gas conditions such as pressure, water concentration and pathlength, and were therefore not used for ISBR analysis. An optical probe was designed for pressurized measurements that did not use water cooling or purge gas.

Measurements were taken using an FTIR in the Solar Turbines pressure rig. Thermocouple measurements were taken concurrently and found to have a random uncertainty of ± 50 K and a bias of -175 K due to radiative losses. The following observations were made regarding the optical measurements taken:

- Optical temperatures at both high and low load showed a linear relationship with thermocouple measurements. The slope between optical and thermocouple measurements was found to be very near one-to-one at 1.03±0.14 and 1.10±0.10 $K_{optical}$ / $K_{exhaust}$, for high and low loads, respectively.
- Optical measurements were 210±19 and 232±19 K higher than the corresponding thermocouple measurements, for high and low load measurements, respectively.

- Optical temperatures were consistently between modeled primary zone (before mixing with secondary air) and secondary zone (after mixing with secondary air) temperatures. Thermocouple measurements corrected for radiative losses were also significantly higher than modeled secondary zone temperatures.
- Repeated measurements at the same operating condition produced small variations in average thermocouple temperature on the order of ± 3 K but variations on the order of ± 15 K for the optical measurements.
- Sources of error in optical calculations were identified, with the main contributor found to be uncertainty in non-temperature ISBR property inputs, such as water concentration and pathlength. Temperature gradients and signal noise were also likely significant sources of noise.
- The total uncertainty in optical measurements was determined to be ± 70 K. In light of the offset of 44 K between optical and radiation corrected thermocouple measurements, pressurized ISBR measurements were shown to agree with thermocouple readings.
- Both optical and corrected thermocouple measurements were significantly higher than the theoretical maximum secondary zone temperatures, indicating delayed mixing of secondary air or other measurement uncertainties not explored, such as measured fuel or air mass flow rates. Further analysis is required to fully validate the magnitude of ISBR temperature measurements at pressure.

Additional analysis was performed by comparing the measured spectra against models generated from the HITEMP database [21]. Observations include:

- All modeled peaks are present in the measured data at the same wavelengths. Peak heights were less consistent than peak locations, with some measured peaks having larger and smaller amplitudes than their modeled counterparts.
- Measured spectra at the same test condition showed minimal variation. Measured peaks at a given wavelength were consistently higher, lower, or the same height as the corresponding modeled peak.
- Collisional broadening due to increased pressure can be clearly seen in the measured spectra and agrees with modeled broadening.
- Modeled spectra at temperatures 100 K different than the ISBR calculated temperature visibly do not agree with the measured spectra.

In addition to correlating ISBR temperatures with thermocouple temperature measurements, integrated bands of raw voltage were compared to thermocouple readings with good agreement. This method could be in a system monitoring application, where the focus is on identifying when conditions have changed. Correlating voltage to thermocouple temperature does not give any indication as to the gas temperature at the measurement location, the cause of the change in voltage ratio, and requires the presence of a thermocouple for calibration.

An optical setup using four InGaAs detectors and spectral filters was also outlined. This system will eliminate the need for an FTIR spectrometer, greatly reducing data acquisition time and measurement complexity at a cost of spectral resolution. Additional development is required before detectors can be implemented for testing.

REFERENCES

[1] M. P. Boyce, "Gas Turbine Engineering Handbook," Burlington, MA, Gulf Professional Publishing, 2006, pp. 5, 130-131, 694-696.

[2] T. Giampaolo, "Gas Turbine Handbook: Principles and Practice," Lilburn, GA, Fairmont Press, 2009, p. 117.

[3] D. J. Ellis, V. P. Solovjov and D. R. Tree, "Temperature Measurements Using Infrared Spectral Band Emissions from H2O," *Journal of Energy Resources,* vol. vol. 138, 2016.

[4] J. R. Tobiasson, "Determining H2O Vapor Temperature and Concentration in Particle-Free and Particle Laden Combustion Flows Using Spectral Line Emission Measurements," *Master Thesis, Mech. Eng., BYU, Utah, USA,* 2016.

[5] Shannon, K S; Butler, B W;, "A Review of the Error Associated with Thermocouple Temperature Measurement in Fire Environments," in *Proceedings of the 2nd Fire Ecology Congress*, Orlando, Florida, 2003.

[6] D. A. Barberree, "The Next Generation of Thermocouples for the Turbine Engine Industry," in *ISA 48th Annual International Instrumentation Symposium*, San Diego, California, 2002.

[7] C. R. Shaddix, "Correcting thermocouple measurements for radiation loss: A critical review," in *33rd National Heat Transfer Conference*, Albuquerque, New Mexico, 1999.

[8] L. C. Martin and R. Holanda, "Applications of thin-film thermocouples for surface temperature measurement," in *NASA/SPIE Conference on Spin-Off Technologies from NASA for Commercial Sensors and Scientific Applications*, San Diego, California, 1994.

[9] I. M. Tougas, M. Amani and O. J. Gregory, "Metallic and Ceramic Thin Film Thermocouples for Gas Turbine Engines," *Sensors,* vol. 13, pp. 15324-15347, 2013.

[10] R. L. Farrow, P. L. Mattern and L. A. Rahn, "Comparison between CARS and corrected thermocouple temperature measurements in a diffusion flame," *Applied Optics,* vol. 21, no. 17, pp. 3119-3125, 1982.

[11] X. Zhau, L. Xiang, J. B. Jeffries and R. K. Hanson, "Development of a sensor for temperature and water concentration in combustion gases using a single tunable diode laser," *Measurement Science and Technology,* vol. 14, pp. 1459-1468, 2003.

[12] C. S. Goldenstein, R. M. Spearrin, J. B. Jeffries and R. K. Hanson, "Infrared laser-absorption sensing for combustion gases," *Progress in Energy and Combustion Science,* vol. 60, pp. 132-176, 2017.

[13] G. B. Rieker, F. R. Giorgetta, W. C. Swann, J. Kofler, A. M. Zolot, L. C. Sinclair, E. Baumann, C. Cromer, G. Petron, C. Sweeney, P. P. Tans, I. Coddington and N. R. Newbury, "Frequency-comb-based remote sensing of greenhouse gases over kilometer air paths," *Optica,* vol. 1, no. 5, pp. 290-298, 2014.

[14] C. Kerr and P. Ivey, "An overview of the measurement errors associated with gas turbine aeroengine pyrometer systems," *Measurement Science and Technology,* vol. 13, pp. 873-881, 2002.

[15] S. Clausen, "Local measurement of gas temperature with an infrared fibre-optic probe," *Measurement Science and Technology,* vol. 7, 1996.

[16] W. M. Glasheen, C. A. DeMilo and Y. R. Sivathanu, "Turbine Inlet Gas Temperature Sensor," in *International Gas Turbine & Aeroengine Congress and Exhibition*, Indianapolis, Indiana, 1999.

[17] S. Nakaya, T. Funahashi, Y. Asakami, I. Fujio, S. Takahashi and M. Tsue, "Thermometry of combustion gas measuring two-band near-infrared emissions less than 1.1 μm from water molecules," *Experimental Thermal and Fluid Science,* vol. 94, pp. 1-8, 2018.

[18] J. R. Tobiasson, S. C. Egbert, B. R. Adams and D. R. Tree, "An optical method for the measurement of combustion gas temperature in particle laden flows," *Environmental and Thermal Fluid Science,* vol. 98, pp. 704-711, 2018.

[19] M. F. Modest, Radiative Heat Transfer, 3rd ed., New York: Academic Press, 2013.

[20] T. L. Bergman, A. S. Lavine, F. P. Incropera and D. P. DeWitt, Fundamentals of Heat and Mass Transfer, 8th ed., New York: Wiley, 2002.

[21] J. T. Pearson, B. W. Webb, V. P. Solovjov and J. Ma, "Efficient Representation of the absoprtion line blackbody distribution function for H2O, CO2, and CO at variable temperature, mole fraction, and total pressure," *Journal of Quantitative Spectroscopy & Radiative Transfer,* vol. vol. 138, 2014.

[22] M. S. Glazman, Y. A. Landa, E. Y. Litovskii and N. A. Puchkelvich, "Spectral emissivity of refractories (review article)," *Refractories and Industrial Ceramics,* vol. 5, pp. 46-51, 1989.

[23] P. R. Griffiths and J. A. de Haseth, Fourier Transform Infrared Spectroscopy, New York: Wiley, 2007.

[24] S. R. Turns, An Introduction to Combustion: Concepts and Applications, 3rd ed., New York: McGraw Hill, 2012.

[25] J. R. Phillips, "ZunZun," [Online]. Available: http://zunzun.com/. [Accessed 4 July 2019].

[26] C. Churchill, "Chapter 16: Absoprtion Features," in *ASTR 605 Interstellar Medium Lecture Notes*, Las Cruces, New Mexico, 2009, pp. 365-376.

[27] N. Goldstein, C. A. Arana, F. Bien, J. Lee, J. Gruninger, T. Anderson and J. Glasheen, "Innovative Minimally Intrusive Sensor Technology Development for Versatile Affordable Advanced Turbine Engine Combustors," *Proceedings of the ASME Turbo Expo,* pp. 281-288, 2002.

APPENDIX A: DATA PROCESSING

Data processing for this work was performed using a MATLAB script. The bulk of the calculations branched off of a script titled MasterScript. Other operations, including generating correlations between modeled and measured integrated gas temperature ratios, calculating gas emission coefficients, etc. will also described.

A.1 Main Code

The main body of code used in this work can be divided into four subroutines with one governing script. The governing script, MasterScript, contains the file path locations for measurements and spectral data files, wavenumber bounds, and calibration temperature ranges. The MasterFilter routine filters out any absorption encountered during blackbody calibration. MasterCalibration generates the calibrations, using the measured blackbody intensities, to convert measured voltage to intensity. MasterProcessData operates on the combustion gas measurements to determine the background, gas temperature, and water concentration of each measurement. MasterProcessData calls the subroutine MasterKappa, which will be discussed in Section A.2 Correlation Generating Code

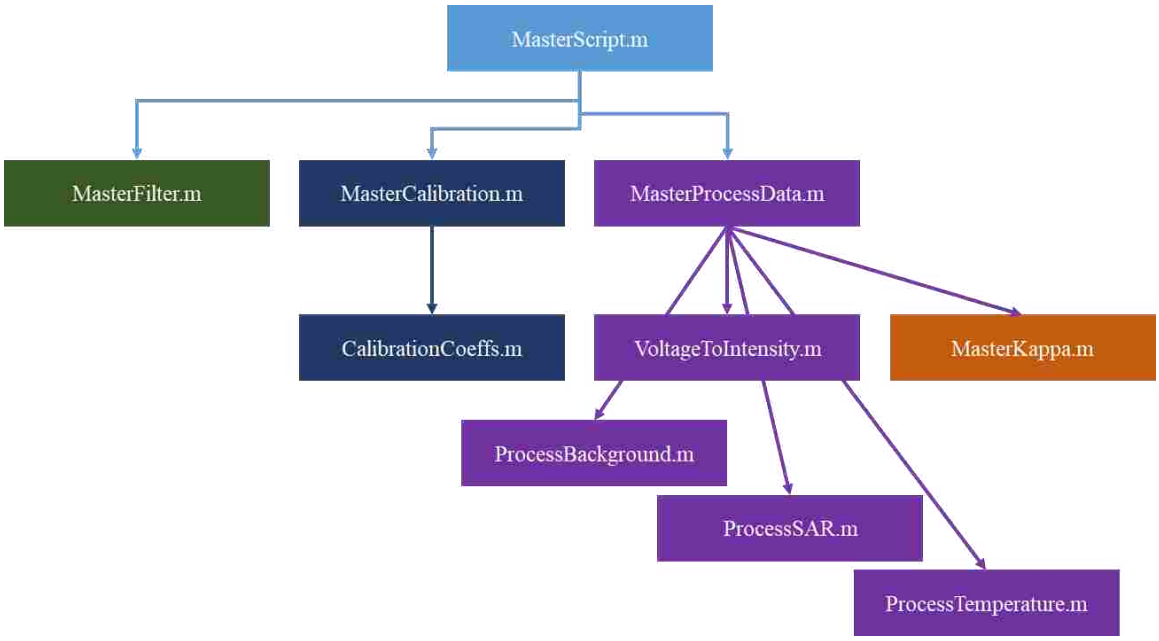

Figure A-1: MasterScript flow chart

A.1.1 MasterScript

```
%% Setup
close all
clear variables
clc

%% System Calibration

calfilepath = 'D:\scott backup April 26 2019\Solar\high pressure
testing May 2018\Calibration 2 - may 16\';
calfilename = '16May2018SolarCalibration'; %code assumes
"...0001.csv" tag on end of file
filterfilename = '16May2018SolarCalibrationFiltered';
kappafilepath = 'D:\Cabs Data\';

starttemp = 600; % max BB calibration temp
endtemp = 1300; % min BB calibration temp
tempstep = 100; % delta temperature

leftStart = 2000; %4600-5900 range for T with BG
rightEnd = 8000;  %3750-7800 good filter range silica
                  %2000-8000 good filter range sapphire
```

```
% MasterFilter(calfilepath, calfilename, filterfilename,
kappafilepath,...
%   starttemp, endtemp, tempstep, leftStart, rightEnd);

leftStart = 3000; %4600-5900 range for T with BG
rightEnd = 8000;  %4500-7500 good calibration range silica
                  %3000-7500 good calibration range sapphire

calibrationType = 'PowerAndExponential' ; % 'Polynomial'
'PolynomialOffset' 'PowerAndExponential'
%       'PowerAndExponentialOffset' 'Power2Exponential'
'Power2ExponentialOffset'

MasterCalibration(calfilepath, filterfilename, calibrationType,
starttemp, endtemp, tempstep, leftStart, rightEnd)

%% Data Processing

measfilepath = 'D:\scott backup April 26 2019\Solar\high
pressure testing May 2018\measured data - may 18\';
date = '18May2018Solar';
measfilename = strcat(date,'Test');
opticalpathfilename = strcat(date,'-Path');
suctionpyrofilename = strcat(date,'-SuctionPyro');

correlationfilepath = 'D:\scott backup April 26
2019\CalibrationIntensities';

broadbandType = 'emitting non-reflecting wall'; % 'emitting non-
reflecting wall' 'particles no wall' 'no broadband removal'
H2OcalculationType = 'with broadband'; % 'with broadband' ,
'without broadband'
fuelType = 'methane'; % 'methane' 'fine wood' 'med wood'
useAreaRatios = 'yes'; % 'yes' 'no'

startdatafile = 4;
stopdatafile = 7;
stepdatafile = 1;

MasterProcessData(kappafilepath, calfilepath, measfilepath,
measfilename, opticalpathfilename,...
    calibrationType, startdatafile, stopdatafile,
stepdatafile,...
    leftStart, rightEnd, broadbandType, useAreaRatios,
correlationfilepath, fuelType)
```

```
% MasterSpectralData(kappafilepath, measfilepath, measfilename,
startdatafile, ...
%     stopdatafile, stepdatafile, calibrationType)

%load train; sound(y,Fs)


%% ----------------Documentation-------------------
%{

% For the 04282016 calibration (PFFW, IFFW)

calfilepath = 'C:\Users\Scott\Documents\Working Files\All BFR
Combustion\extended spectrum\April Calibration\';
calfilename = '04282016Callibration'; %code assumes
"...0001.csv" tag on end of file
filterfilename = '04282016CalibrationFiltered';
datafilepath = 'F:\';

starttemp = 600; %max BB calibration temp
endtemp = 1100; %min BB calibration temp
tempstep = 50; %delta temperature

% For the 02172016 calibration (PFNG, IFNG, PFMW)

calfilepath = 'C:\Users\Scott\Documents\Working Files\All BFR
Combustion\extended spectrum\February Calibration\';
calfilename = '02172016Callibration'; %code assumes
"...0001.csv" tag on end of file
filterfilename = '02172016CalibrationFiltered';
datafilepath = 'F:\';

starttemp = 1100; %max BB calibration temp
endtemp = 600; %min BB calibration temp
tempstep = -50; %delta temperature

%}

%{

calfilepath = 'C:\Users\Scott\Documents\Working Files\Solar\high
pressure testing May 2018\calibration 1 - may 15\';
calfilename = '15May2018SolarCalibration'; %code assumes
"...0001.csv" tag on end of file
filterfilename = '15May2018SolarCalibrationFiltered';
kappafilepath = 'E:\';
```

```
starttemp = 1000; % max BB calibration temp
endtemp = 1400; % min BB calibration temp
tempstep = 100; % delta temperature


calfilepath = 'C:\Users\Scott\Documents\Working Files\Solar\high
pressure testing May 2018\Calibration 2 - may 16\';
calfilename = '16May2018SolarCalibration'; %code assumes
"...0001.csv" tag on end of file
filterfilename = '16May2018SolarCalibrationFiltered';
kappafilepath = 'E:\';

starttemp = 600; % max BB calibration temp
endtemp = 1300; % min BB calibration temp
tempstep = 100; % delta temperature


calfilepath = 'C:\Users\Scott\Documents\Working Files\Solar\high
pressure testing May 2018\calibration 3 - may 17 (bare)\';
calfilename = '17May2018SolarCalibration'; %code assumes
"...0001.csv" tag on end of file
filterfilename = '17May2018SolarCalibrationFiltered';
kappafilepath = 'E:\';

starttemp = 600; % max BB calibration temp
endtemp = 1100; % min BB calibration temp
tempstep = 50; % delta temperature

%}
```

A.1.2 MasterFilter

```
function [] = MasterFilter(calfilepath, calfilename,
filterfilename, kappafilepath,...
    starttemp, endtemp, tempstep, leftStart, rightEnd)

%% attempt at selective filtering based on absorption cross
section. Work in progress

close all

%load Cabs coefficients, extract the data from a structure
H2Oraw =
load(strcat(kappafilepath,'relevantH2OCabsDatabaseFiles\Cabs h2o
300K Y1 P1'));
fieldName = fields(H2Oraw);
```

```
H2Odata = H2Oraw.(fieldName{1});

CO2raw =
load(strcat(kappafilepath,'relevantCO2CabsDatabaseFiles\Cabs co2
300K Y0 P1'));
fieldName = fields(CO2raw);
CO2data = CO2raw.(fieldName{1});

[~, leftBand] = min(abs(H2Odata(:,1) - leftStart));
[~, rightBand] = min(abs(H2Odata(:,1) - rightEnd));

%estimate H2O and CO2 concentration
ppmH2O = 7223.2; % witih old guesses
ppmCO2 = 400;

H2Oabsorb = H2Odata(leftBand:rightBand,2) * ppmH2O;
CO2absorb = CO2data(leftBand:rightBand,2) * ppmCO2;
etaAbsorb = H2Odata(leftBand:rightBand,1);

allAbsorb = H2Oabsorb + CO2absorb;

% plot(nuAbsorb,allAbsorb)

clear H2Oraw CO2raw H2Odata CO2data fieldname H2Oabsorb
CO2absorb

%establish minimum value
[~, cutoffSplit1] = min(abs(etaAbsorb - 4500));
[~, cutoffSplit2] = min(abs(etaAbsorb - 6500));

cutoff(1:cutoffSplit1,1) = 1E-17; %units unknown, selected by
looking at plot and filtered data
cutoff(cutoffSplit1:cutoffSplit2,1) = 1E-18; %best performance
found by applying multiple
cutoff(cutoffSplit2:length(allAbsorb),1) = 1E-19;

%create arrays for finding absorption rising and falling past
cutoff
up = allAbsorb - cutoff;
up(up<0) = 0;
down = cutoff - allAbsorb;
down(down<0) = 0;

k = 1; %index in spectral array
j = 0; %index in absorption bands array
kFinal = length (up);
```

```
while k < kFinal && any(up) == 1
    j = j+1;

    absorbIndex(j,1) = find(up,1); %find section where cutoff
starts
    k = absorbIndex(j,1); %shift spectral array index to new
position

    down(1:k) = 0; %remove previously identified peaks

    absorbIndex(j,2) = find(down,1); %find section where cutoff
ends
    k = absorbIndex(j,2); %shift spectral array index to new
position

    up(1:k) = 0; %remove previously identified peaks

    absorbBands(j,:) =
[etaAbsorb(absorbIndex(j,1)),etaAbsorb(absorbIndex(j,2))];
end

clear up down allAbsorb nuAbsorb

i = 0; %initialize counter variable
for T = starttemp:tempstep:endtemp
    tic
    i = i+1;

    %     if i == 2 || i == 5 || i == 10 || i == 13
    %         i = i +1;
    %     end               %for february 2016 calibration

    if i<10 %matches file format "...0001.csv" from OMNIC
default
        numstr = strcat('000',num2str(i));
    elseif i<100
        numstr = strcat('00',num2str(i));
    elseif i<1000
        numstr = strcat('0',num2str(i));
    else
        numstr = num2str(i);
    end

    tempstr = num2str(T); %temperature value as a string

    % Load data
```

```
    data =
csvread(strcat(calfilepath,calfilename,numstr,'.csv'));

    % Extract variables, prepare for filtering
    V = data(:,2); % Voltage
    eta = data(:,1); % Wave number
    clear data;

    %% REMOVE SPECTRAL ABSORPTION

    j = 0; %index of absorption band
    Vabsorb = V; %copy over all data from original measurements
    for j = 1:1:length(absorbBands)

        [~, startBand] = min(abs(eta-absorbBands(j,1)));
        [~, stopBand] = min(abs(eta-absorbBands(j,2)));

        %grab data outside of absorption range
        %average Vref to reduce impact of noise
        Vref = [mean(V(startBand - 5:startBand - 1)),
mean(V(stopBand + 1:stopBand + 5))];
        etaRef = [eta(startBand - 1), eta(stopBand + 1)];

        Vabsorb(startBand:stopBand) = interp1(etaRef, Vref,
eta(startBand:stopBand));

    end


    %% BUTTERWORTH SMOOTHING FILTER

    % Filter order
    nf = 5;

    % Filter cutoff frequency -- increasing this number
decreases the
    % smoothing; decreasing this number increases the amount of
smoothing
    fc = 0.004; % from BFR %0.005; from Dr. Colton

    % Create filter
    [B,A] = butter(nf, fc);

    % Apply the butterworth filter to the previously filtered Vf
data
    Vfilter = filtfilt(B, A, Vabsorb);
```

```
    % Plot unfiltered data
    figure(1);
    hold all
    plot(eta,V,'b');
    title(strcat(tempstr,'C Calibration Data'))
    xlabel('wavenumber(cm-1)')
    ylabel('Intensity (volts)')

    % Add "maximum" filtered data to plot
    plot(eta,Vabsorb,'g');

    % Add butterworth filtered data to plot
    figure(1);
    plot(eta,Vfilter,'r');
    legend('raw','maximum','smoothed')

    save(strcat(calfilepath,filterfilename,tempstr,'.mat'),
'eta',  'Vfilter');

    FilterDataTime = toc

end

end

%% ----------------Documentation-------------------
%{

For the 04282016 calibration

cutoff(1:cutoffSplit1,1) = 1E-17;
cutoff(cutoffSplit1:cutoffSplit2,1) = 2E-18;
cutoff(cutoffSplit2:length(allAbsorb),1) = 5E-18;

fc = 0.004;

For the 02172016 calibration

cutoff(1:cutoffSplit1,1) = 1E-17;
cutoff(cutoffSplit1:cutoffSplit2,1) = 1E-18;
cutoff(cutoffSplit2:length(allAbsorb),1) = 5E-18;

fc = 0.005;



%}
```

A.1.3 MasterCalibration

```
function [] = MasterCalibration(calfilepath, filterfilename,
calibrationType, ...
    tempStart, tempEnd, tempStep, leftStart, rightEnd)

close all
tic

% set low and high temperatures in degrees C
tempLow = min(tempStart,tempEnd);
tempHigh = max(tempStart,tempEnd);
tempSpacing = abs(tempStep);

tempstr = num2str(tempLow);
load(strcat(calfilepath,filterfilename,tempstr,'.mat')); % open
a file to grab wavenumber bounds

if exist('nu','var'), eta = nu; end % this is temporary. Things
became a little inconsistent with eta and nu meaning the same
thing.
% In the future, everything will save as eta. Once all the nu's
are gone, this statement can be removed

[~, rowLowLeft] = min(abs(eta-leftStart)); %index of start and
stop wavenumbers
[~, rowHighRight] = min(abs(eta-rightEnd));
etaTruncated = eta(rowLowLeft:rowHighRight);

% read in original wavenumbers
i = 0;
clear eta Vfilter % close that file (we'll open them all in the
next section)

% generate BB intensity corresponding to each temperature
for temp = tempLow:tempSpacing:tempHigh

    i = i+1;

    tempstr = num2str(temp);
    load(strcat(calfilepath,filterfilename,tempstr,'.mat'));
    % variables: 'eta',  'Vfilter'
    V(:,i) = Vfilter(rowLowLeft:rowHighRight); %only desired
wavenumbers are saved

    bbInts(:,i) = PlanckIntensities(temp+273.15,
etaTruncated); % planck function operates in Kelvin
```

```
    clear eta nu Vfilter

end

%perform curve fit corresponding to each wavenumber
for j = 1:length(etaTruncated)

    fun = @(coeffsVar)CalibrationCoeffs(calibrationType,
coeffsVar, V(j,:), bbInts(j,:));

    if j == 1 % for the first iteration, use any intial guess
        if strcmp(calibrationType, 'Polynomial') == 1
            coeffs0 = [1,1]; % intial guess with 2 coefficients
        elseif strcmp(calibrationType,
'PowerAndExponentialOffset') == 1 || ...
                strcmp(calibrationType,
'Power2ExponentialOffset') == 1
            coeffs0 = [1,1,1,1]; % intial guess with 4
coefficients
        else
            coeffs0 = [1,1,1]; % intial guess for all except one
(most have 3 coefficients)
        end
    else
        coeffs0 = coeffs(j-1,:); % future guesses are whatever
was calculated for the last wavenumber
    end

    coeffs(j,:) = fminsearch(fun,coeffs0);
    RMSerror(j,:) = CalibrationCoeffs(calibrationType,
coeffs(j,:), V(j,:), bbInts(j,:)); % get the final RMS error

end

% plot coeffs to verify that they follow bb curve
i = 0;
hold on
for temp = tempLow:tempSpacing:tempHigh
    i = i+1;

    plot(etaTruncated, bbInts(:, i), 'o')
    title('Calibration Curve Fit')
    xlabel('Wavenumber (cm^{-1})');
    ylabel('Intensity (W/{m^2}/sr/cm^{-1}');
```

```
    intsMeas(:,i) = CalibrationEquation(calibrationType, coeffs,
V(:,i));

    plot(etaTruncated, intsMeas(:,i),'r','linewidth',2)
    legend('BB Intensity','Curve Fit')

end

% save coeffs
save(strcat(calfilepath,'Coeffs', calibrationType, '.mat'),
'coeffs', 'etaTruncated', 'RMSerror');

CalibrationCurveTime = toc

load train; sound(y,Fs)

end
```

A.1.4 CalibrationCoeffs

```
function [RMSerror] = CalibrationCoeffs(calibrationType, coeffs,
V, bbInts)

Imeas = CalibrationEquation(calibrationType, coeffs, V);

RMSerror = sqrt(sum((Imeas - bbInts).^2)/length(Imeas)); % solve
for 0, this function will be minimized

end
```

A.1.5 MasterProcessData

```
function [results] = MasterProcessData(kappafilepath,
calfilepath, ...
    measfilepath, measfilename, ~,...
    calibrationType, startdatafile, stopdatafile,
stepdatafile,...
    leftStart, rightEnd, broadbandType, useAreaRatios,
correlationfilepath, ~)

%read in optical pathlength data
pathlengthRaw = 0.152*ones(stopdatafile,1); % 6" diameter
pressurized rig %
xlsread(strcat(measfilepath,opticalpathfilename));
```

```
yco2Raw = xlsread(strcat(measfilepath,'input - CO2
concentration'));
pressureRaw = xlsread(strcat(measfilepath,'input - pressure'));

bandRange(1) = leftStart;
bandRange(2) = rightEnd;

bandBroadLeft = [4630-25,4630+25];
bandBroadRight = [6150-25,6150+25];

bandA = [5185, 5310];
bandB = [5310, 5435];
bandC = [5435, 5560];
bandE = [5615, 5715];

bandF = [3800, 3900];
bandG = [3900, 4000];
bandH = [4000, 4100];
bandJ = [5200, 5800];

bandsGas = [bandA; bandB; bandC; bandE; bandF; bandG; bandH;
bandJ];
bandH2O = bandE; % use band E, compareable result to using bands
A-C [5185 5560];
bandAratio = [bandA(1), bandE(2)]; % use all silica gas bands

tempGas = 1400; % initial guess at Tgas
Aratio = 1; % initial guess at intensity ratio (how much more we
are seeing in the test than during calibration)

iterLimit = 30; % max number of allowed iterations
iter = 1; % number of iterations performed

for i = startdatafile:stepdatafile:stopdatafile

    if i == 19
        i = i+1;
    end

    yh2o = 2*yco2Raw(i);
    yco2 = yco2Raw(i);
    pressure = pressureRaw(i);
    pathlength = pathlengthRaw(i);

    i
    tic
```

```
    j = 0; clear T % record the convergence of temperature

    [etaMeas, intsMeasRaw, ~] = VoltageToIntensity(calfilepath,
measfilepath, ...
        calibrationType, measfilename, i, bandRange); % convert
measured data to intensity values

    intsMeas = intsMeasRaw / Aratio; % reduce measured intensity
by area ratio

    gasTempChange = 1; %change of gasTemp between iterations
    AratioChange = 1;
    yh2oChange = 1;

    [gasKappa, etaModel] = MasterKappa(kappafilepath, 'h2o',
pressure, tempGas,...
        yh2o, bandRange(1), bandRange(2));
    gasEmissivityModel = 1 - exp(-gasKappa*pathlength); %
modeled gas emissivity

    while max(abs([gasTempChange, AratioChange, yh2oChange])) >
0.01/100 && iter < (iterLimit+1) % we add 1 to iter before
processeing

        gasEmissivity = interp1(etaModel, gasEmissivityModel,
etaMeas); % emissivity values that match measured wavenumbers

        if strcmp(broadbandType, 'no broadband removal') == 1
            broadbandConditions = [0,1]; % Twall = 0 K, emWall =
1
            integratedBroadabndIntensities = [0,0];
        else
            [broadbandConditions,
integratedBroadabndIntensities] = ProcessBroadband(intsMeas,
etaMeas, bandBroadLeft,...
                bandBroadRight);
        end

        AratioPrevious = Aratio;
        if strcmp(useAreaRatios, 'yes') == 1 % not entering this
loop leaves the area ratio as 1 (no effect)
            [Aratio] = ProcessAreaRatio(intsMeasRaw, etaMeas,
bandAratio, ...
                tempGas, gasEmissivity, broadbandConditions,
broadbandType);
```

```
            intsMeas = intsMeasRaw / Aratio; % reduce measured
intensity by area ratio
        end

        gasTempPrevious = tempGas; % save previous guess of gas
temperature
        [tempGas, tempsGas, integratedGasIntensities] =
ProcessTemperature(intsMeas, etaMeas, bandsGas,...
            gasEmissivity, gasTempPrevious, broadbandConditions,
pathlength, pressure, yh2o,...
            broadbandType, useAreaRatios, correlationfilepath);

        yh2oPrevious = yh2o;
        %           [yh2o, yco2, gasEmissivityModel] =
ProcessH2O(kappafilepath, intsMeas, etaMeas,...
        %               bandH2O, tempGas, broadbandConditions,
pressure(i), yh2o,...
        %               pathlength(i), broadbandType, fuelType);

        [gasKappa, etaModel] = MasterKappa(kappafilepath, 'h2o',
pressure, tempGas,...
            yh2o, bandRange(1), bandRange(2));
        gasEmissivityModel = 1 - exp(-gasKappa*pathlength);

        [tempGas, yh2o, broadbandConditions, Aratio, iter]

        j = j+1;
        T(j,:) = [tempsGas(1), tempsGas(2), tempsGas(3)];

        AratioChange = (Aratio - AratioPrevious) /
AratioPrevious; % percent change during iteration
        gasTempChange = (tempGas - gasTempPrevious) /
gasTempPrevious; % percent change during iteration
        yh2oChange = (yh2o - yh2oPrevious) / yh2oPrevious;


        iter = iter + 1; % how many times we have iterated on
this set of spectra

    end

    ProcessDataTime = toc

    if iter > (iterLimit-1) % if we reached iterlimit
        'reached iteration limit' % let the user know
        ProcessDataTime = floor(ProcessDataTime); % round
process time to make non-convergence obvious in results file
```

```
    end

    iter = 1; % reset iteration counter

    results(i,:) = [i, pathlength, pressure, tempsGas,
integratedGasIntensities, ...
        broadbandConditions, integratedBroadabndIntensities,
yh2o, yco2, Aratio, ProcessDataTime]; %combine results

    %% save the data
    % saves every iteration to ensure data isn't lost if an
error is found
    headers = {'Test', 'Path Length [m]', 'Pressure [atm]', ...
        'Gas T E/A [K]', 'Gas T E/B [K]', 'Gas T E/C [K]', ...
        'Gas T J/F [K]', 'Gas T J/G [K]', 'Gas T J/H [K]', ...
        'Gas T G/F [K]', 'Gas T H/F [K]', ...
        'Intensity A', 'Intensity B', 'Intensity C','Intensity
E',...
        'Intensity F', 'Intensity G', 'Intensity H','Intensity
J',...
        'Broadband T [K]', 'Broadband Emissivity','Intensity
B1','Intensity B2'...
        'Y H2O', 'Y CO2', 'Area Ratio', 'Time to Process
[sec]'};

    xlswrite(strcat(measfilepath,measfilename,'-Results
',calibrationType), headers, 1, 'A1');
    xlswrite(strcat(measfilepath,measfilename,'-Results
',calibrationType), results, 1, 'A2');

end

end
```

A.1.6 VoltageToIntensity

```
function [etaMeas, intsMeas, voltages] =
VoltageToIntensity(calfilepath, measfilepath, ...
    calibrationType, measfilename, i, bandAll)

% load conversion coefficients (variables: 'coeffsAll',
'etaTruncated');)
load(strcat(calfilepath,'Coeffs', calibrationType, '.mat'));

% Get bounding rows for left and right BG and A-E ratio
wavelength bands
```

```
[~, removeLow] = min(abs(etaTruncated-bandAll(1))); %
etaTruncated is from Coeffs file
[~, removeHigh] = min(abs(etaTruncated-bandAll(2)));

%Cut off unnecessary data and re-assign matrices
coeffs = coeffs(removeLow:removeHigh, :);


%% Open file, identify wavenumber band locations, prune measured
values to size,
% convert to intensities

% Get the raw test data
if i<10 %matches file format "...0001.csv" from OMNIC default
    numstr = strcat('000',num2str(i));
elseif i<100
    numstr = strcat('00',num2str(i));
elseif i<1000
    numstr = strcat('0',num2str(i));
else
    numstr = num2str(i);
end

rawData =
csvread(strcat(measfilepath,measfilename,numstr,'.csv'));

% Get bounding rows for left and right BG and A-E ratio
wavelength bands
rawWavenumbers = rawData(:,1);
[~, removeLow] = min(abs(rawWavenumbers-bandAll(1)));
[~, removeHigh] = min(abs(rawWavenumbers-bandAll(2)));

%Cut off unnecessary data and re-assign matrices
etaMeasRaw = rawData(removeLow:removeHigh, 1);
voltages = rawData(removeLow:removeHigh, 2);

intsMeas = CalibrationEquation(calibrationType, coeffs,
voltages);

if isreal(intsMeas) == false
    intsMeas = real(intsMeas);
    ImaginaryNumbers = 'yes'
end

etaMeas = etaMeasRaw + 0.167; % JT shift. good, but less helpful
in outside of silica region
```

```
% +(etaMeasRaw*3E-5 - .0143); % measured to model offset from
peak analysis


% save the measured data
save(strcat(measfilepath,measfilename,numstr,'meas',calibrationT
ype,'.mat'), 'etaMeas', 'intsMeas')

end
```

A.1.7 ProcessBroadband

```
function [broadbandConditions, integratedBroadabndIntensities] =
ProcessBroadband(intsMeas, etaMeas, bandBroadLeft,...
    bandBroadRight)

% This function will calculate the background temperature and
% emissivity based on 2-color pyrometry for a back wall or
% particles (no wall) in a region where gas emission ~ 0

% Get row information
intLeft = IntegrateIntensity(intsMeas, etaMeas,
bandBroadLeft(1), bandBroadLeft(2));
intRight = abs(IntegrateIntensity(intsMeas, etaMeas,
bandBroadRight(1), bandBroadRight(2)));

integratedBroadabndIntensities = [intLeft, intRight];

% ratio of broadbands
ratioMeasLR = intLeft / intRight;

% calculate temperature by comparing to Planck curve (two color
pyrometry method)
tempRange = 200:100:3000; %less refined initial run

for i = 1:2 %execute twice, once less refined and once more
refined

    for j = 1:1:length(tempRange)

        intsPlanck = PlanckIntensities(tempRange(j), etaMeas);

        intPlanckLeft = IntegrateIntensity(intsPlanck, etaMeas,
bandBroadLeft(1), bandBroadLeft(2));
        intPlanckRight = IntegrateIntensity(intsPlanck, etaMeas,
bandBroadRight(1), bandBroadRight(2));
```

```
        RatioLRPlanck(j) = intPlanckLeft / intPlanckRight;

    end

    tempBroadband = interp1(RatioLRPlanck, tempRange,
ratioMeasLR);

    tempRange = (tempBroadband-
150):.5:(tempBroadband+150); %more refined second run

end

tempBroadband = 842-50

%% Get the emissivity of the background

% Add up total planck values for em = 1, for each section
intsPlanck = PlanckIntensities(tempBroadband, etaMeas);

intPlanckLeft = IntegrateIntensity(intsPlanck, etaMeas,
bandBroadLeft(1), bandBroadLeft(2));
intPlanckRight = IntegrateIntensity(intsPlanck, etaMeas,
bandBroadRight(1), bandBroadRight(2));

emBroadbandLeft = intLeft / intPlanckLeft;
emBroadbandRight = intRight / intPlanckRight;

% get emissivity from intensities
emBroadband = mean([emBroadbandLeft, emBroadbandRight]); % these
values should be about the same
% that's how we chose our temperature (to make the ratio of
those values equal to that of a BB)

if emBroadband > 1
    emBroadband % print value to make user aware of the issue
   % emBroadband = 1;
end

broadbandConditions = [tempBroadband, emBroadband];

end
```

A.1.9 ProcessSAR

```
function [Aratio] = ProcessSAR(intsMeasRaw, etaMeas, bandAratio,
gasTemp, gasEmissivity,...
    broadbandConditions, broadbandType)

intsBroadband = PlanckIntensities(broadbandConditions(1),
etaMeas) * broadbandConditions(2); %broadband emission intensity
(particle or wall)
intsGas = PlanckIntensities(gasTemp, etaMeas) .* gasEmissivity;

if strcmp(broadbandType, 'emitting non-reflecting wall') == 1
    % wall, gas, sensor
    Aratios = intsMeasRaw ./ (intsBroadband.*(1-gasEmissivity) +
intsGas);

elseif strcmp(broadbandType, 'particles no wall') == 1
    % vacuum, gas & particles (optically thin = no interaction
between gas and particles), sensor
    Aratios = intsMeasRaw ./ (intsBroadband + intsGas);

end

[~,start] = min(abs(etaMeas - bandAratio(1)));
[~,stop] = min(abs(etaMeas - bandAratio(2)));

Aratio = mean(Aratios(start:stop));

if Aratio > 10
    Aratio % print value to make user aware of the issue (not
super common)
    Aratio = 10; % running into issues while code is converging.
Doesn't usually effect end result
end

end
```

A.1.8 ProcessTemperature

```
function [tempGas, tempsGas, integratedGasIntensities] =
ProcessTemperature(intsMeas, etaMeas, bandsGas,...
    gasEmissivity, tempGasPrev, broadbandConditions, pathLength,
pressure, yh2o,...
    broadbandType, useAreaRatios, correlationfilepath)
```

```
intsBroadband = PlanckIntensities(broadbandConditions(1),
etaMeas) * broadbandConditions(2); %broadband emission intensity
(particle or wall)

if strcmp(broadbandType, 'emitting non-reflecting wall') == 1

    if strcmp(useAreaRatios, 'yes') == 1 % if we use area
ratios, gasEmissivity ~ measured emissivity (we can use the
model)
        % wall, gas, sensor
        intsGas = intsMeas - intsBroadband .* (1 -
gasEmissivity);
    else % if we aren't using area ratios, we need to calculate
the emissivity from the measured gas
        intsGasBB = PlanckIntensities(tempGasPrev, etaMeas);
        % solving Ig = Imeas - Ibkg*(1-em) where em = Ig/Igbb
(rearrange to solve for Ig)
        intsGas = (intsMeas - intsBroadband) ./ (1 -
(intsBroadband./intsGasBB));
    end

elseif strcmp(broadbandType, 'particles no wall') == 1
    % vacuum, gas & particles (optically thin = no interaction
between gas and particles), sensor
    intsGas = intsMeas - intsBroadband;

elseif strcmp(broadbandType, 'no broadband') == 1
    intsGas = intsMeas;

end

intGasA = IntegrateIntensity(intsGas, etaMeas, bandsGas(1,1),
bandsGas(1,2));
intGasB = IntegrateIntensity(intsGas, etaMeas, bandsGas(2,1),
bandsGas(2,2));
intGasC = IntegrateIntensity(intsGas, etaMeas, bandsGas(3,1),
bandsGas(3,2));
intGasE = IntegrateIntensity(intsGas, etaMeas, bandsGas(4,1),
bandsGas(4,2));

intGasF = IntegrateIntensity(intsGas, etaMeas, bandsGas(5,1),
bandsGas(5,2));
intGasG = IntegrateIntensity(intsGas, etaMeas, bandsGas(6,1),
bandsGas(6,2));
intGasH = IntegrateIntensity(intsGas, etaMeas, bandsGas(7,1),
bandsGas(7,2));
```

```
intGasJ = IntegrateIntensity(intsGas, etaMeas, bandsGas(8,1),
bandsGas(8,2));

integratedGasIntensities = [intGasA, intGasB, intGasC,
intGasE, ...
    intGasF, intGasG, intGasH, intGasJ];

% calcuate ratio bands for temperature curve fit
ratioGasEA = intGasE / intGasA;
ratioGasEB = intGasE / intGasB;
ratioGasEC = intGasE / intGasC;

ratioGasJF = intGasJ / intGasF;
ratioGasJG = intGasJ / intGasG;
ratioGasJH = intGasJ / intGasH;

ratioGasHF = intGasH / intGasF;
ratioGasGF = intGasG / intGasF;

% Get temperature from each band
load(correlationfilepath) % all intensities
%
'ModelA','ModelB','ModelC','ModelE','ModelF','ModelG','ModelH','
ModelJ', ...
% 'bandsAllC', 'pressureC', 'yh2oC', 'pathlengthC', 'tempC'

EA = ModelE ./ ModelA;
EB = ModelE ./ ModelB;
EC = ModelE ./ ModelC;

JF = ModelJ ./ ModelF;
JG = ModelJ ./ ModelG;
JH = ModelJ ./ ModelH;

HF = ModelH ./ ModelF;
GF = ModelG ./ ModelF;

for i = 1:length(tempC) % interpolate known conditions to find
ratioModelEA @ conditions = f(Temperature)

    EAofT(i) = interpn(pressureC, yh2oC, pathlengthC,...
        EA(:,:,:,i), pressure, yh2o, pathLength, 'spline');
    EBofT(i) = interpn(pressureC, yh2oC, pathlengthC,...
        EB(:,:,:,i), pressure, yh2o, pathLength, 'spline');
    ECofT(i) = interpn(pressureC, yh2oC, pathlengthC,...
        EC(:,:,:,i), pressure, yh2o, pathLength, 'spline');
```

```
    JFofT(i) = interpn(pressureC, yh2oC, pathlengthC,...
        JF(:,:,:,i), pressure, yh2o, pathLength, 'spline');
    JGofT(i) = interpn(pressureC, yh2oC, pathlengthC,...
        JG(:,:,:,i), pressure, yh2o, pathLength, 'spline');
    JHofT(i) = interpn(pressureC, yh2oC, pathlengthC,...
        JH(:,:,:,i), pressure, yh2o, pathLength, 'spline');

    HFofT(i) = interpn(pressureC, yh2oC, pathlengthC,...
        HF(:,:,:,i), pressure, yh2o, pathLength, 'spline');
    GFofT(i) = interpn(pressureC, yh2oC, pathlengthC,...
        GF(:,:,:,i), pressure, yh2o, pathLength, 'spline');

end

    % interpolate temperature = f(ratioEA @ conditions) to find
temperature @ EA measured
    tempEA = interp1(EAofT, tempC, ratioGasEA, 'spline');
    tempEB = interp1(EBofT, tempC, ratioGasEB, 'spline');
    tempEC = interp1(ECofT, tempC, ratioGasEC, 'spline');

    tempJF = interp1(JFofT, tempC, ratioGasJF, 'spline');
    tempJG = interp1(JGofT, tempC, ratioGasJG, 'spline');
    tempJH = interp1(JHofT, tempC, ratioGasJH, 'spline');

    tempHF = interp1(HFofT, tempC, ratioGasHF, 'spline');
    tempGF = interp1(GFofT, tempC, ratioGasGF, 'spline');

    % Compile results
    tempGasSilica = mean([tempEA, tempEB, tempEC]);
    tempGasSapphire = mean([tempHF, tempGF]);
    tempGasMixed = mean([tempJF, tempJG, tempJH]);

    tempsGas(1) = tempEA;
    tempsGas(2) = tempEB;
    tempsGas(3) = tempEC;

    tempsGas(4) = tempJF;
    tempsGas(5) = tempJG;
    tempsGas(6) = tempJH;

    tempsGas(7) = tempHF;
    tempsGas(8) = tempGF;

    tempGas = tempGasSilica; % most trusted thus far

    if abs(1200 - tempGas) > 800 %verify temperature is
reasonable (define reasonable...)
```

```
        tempGas % print tempGas, it seems off
    end

end
```

A.2 Correlation Generating Code

Correlations refer to the relationship between the ratio of integrated gas temperature bands and gas temperature. Those correlations are then used to calculate gas temperature by comparing the measured integrated spectral band ratios to these generated models.

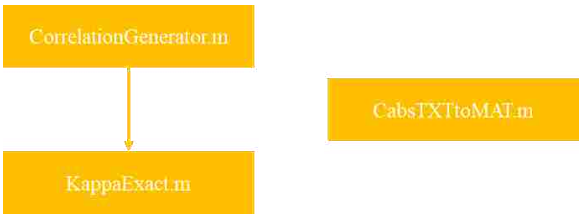

Figure A-2: CorrelationGenerator flow chart

A.2.1 CorrelationGenerator

```
% THIS CODE TAKES A VERY LONG TIME TO RUN (at least an hour for
the whole thing)

close all
clear
clc
tic

% this code is set up to generate all of the ratio values needed
to
% calculated temperature. Previously, these were turned into
polynomial
% curve fits. This required verifying that the curve fits
worked.
% Currently, all of the data is saved (it's really not that
much) and the
```

```
% temperature is calculated by interpolating between values.
Note that it
% isn't that simple (it's a multilayered thing with pressure,
pathlength,
% concentration, and temperature) but it works pretty well and
avoids curve
% fit issues.

% Cabs values have units of cm^2/molecule
% kappa values have units of 1/m

% Define band beginning and end points

kappafilepath = 'E:/';

bandA = [5185, 5310];
bandB = [5310, 5435];
bandC = [5435, 5560];
bandE = [5615, 5715];

bandF = [3800, 3900];
bandG = [3900, 4000];
bandH = [4000, 4100];
bandJ = [5200, 5800];

bandsAll = [bandA; bandB; bandC; bandE; bandF; bandG; bandH;
bandJ];

nuMin = min(bandsAll(:));
nuMax = max(bandsAll(:));

pressure = [.5, 1, 2, 4, 8, 15, 30, 50]';
for p = 1:length(pressure)

    yh2o = [.05, .10, .20, .30, .40]';
    for y = 1:length(yh2o)

        temp = (300:100:3000)';
        for t = 1:length(temp)

            %print the conditions being calculated for reference
            pressure(p)
            yh2o(y)
            temp(t)

            % calculate H2O kappas
```

```
            [kappasH2O, eta] = MasterKappa(kappafilepath, 'h2o',
pressure(p),...
                temp(t), yh2o(y), nuMin, nuMax); %returns [eta,
kappa]

            % calculate planck intensities
            planckInts = PlanckIntensities(temp(t), eta);

            pathlength = (.02:.02:1)';
            for pl = 1:length(pathlength)

                % calculate emisivities
                emissivities = 1 - exp(-kappasH2O *
pathlength(pl));

                reflectivity = (0:0.1:1)';
                for r = 1:length(reflectivity)

                    intsGas = planckInts .* emissivities .*...
                        (1 + reflectivity(r)*(1-emissivities));

                    % integrate bands
                    ModelA(p,y,pl,r,t) =
IntegrateIntensity(intsGas,...
                        eta, bandA(1), bandA(2));
                    ModelB(p,y,pl,r,t) =
IntegrateIntensity(intsGas,...
                        eta, bandB(1), bandB(2));
                    ModelC(p,y,pl,r,t) =
IntegrateIntensity(intsGas,...
                        eta, bandC(1), bandC(2));
                    ModelE(p,y,pl,r,t) =
IntegrateIntensity(intsGas,...
                        eta, bandE(1), bandE(2));

                    ModelF(p,y,pl,r,t) =
IntegrateIntensity(intsGas,...
                        eta, bandF(1), bandF(2));
                    ModelG(p,y,pl,r,t) =
IntegrateIntensity(intsGas,...
                        eta, bandG(1), bandG(2));
                    ModelH(p,y,pl,r,t) =
IntegrateIntensity(intsGas,...
                        eta, bandH(1), bandH(2));
                    ModelJ(p,y,pl,r,t) =
IntegrateIntensity(intsGas,...
                        eta, bandJ(1), bandJ(2));
```

```
                    clear intsGas

                end %end reflectivity loop

                clear emissivities

            end %end pathlength loop

        end %end temp loop

        %                 hold on
        %                 plot(temp, ratioEA, 'LineWidth',2)
        %                 plot(temp, ratioEB, 'LineWidth',2)
        %                 plot(temp, ratioEC, 'LineWidth',2)
        %                 plot(temp, ratioCB, 'LineWidth',2)
        %                 plot(temp, 1./ratioCA, 'LineWidth',2)
        %                 plot(temp, 1./ratioBA, 'LineWidth',2)
        %
legend('E/A','E/B','E/C','C/B','A/C','A/B')

        clear kappasH2O eta planckInts

    end %end yh2o loop

end %end pressure loop

bandsAllC = bandsAll; % add C (correlation) at the end to avoid
confusion when opening
pathlengthC = pathlength;
pressureC = pressure;
yh2oC = yh2o;
tempC = temp;
reflectivityC = reflectivity;

save('C:\Users\Scott\Documents\MATLAB\CabsDatabaseFiles\Calibrat
ionIntensities',...

'ModelA','ModelB','ModelC','ModelE','ModelF','ModelG','ModelH','
ModelJ', ...
    'bandsAllC', 'pressureC', 'yh2oC', 'pathlengthC',
'reflectivityC', 'tempC')

toc
```

A.2.2 KappaExact

```
function [kappa, nu] = KappaExact(gasName, pressure, Tgas, yGas,
nuLow, nuHigh)

% Don't bother interpolating if you are doing modeling work
% will speed correlation and modeling calculations considerably
% the only issue is, you have to get it right! (no
interpolation)
% I hope to integrate this with the normal kappa files, so that
it can
% recognize when it doesn't need to interpolate.

datafilepath = 'C:\Users\Scott\Documents\Working Files\Cabs
Data\';

if strcmp(gasName, 'h2o') == 1
    % location of the H2O absorption cross section database
(Pearson)
    fileLoc =
strcat(datafilepath,'relevantH2OCabsDatabaseFiles\');

elseif strcmp(gasName, 'co2') == 1
    % location of the CO2 absorption cross section database
    fileLoc =
strcat(datafilepath,'relevantCO2CabsDatabaseFiles\');

else
    gasName = throwerror; %if executed, this will throw an error

end

databaseLoc = 'throwerror'; % for now, I don't want this to
execute

%% determine files to use for linear interpolation.
% This allows the function to interpolate based on pressure,
tempearture,
% and concentration (molar). These values are based on what is
available
% in Pearson's database.

% determine high and low concentrations for tabulated data
if strcmp(gasName, 'h2o')

    [~, yStr] = KappaConcentration(yGas);
```

```
elseif strcmp(gasName, 'co2')
    % if gas is CO2 all concentrations are 0 for looking up the
    % files. This is important because Pearson's database does
not
    % provide different values for the different concentrations
of CO2,
    % as he found it to be a negligible parameter in determining
CO2
    % absorption cross sections.
    yStr = {'0';'0'};

end

[~, pStr] = KappaPressure(pressure); %same for both CO2, H2O

%% linear interpolation scheme
% interpolation order goes pressure, then concentration, then
temperature
% it will first check to see if the given value matches the
values in the
% data base. If they do not, it will then linearly interpolate
accordingly

% interpolate by pressure (first), then concentration (second),
then temperature (third)
[Cabs, nu] = KappaRawData(fileLoc, gasName, Tgas, yStr(1),
pStr(1), nuHigh, nuLow);

%% convert Cabs to kappa, prepare to return values to calling
function

Ru = 0.8205; % universal gas constant, cm^2 * m / mol / K
Na = 6.02214085774 * (10^23); % avogadro's number, molecules /
mol

kappa = Cabs * ((yGas * pressure) ./ (Ru * Tgas)) * Na;

end
```

A.2.3 CabsTXTtoMAT

```
% This code will find relevant Cabs files in the database for
water. Once a
% relevant file has been found, it will be loaded, split into
wavenumbers
```

```
% and Cabs values, and saved as a .mat file. These new files
will load in
% .5s, as compared to 6.5-25s with various methods of loading
the currently
% existing files.

% search through the relevant folder
files = dir('D:\Cabs_Absorption Coefficients_co2\*.txt');
for file = files'
    % make sure it's a .txt file
    if strcmp(file.name(end-2:end), 'txt') == 1
        % make sure it's a file for the right gas
        if strcmp(file.name(6:8), 'co2') == 1
            % search through it looking for the temperature
                % find K
                tempLoc = strfind(file.name, 'K');
            tempStr = file.name(10:tempLoc-1);
            tempNum = str2double(tempStr);

            if tempNum == 900 %>= 299 && tempNum <= 700
            % if it's a relevant temperature, find the
concentration
                concStart = tempLoc + 3;
                postConcBlank =
strfind(file.name(concStart:end), ' ');
                concEnd = (postConcBlank - 2) + concStart;
                concStr = file.name(concStart:concEnd);

                if strcmp(concStr, '0') == 1 || strcmp(concStr,
'05') == 1 || strcmp(concStr, '1') == 1  ...
                     || strcmp(concStr, '2') == 1 ||
strcmp(concStr, '3') == 1 ...
                     || strcmp(concStr, '4') == 1;
                % if it's a relevant concentration, find the
pressure
                    pressStart = concEnd + 3;
                    pressureStr = file.name(pressStart:end-4);

                    if strcmp(pressureStr, '4') == 1 || ...
                       strcmp(pressureStr, '8') == 1 || ...
                       strcmp(pressureStr, '15') == 1 || ...
                       strcmp(pressureStr, '30') == 1 || ...
                       strcmp(pressureStr, '50') == 1
                    % if it's a relevant pressure, load the file
                        % save the file name
                        dataA = fopen(strcat('D:\Cabs_Absorption
Coefficients_co2\', ...
```

```
                                        file.name));
                        dataB = textscan(dataA, '%f %f');

                        fileNameA = file.name(1:end-3); % cut
off the txt
                        fileName = strcat(fileNameA, 'mat');

                        % store the cabs values
                        rawDataCabs = dataB{:, 2};

                        % generate the wavenumbers
                        rawDataWavenumbers =
transpose(0:0.005:0.005*size(dataB{1,1},1)-0.005);%25000

                        rawDataCabs = cat(2,
rawDataWavenumbers, ...
                                          rawDataCabs);

                        % save these values as a .mat file,
using the old file
                        % name as a base.

save(strcat('C:\Users\Scott\Documents\MATLAB\CabsDatabaseFiles\'
, ...
                                        fileName), 'rawDataCabs')
                    else
                    end
                else
                end
            else
            end
        else
        end
    else
    end
end
```

A.3 Radiation Coefficients Code

Radiative absorption coefficients are generated using a HITEMP derivative spectral database generated by Pearson [21]. Coefficient values at a given concentration and pressure are generated from the spectral database as shown.

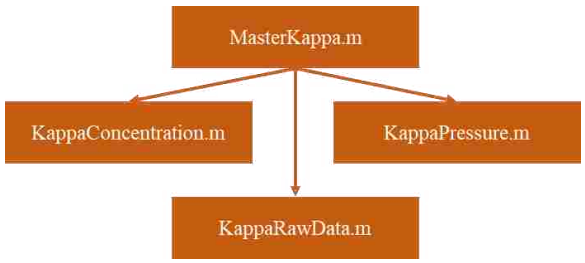

Figure A-3: MasterKappa flow chart

A.3.1 MasterKappa

```
function [kappa, nu] = MasterKappa(kappafilepath, gasName,
pressure, Tgas, yGas, nuLow, nuHigh)

% Author: John Tobiasson
% Date: 04/07/2016
% Purpose: This function will caclculate an array of gas
emissivities for a
% given set of conditions, from John Person's Cabs data. The
resulting array
% will be passed to another program. The Cabs used will be
created from
% interpolating between temperature and concentration files.

if strcmp(gasName, 'h2o') == 1
    % location of the H2O absorption cross section database
(Pearson)
    fileLoc =
strcat(kappafilepath,'relevantH2OCabsDatabaseFiles\');

elseif strcmp(gasName, 'co2') == 1
    % location of the CO2 absorption cross section database
    fileLoc =
strcat(kappafilepath,'relevantCO2CabsDatabaseFiles\');

else
    gasName = throwerror; %if executed, this will throw an error

end

%% determine files to use for linear interpolation.
% This allows the function to interpolate based on pressure,
tempearture,
```

```
% and concentration (molar). These values are based on what is
available
% in Pearson's database.

if rem(Tgas, 100) == 0 % if the gas temperature is a multiple of
100, no need to interpolate

    gasT = Tgas;

else

    gasT(1) = ceil(Tgas/100) * 100; % round Tgas up to the
nearest 100
    gasT(2) = gasT(1) - 100;

end

% determine high and low concentrations for tabulated data
if strcmp(gasName, 'h2o')

    [yVal, yStr] = KappaConcentration(yGas);
    % returns 1 element if we don't need to interpolate, 2 if we
do (bounding
    % concentrations in the database)

elseif strcmp(gasName, 'co2')
    % if gas is CO2 all concentrations are 0 for looking up the
    % files. This is important because Pearson's database does
not
    % provide different values for the different concentrations
of CO2,
    % as he found it to be a negligible parameter in determining
CO2
    % absorption cross sections.
    yVal = 0;
    yStr = {'0'};

end

[pVal, pStr] = KappaPressure(pressure); %same for both CO2, H2O
% returns 1 element if we don't need to interpolate, 2 if we do
(bounding
% pressures in the database)

%% linear interpolation scheme
% interpolation order goes pressure, then concentration, then
temperature
```

```
% it will first check to see if the given value matches the
values in the
% data base. If they do not, it will then linearly interpolate
accordingly

if length(gasT) == 1 && length(yVal) == 1 && length(pVal) == 1

    [Cabs, nu] = KappaRawData(fileLoc, gasName, gasT, yStr,
pStr, nuHigh, nuLow);

else % if we have to interpolate 1 of the 3, let's just do it
for all of them
    % (since we probably aren't modeling, we have measured data)

    if length(gasT) == 1

        gasT(2) = gasT(1);

    end

    if length(yVal) == 1

        yStr(2) = yStr(1);
        yVal(2) = yVal(1);

    end

    if length(pVal) == 1

        pStr(2) = pStr(1);
        pVal(2) = pVal(1);

    end

    % interpolate by pressure (first), then concentration
(second), then temperature (third)
    [Cabs111, nu] = KappaRawData(fileLoc, gasName, gasT(1),
yStr(1), pStr(1), nuHigh, nuLow);
    [Cabs112, ~] = KappaRawData(fileLoc, gasName, gasT(1),
yStr(1), pStr(2), nuHigh, nuLow);
    [Cabs121, ~] = KappaRawData(fileLoc, gasName, gasT(1),
yStr(2), pStr(1), nuHigh, nuLow);
    [Cabs122, ~] = KappaRawData(fileLoc, gasName, gasT(1),
yStr(2), pStr(2), nuHigh, nuLow);
    [Cabs211, ~] = KappaRawData(fileLoc, gasName, gasT(2),
yStr(1), pStr(1), nuHigh, nuLow);
```

```
    [Cabs212, ~] = KappaRawData(fileLoc, gasName, gasT(2),
yStr(1), pStr(2), nuHigh, nuLow);
    [Cabs221, ~] = KappaRawData(fileLoc, gasName, gasT(2),
yStr(2), pStr(1), nuHigh, nuLow);
    [Cabs222, ~] = KappaRawData(fileLoc, gasName, gasT(2),
yStr(2), pStr(2), nuHigh, nuLow);

    fractionP = (pressure-pVal(1))/(pVal(2)-pVal(1)); %
percentage pressure is from PLow (w/ ref to PHigh)
    Cabs11 = fractionP * (Cabs112 - Cabs111) + Cabs111; % linear
interpolation of P for each pair of T, Y
    Cabs12 = fractionP * (Cabs122 - Cabs121) + Cabs121;
    Cabs21 = fractionP * (Cabs212 - Cabs211) + Cabs211;
    Cabs22 = fractionP * (Cabs222 - Cabs221) + Cabs221;

    if strcmp(gasName, 'h2o')
        fractionY = (yGas-yVal(1))/(yVal(2)-yVal(1)); %
percentage Y is from YLow (w/ ref to YHigh)
    elseif strcmp(gasName, 'co2')
        fractionY = 1; % Cabs != f(yCO2)
    end
    Cabs1 = fractionY * (Cabs12 - Cabs11) + Cabs11; % linear
interpolation of Y for each pair of T
    Cabs2 = fractionY * (Cabs22 - Cabs21) + Cabs21;

    fractionT = (Tgas-gasT(1))/(gasT(2)-gasT(1)); % percentage
gasT is from TLow (w/ ref to THigh)
    fractionT(isnan(fractionT)) = 0; % NAN when the T is
divisible by 100. bandaid. needs TLC
    Cabs = fractionT * (Cabs2 - Cabs1) + Cabs1; % linear
interpolation of T
end

%% convert Cabs to kappa, prepare to return values to calling
function

Ru = 0.8205; % universal gas constant, cm^2 * m / mol / K
Na = 6.02214085774 * (10^23); % avogadro's number, molecules /
mol

kappa = Cabs * ((yGas * pressure) ./ (Ru * Tgas)) * Na;

end
```

A.3.2 KappaConcentration

```
function [yVal, yStr] = KappaConcentration(yH2O)

% in conjunction with Pearson database, determine which file to
open based
% on the gas concentration (H2O only, CO2 =! f(concentration) in
Pearson)

if yH2O == 0.05

    yVal = 0.05;
    yStr = {'05'};

elseif yH2O == 0.1

    yVal = 0.1;
    yStr = {'1'};

elseif yH2O == 0.2

    yVal = 0.2;
    yStr = {'2'};

elseif yH2O == 0.3

    yVal = 0.3;
    yStr = {'3'};

elseif yH2O == 0.4

    yVal = 0.4;
    yStr = {'4'};

elseif yH2O == 0.6

    yVal = 0.6;
    yStr = {'6'};

elseif yH2O == 0.8

    yVal = 0.8;
    yStr = {'8'};

elseif yH2O == 1

    yVal = 1.0;
```

```
    yStr = {'10'};

    %% what happens if we don't get it exactly right? set up to
interpolate later
elseif yH2O <= 0.05

    yVal = [0; 0.05];
    yStr = {'0'; '05'};

elseif yH2O <= 0.1

    yVal = [0.05; 0.1];
    yStr = {'05'; '1'};

elseif yH2O <= 0.2

    yVal = [0.1; 0.2];
    yStr = {'1'; '2'};

elseif yH2O <= 0.3

    yVal = [0.2; 0.3];
    yStr = {'2'; '3'};

elseif yH2O <= 0.4

    yVal = [0.3; 0.4];
    yStr = {'3'; '4'};

elseif yH2O <= 0.6

    yVal = [0.4; 0.6];
    yStr = {'4'; '6'};

elseif yH2O <= 0.8

    yVal = [0.6; 0.8];
    yStr = {'6'; '8'};

elseif yH2O <= 1

    yVal = [0.8; 1.0];
    yStr = {'8'; '10'};

end
end
```

A.3.3 KappaPressure

```
function [pVal, pStr] = KappaPressure(pressure)

% in conjunction with Pearson database, determine which file to
open based
% on the total pressure (H2O and CO2 use common pressure
increments)


if pressure == 0.1

    pVal = 0.1;
    pStr = {'01'};

elseif pressure == 0.25

    pVal = 0.25;
    pStr = {'025'};

elseif pressure == 0.5

    pVal = 0.5;
    pStr = {'05'};

elseif pressure == 1

    pVal = 1;
    pStr = {'1'};

elseif pressure == 2

    pVal = 2;
    pStr = {'2'};

elseif pressure == 4

    pVal = 4;
    pStr = {'4'};

elseif pressure == 8

    pVal = 8;
    pStr = {'8'};

elseif pressure == 15
```

```
    pVal = 15;
    pStr = {'15'};


elseif pressure == 30

    pVal = 30;
    pStr = {'30'};

elseif pressure == 50

    pVal = 50;
    pStr = {'50'};

%% what if we don't get it exactly right? we need to interpolate
later
elseif pressure <= 0.1

    pVal = [0; 0.1];
    pStr = {'0'; '01'};

elseif pressure <= 0.25

    pVal = [0; 0.25];
    pStr = {'0'; '025'};

elseif pressure <= 0.5

    pVal = [0; 0.5];
    pStr = {'0'; '05'};

elseif pressure <= 1

    pVal = [0.5; 1];
    pStr = {'05'; '1'};

elseif pressure <= 2

    pVal = [1; 2];
    pStr = {'1'; '2'};

elseif pressure <= 4

    pVal = [2; 4];
    pStr = {'2'; '4'};

elseif pressure <= 8
```

```
    pVal = [4; 8];
    pStr = {'4'; '8'};

elseif pressure <= 15

    pVal = [8; 15];
    pStr = {'8'; '15'};


elseif pressure <= 30

    pVal = [15; 30];
    pStr = {'15'; '30'};

else

    pVal = [30; 50];
    pStr = {'30'; '50'};

end

end
```

A.3.4 KappaRawData

```
function [Cabs, eta] = KappaRawData(fileLoc, gasName, Temp,
concStrs, pressStrs, etaHigh, etaLow)

filenameCabs = strcat({fileLoc}, {'Cabs '},{gasName},{' '}, ...
    num2str(Temp), {'K Y'}, concStrs, {' P'}, pressStrs,...
    {'.mat'});

% check if the file exists.
if exist(filenameCabs{1}, 'file') == 2

    rawDataCabs = load(filenameCabs{1});
    fieldName = fields(rawDataCabs);
    rawDataCabs1 = rawDataCabs.(fieldName{1});

else % if .mat file does not exist, try to load the .txt version

    loadFilename = strcat(databaseLoc, gasName,'\', ...
        filenameCabs{1}((size(fileLoc,2)+1):(end-3)),'txt');
    fileID = fopen(loadFilename);
```

```
    rawDataCabs = textscan(fileID,'%s %s');
    rawDataCabs1 = zeros(size(rawDataCabs{1,1},1), 2);
    rawDataCabs1(:,1) = str2double(rawDataCabs{1, 1});
    rawDataCabs1(:,2) = str2double(rawDataCabs{1, 2});
    save(filenameCabs{1},'rawDataCabs1'); % save it as a .mat

end

% verify that all needed values are present for low wavenumbers
low = min(rawDataCabs1(:,1));

if low > etaLow % Cabs data does not go low enough (assume
unlisted Cabs = 0)

    indexLow = round((low - etaLow)/.005,5);
    addLow = zeros(indexLow,2); % assuming .005 cm-1 spacing
    rawDataCabs1 = vertcat(addLow,rawDataCabs1);

elseif low < etaLow % Cabs data goes too low (needs to be
truncated)

    [~, indexLow] = min(abs(rawDataCabs1(:, 1) - etaLow));
    rawDataCabs1 = rawDataCabs1(indexLow:end,:);

end

% verify that all needed values are present for high wavenumbers
high = max(rawDataCabs1(:,1));

if high < etaHigh % Cabs data does not go high enough (assume
unlisted Cabs = 0)

    indexHigh = round((etaHigh-high)/.005,5);
    addHigh = zeros(indexHigh,2); % assuming .005 cm-1 spacing
    rawDataCabs1 = vertcat(rawDataCabs1,addHigh);

elseif high > etaHigh % Cabs data goes too high (needs to be
truncated)

    [~, indexHigh] = min(abs(rawDataCabs1(:, 1) - etaHigh));
    rawDataCabs1 = rawDataCabs1(1:indexHigh,:);

end

eta = rawDataCabs1(:,1);
Cabs = rawDataCabs1(:,2);
end
```

A.4 Other Commonly Used Subroutines

Three other functions are commonly used in processing data. These functions are used in a variety of subroutines.

Figure A-4: Other commonly used subroutines

A.4.1 CalibrationEquation

```
function [ints] = CalibrationEquation(calibrationType, coeffs,
V)

% This function calculates the measured intensity for a given
measured
% voltage. It is used both when creating the calibrations and
when
% converting the gas measurements to intensity
%
% each "elseif" statement is the same, other that the equation
used and
% possibly the number of coefficients needed

if strcmp(calibrationType, 'polyABC') == 1

    A = coeffs(:,1); B = coeffs(:,2); C = coeffs(:,3);
    ints = A + B.*V + C.*V;

elseif strcmp(calibrationType, 'polyBC') == 1

    B = coeffs(:,1); C = coeffs(:,2);
    ints = B.*V + C.*V;

elseif strcmp(calibrationType, 'PowerAndExponential') == 1

    A = coeffs(:,1); B = coeffs(:,2); C = coeffs(:,3);
    ints = A * V.^B .* exp(C*V);

elseif strcmp(calibrationType, 'Power2Exponential') == 1

    A = coeffs(:,1); B = coeffs(:,2); C = coeffs(:,3);
```

```
    ints = A .* exp(B .* V.^C);

end

end
```

A.4.2 PlanckIntensities

```
function [bbInts] = PlanckIntensities(temp, eta) %, waveType)

% Date: 07/15/2016
% Author: John Tobiasson
% Purpose: This function will calculate blackbody intensities
for various
% temperatures for the wavenumbers of interest. The intensities
will be as
% W/m^2/sr/um, based off of wavenumbers. This will be used as
part of
% generating Cv values as functions of Mv and eta both.

% Temperatures must be in degrees C, and incrementable by 100 C.

% RevB Note: This revision no longer saves files, but is meant
to be called

h = 6.62606957 * (10^(-34));
k = 1.3806488 * (10^(-23));
c0 = 2.99792458 * (10^8);

waveType = 'length';

if strcmp(waveType, 'length') == 1

    bbInts = (2 * h * (c0^2) .* (eta.^5) * (10^4)) ./ ...
        (exp((h * c0 .* eta * 100) / (k * temp)) - 1);

elseif strcmp(waveType, 'number') == 1

    bbInts = (2 * h * (c0^2) .* (eta.^3) * (10^8)) ./ ...
        (exp((h * c0 .* eta * 100) / (k * temp)) - 1);

else

    waveType = throwerror; %unkown waveType
end
end
```

A.4.3 IntegrateIntensity

```
function [int] = IntegrateIntensity(ints, eta, start, stop,
waveType)

 if ~exist('waveType','var'), waveType = 'length'; end %
optional input

% integrates a function within the desired band

[~, indexStart] = min(abs(eta-start));
[~, indexStop] = min(abs(eta-stop));

% Get Cvs (correction constants), calc intensities, and sum
bands
intsTruncated = ints(indexStart:indexStop);
nuTruncated = eta(indexStart:indexStop);

if indexStart == indexStop

    int = 0;

elseif strcmp(waveType, 'number') == 1

    int = trapz(nuTruncated, intsTruncated);

elseif strcmp(waveType, 'length') == 1

    % get wavelength band values
    lambdatruncated = 10^4 ./ nuTruncated;

    % Change sums to integrals, flipping arrays so the integrals
are +
    int = trapz(flipud(lambdatruncated), flipud(intsTruncated));

else

    waveType = throwerror; %unkown waveType

end

end
```

APPENDIX B: HIGH PRESSURE OPTICAL PROBE DESIGN

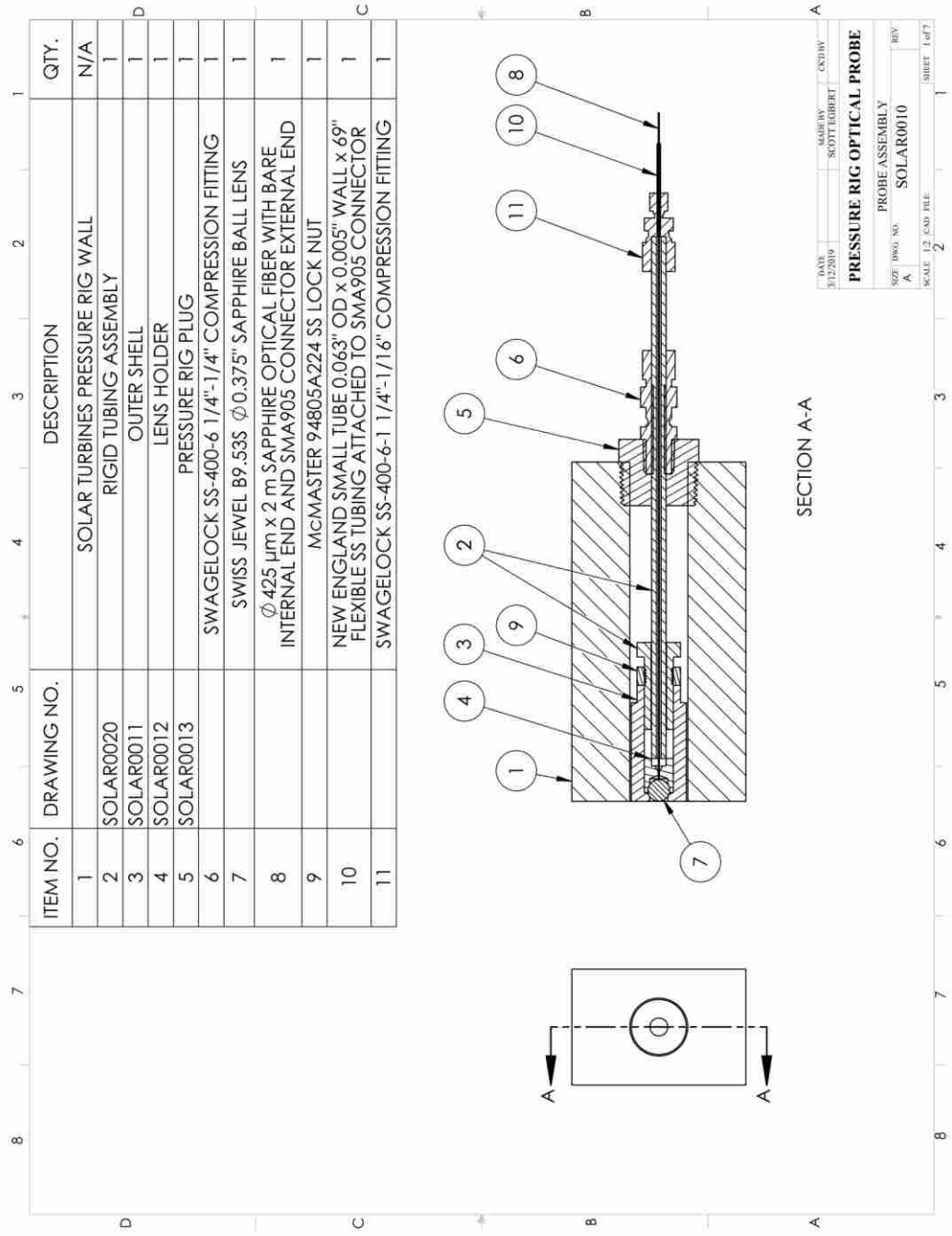

Figure B-1: Pressure rig optical probe, probe assembly

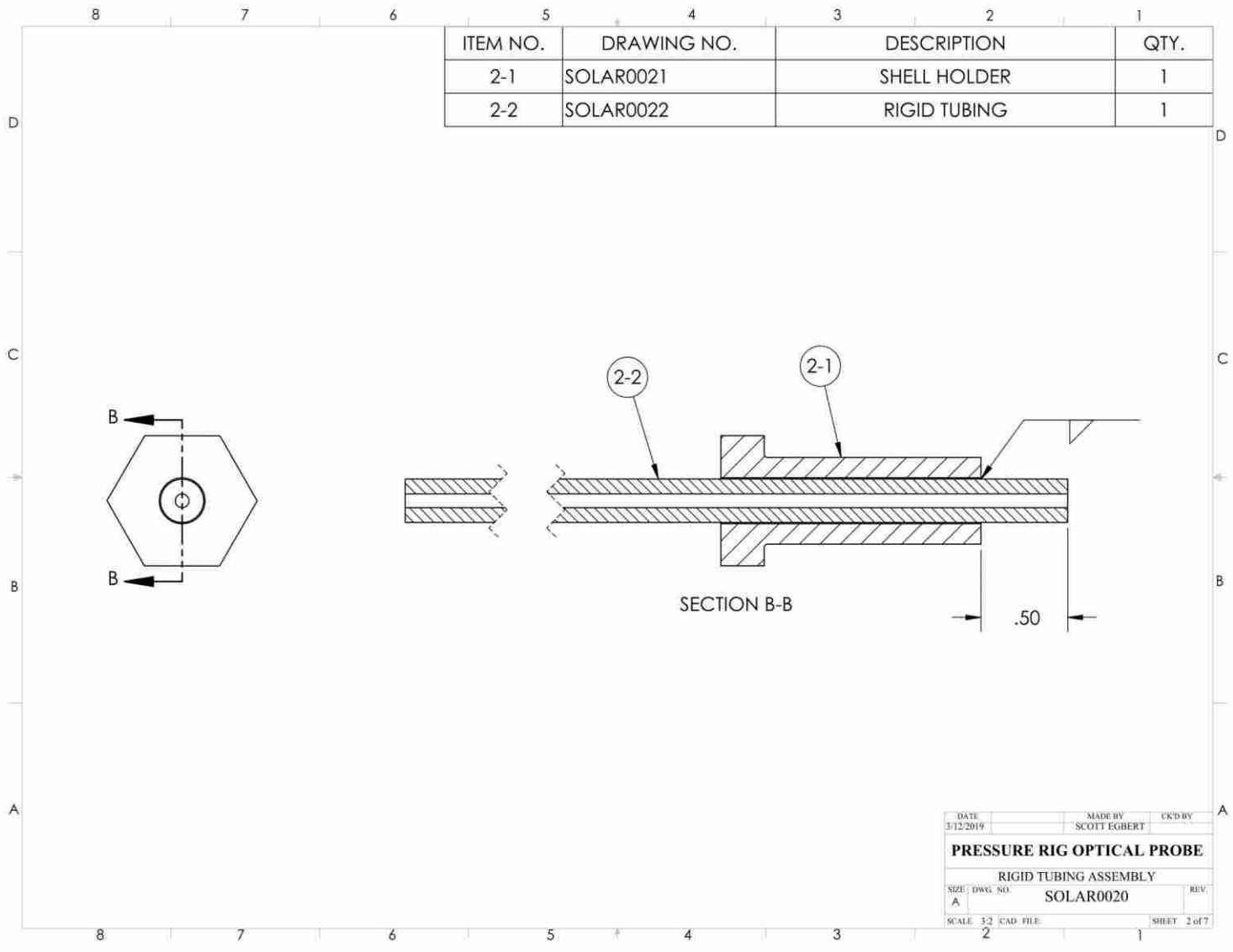

Figure B-2: Pressure rig optical probe, rigid tubing assembly

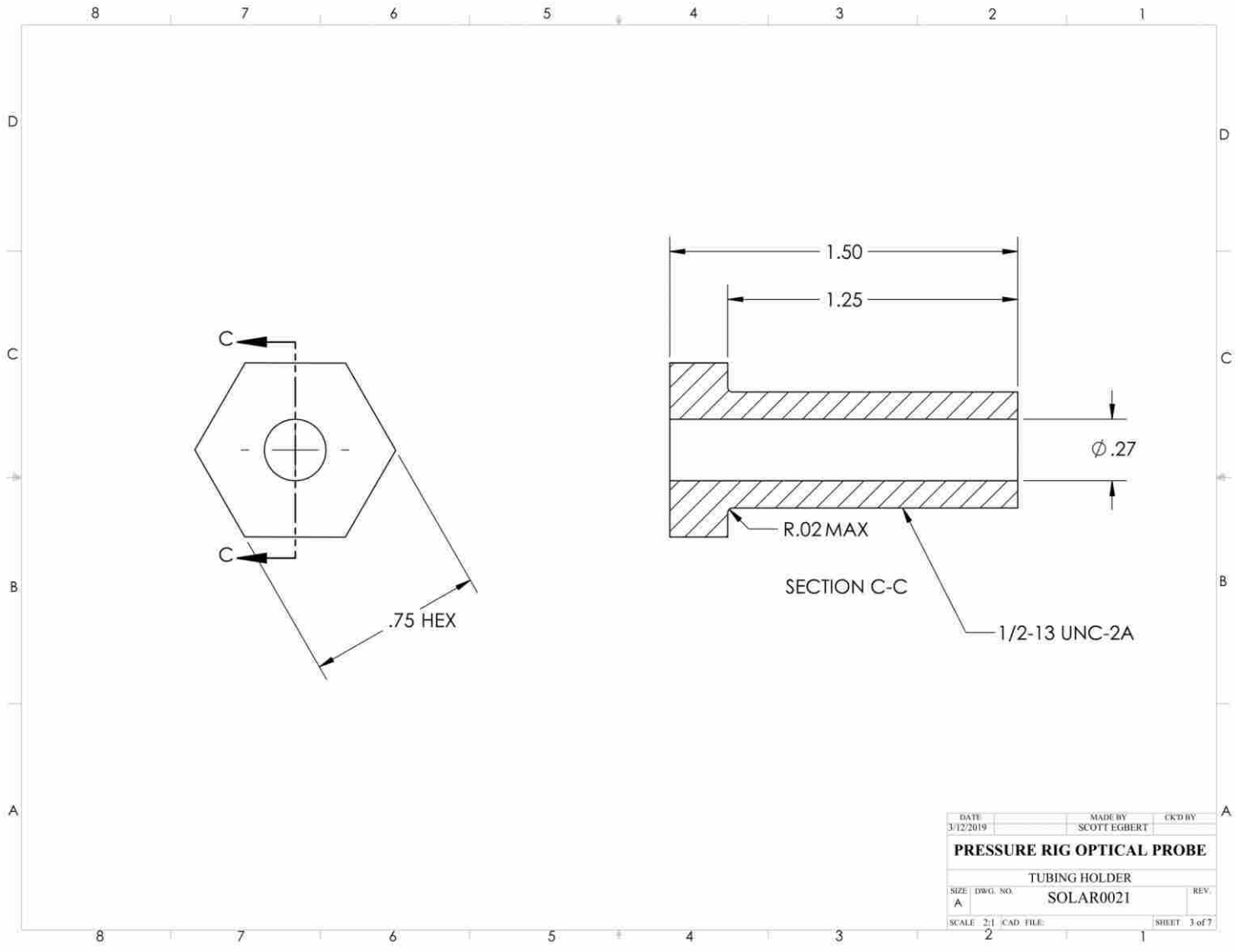

Figure B-3: Pressure rig optical probe, tubing holder

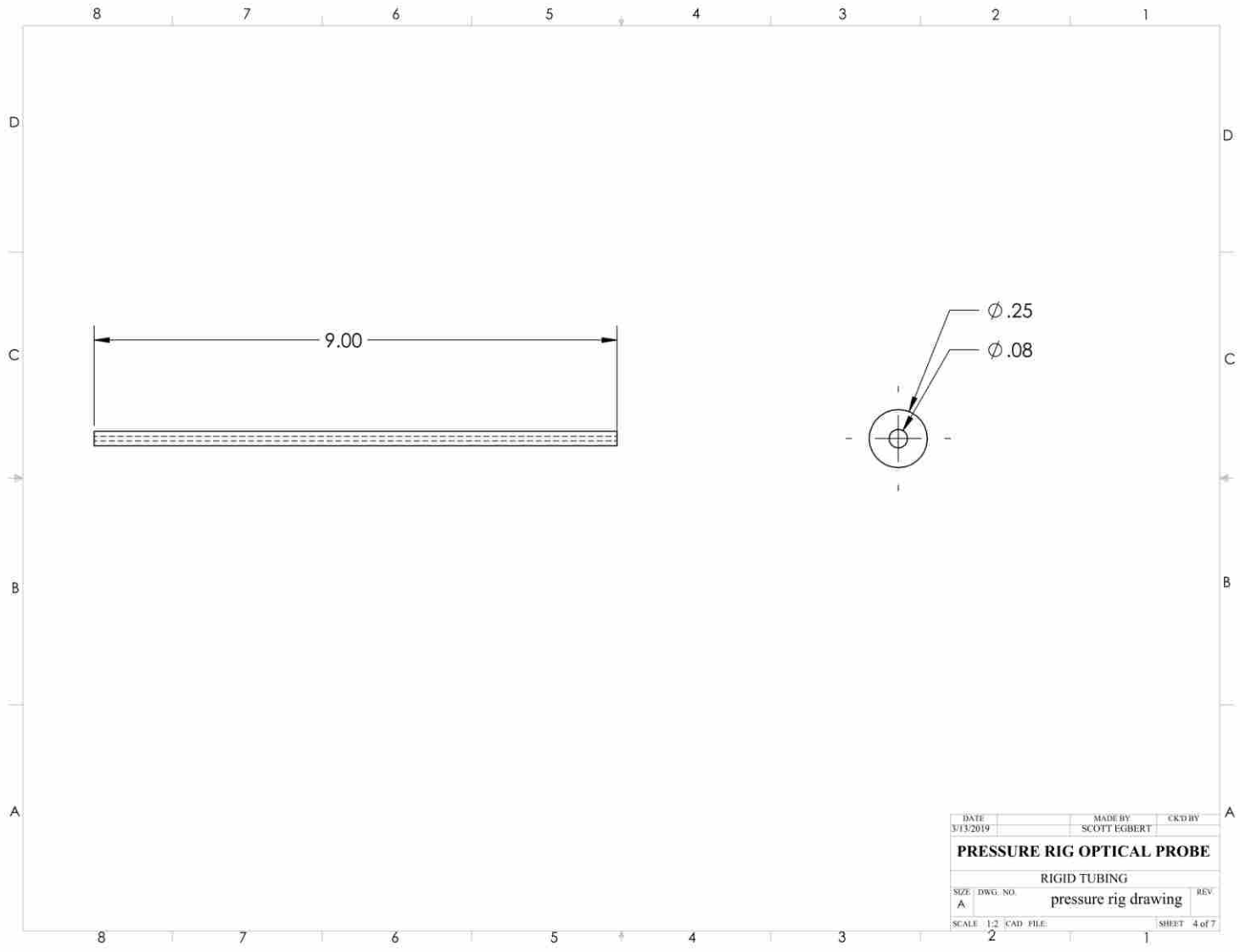

Figure B-4: Pressure rig optical probe, rigid tubing

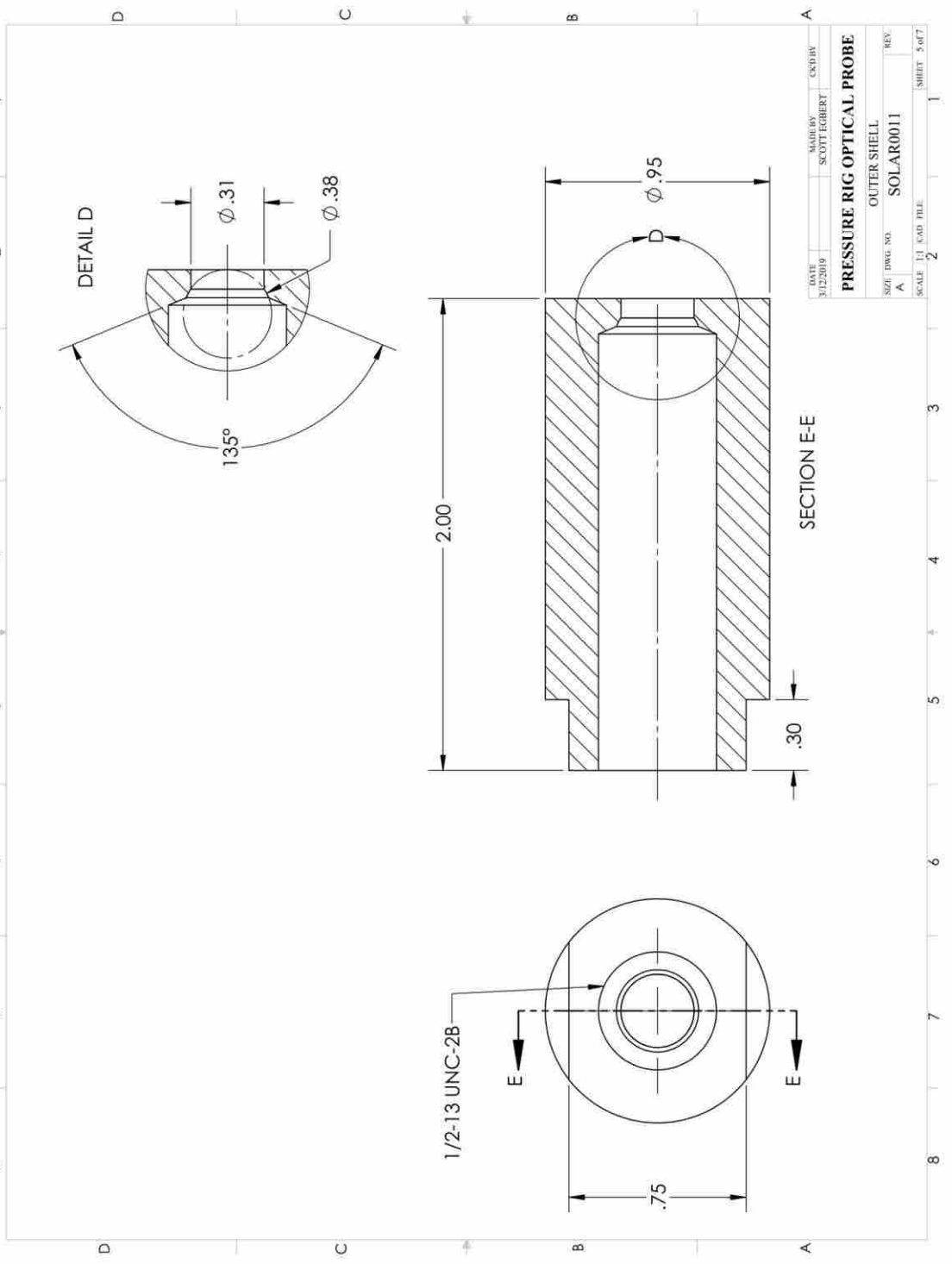

Figure B-5: Pressure rig optical probe, outer shell

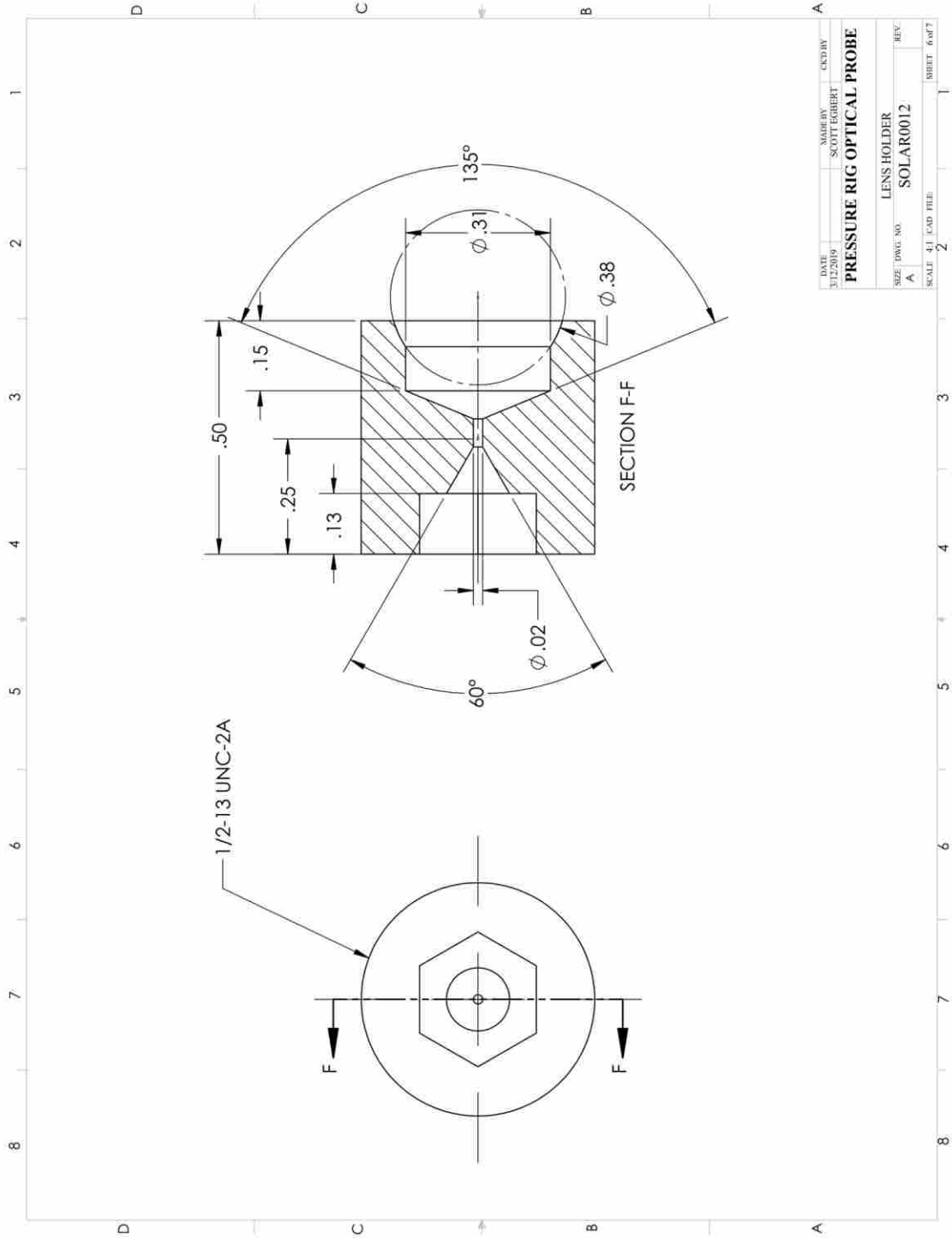

Figure B-6: Pressure rig optical probe, lens holder

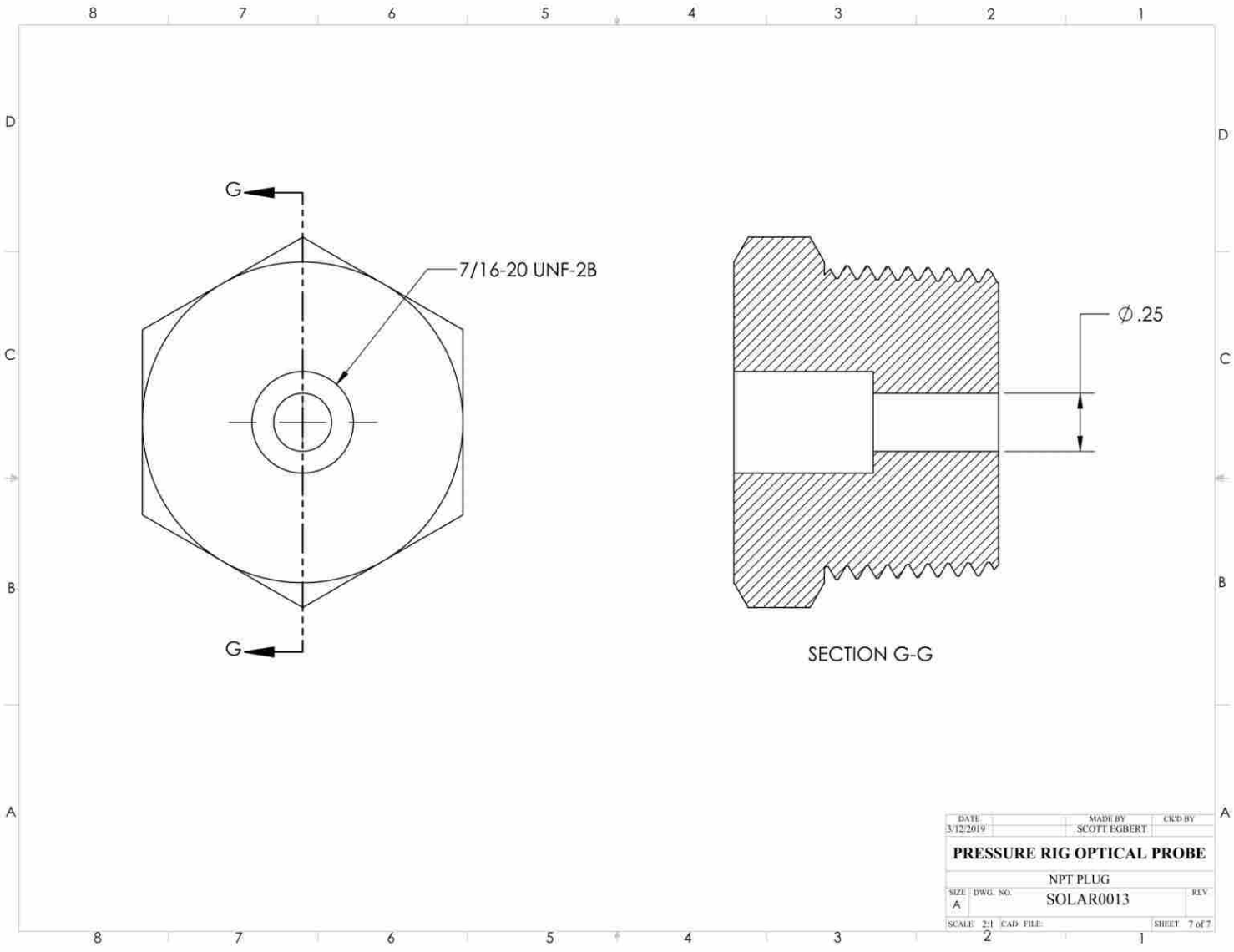

Figure B-7: Pressure rig optical probe, NPT plug

APPENDIX C: QUAD ELEMENTAL INGAAS DETECTOR

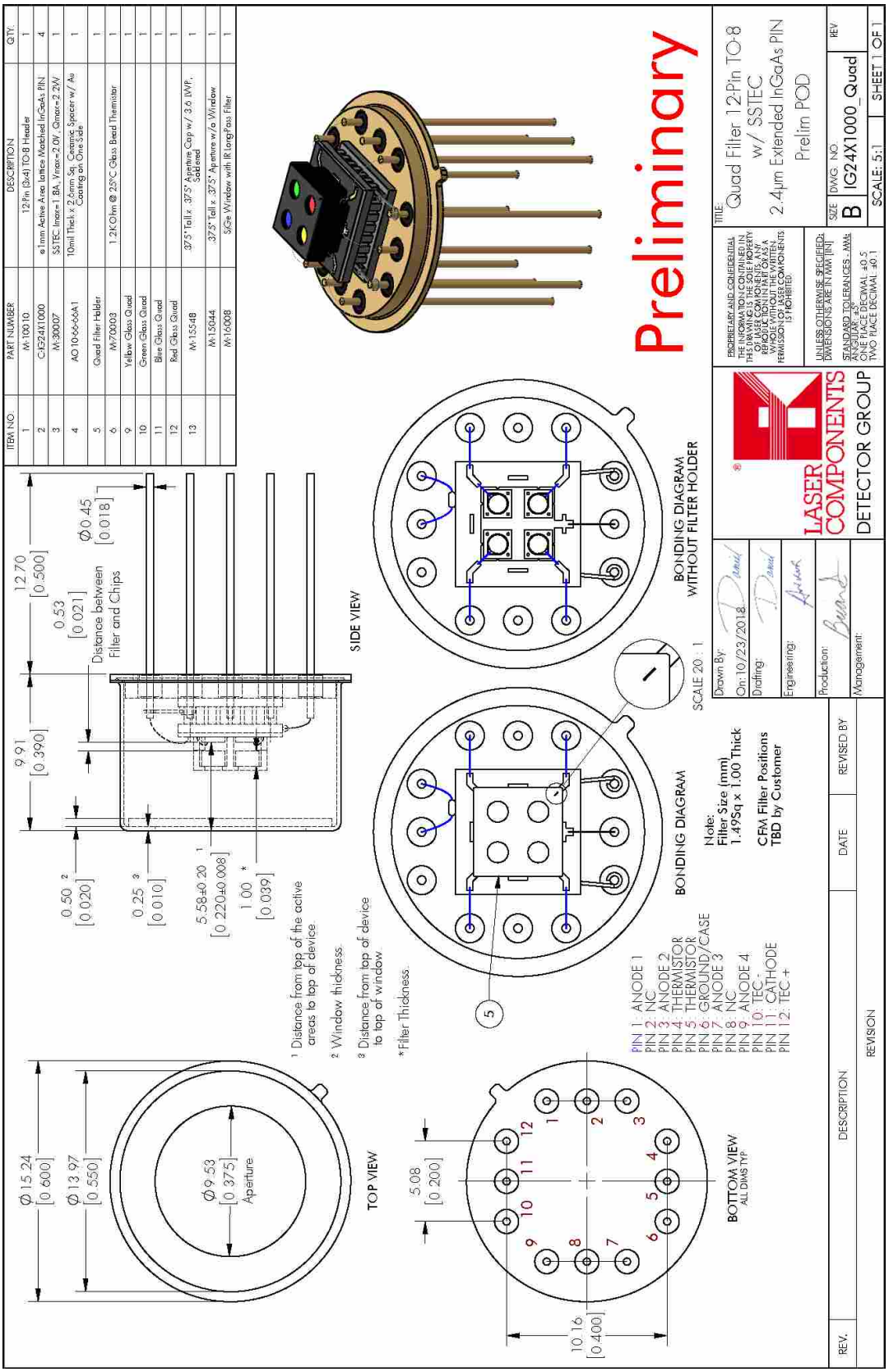

Figure C-1: Quad element InGaAs detector engineering drawing.